MULTINOZZLE PRINTHEADS FOR 3D PRINTING OF VISCOELASTIC INKS

BY

STEPHEN J. KRANZ

THESIS

Submitted in partial fulfillment of the requirements
for the degree of Master of Science in Materials Science and Engineering
in the Graduate College of the
University of Illinois at Urbana-Champaign, 2013

Urbana, Illinois

Advisor:

Professor Jennifer A. Lewis

Abstract

High-pressure microfluidic printheads were developed for 3D printing of viscoelastic inks. These multinozzle arrays were machined out of poly(methylmethacrylate) (PMMA) using a 3-axis CNC mill. Several printhead designs were made, tested, and modeled, including those with bifurcating arrays of microchannels of varying sizes and a plenum design that split a single stream of ink into multiple streams of equal flow yielding devices with 8-, 16-, 64- and 128-nozzles (or outputs). These microfluidic devices were designed to enable (1) high throughput, 3D printing, (2) multimaterial deposition, and (3) parallel printing of arbitrary designs.

An iterative 1D model was developed that predicts the relative volumetric flow rates of power-law fluids in individual channels of a microfluidic network. The model utilized a modified Hagen-Poiseuille equation and the hydraulic-electric analogy. The model was employed to predict hydraulic resistances of various network designs and to determine the effects of geometric asymmetries on the uniformity of extruded filaments. The predictions of this simplified 1D model were in good agreement with those made by 3D finite element modeling using COMSOL.

Finally, these multinozzle printheads were mounted on a 3-axis motion-controlled printer. Using these multinozzle printheads, multiple ink types were successfully patterned, including an organic wax ink, a photo-curable epoxy, a hydrogel, and two colloidal inks.

Acknowledgments

I would like to thank my advisor, Jennifer Lewis, for guiding my research and shaping me as a scientist. Her vision showed me how to solve complex problems and her vision inspired me to work hard to achieve my goals.

I would like to thank my family, especially my sister, Lauren, my mother, Karen, and my late father John, for their unconditional love throughout my life. They have helped shaped me into the person I am today, and I could not be more fortunate. I am also very grateful for my godparents, Jean Doyle and Larry Dukerich, who have helped support me, particularly during my undergraduate and graduate career.

I want to acknowledge all of the current and former members of the Lewis research group, who have made my research at Illinois a fun and exciting experience. In particular, I would like to thank David Kolesky, John Vericella, Chris Hansen, David Lorang, Lucas Osterbur, Scott Slimmer, James Hardin, Jaime Juarez, Adam DeConinck, and Bok-Yeop Ahn for their assistance and advice in the lab. I would also like to thank my undergraduate assistant, Artie Jataputra, for assisting me with the manufacture of devices.

I am very grateful for our collaborators, Bo Jiang and Greg Muldowny at Rohm & Haas, for providing the engineering objectives that motivated this work and for funding the research.

Finally, I would like to thank Charles Kiyanda, Tim Head, Peter Czoschke and David Hull, who have all contributed in some part to the "uiucthesis2009" LaTeX package which I used to format this document.

Table of contents

List of symbols **vi**

Chapter 1 Introduction **1**
1.1 Thesis objectives 2
1.2 Thesis organization 2

Chapter 2 Literature review **3**
2.1 Additive manufacturing 3
2.2 Microfluidic devices 5
2.2.1 Creating PMMA microfluidic devices 6
2.2.2 Bonding of PMMA microfluidic devices 7
2.3 Fluid flow in enclosed channels 7
2.4 Murray's law 8
2.5 Fluid viscosity models 10
2.6 Reynolds number 11

Chapter 3 Multinozzle printhead design, fabrication, and modeling **13**
3.1 Introduction 13
3.2 Experimental methods 13
3.2.1 Microfluidic network design 13
3.2.2 Multinozzle printhead fabrication 16
3.2.3 Fabrication of dual network multinozzle printheads 21
3.2.4 Ink compositions 21
3.2.5 Experimental viscometry and hydraulic resistance measurements 22
3.2.6 One-dimensional modeling of fluid flow 24
3.2.7 3D modeling of fluid flow 26
3.3 Results and discussion 27
3.3.1 Bifurcating microfluidic network design 27
3.3.2 Shear viscometry and hydraulic resistance measurements 28

3.3.3 1D and 3D modeling . . . 33
3.4 Conclusion . . . 46

Chapter 4 High throughput printing via multinozzle printheads 48
4.1 Introduction . . . 48
4.2 Experimental methods . . . 48
4.2.1 Material systems . . . 48
4.2.2 Printing and infilling woodpile lattice pads . . . 49
4.2.3 Co-infill epoxy pad process . . . 53
4.2.4 Adjustable fill factor multinozzle printhead . . . 54
4.2.5 Wide-spaced multinozzle printheads . . . 56
4.2.6 Multinozzle deposition of functional materials . . . 56
4.3 Results and Discussion . . . 57
4.3.1 Printing and infilling woodpile lattice pads . . . 57
4.3.2 Co-infill epoxy pad process . . . 57
4.3.3 Adjustable fill factor multinozzle printhead . . . 60
4.3.4 Wide-spaced multinozzle printheads . . . 62
4.3.5 Multinozzle deposition of functional materials . . . 63
4.4 Conclusion . . . 66

Chapter 5 Conclusions 67
5.1 Future work . . . 68

Appendix A Hydraulic diameter and square channels 69

Appendix B 3D simulations of laminar flow at high Reynolds number 71

Appendix C Multinozzle printhead evolution 73

References 83

List of symbols

Symbol	Meaning	MKS units
A	geometric factor for Newtonian flow in non-circular channels	-
c	apparent nozzle center-to-center spacing	m
C	center-to-center spacing of parallel channels	m
$d,\ d_{hyd}$	hydraulic diameter of a channel or pipe	m
h	square root of a channel's cross-sectional area	$\mathrm{m}^{1/2}$
K_{hyd}	hydraulic conductance	$\mathrm{m}^3/\mathrm{Pa{\cdot}s}$
L	length of a channel or pipe	m
m	power-law dynamic viscosity coefficient	$\mathrm{Pa{\cdot}s}^n$
M	mass of extruded filament	kg
n	power-law dynamic viscosity exponent	-
$p,\ \Delta p$	applied pressure, pressure drop	Pa
P	power involved in fluidic processes	W
Q	volumetric flow rate	m^3/s
R_{hyd}	hydraulic resistance	$\mathrm{Pa{\cdot}s}/\mathrm{m}^3$
Re	Reynolds number	-
t	extrusion time	s
$\bar{v}$	average fluid velocity in a channel	m/s
V	volume of a microfluidic network	m^3
w	apparent filament width	m
$\dot{\gamma}$	shear rate	s^{-1}
η	dynamic viscosity	$\mathrm{Pa{\cdot}\ s}$
θ	orientation angle relative to printing direction	$^\circ$
λ	n-dependent geometric factor for non-circular channels	-
ρ	fluid density	kg/m^3

Chapter 1

Introduction

3D extrusion printing of viscoelastic inks under ambient conditions is a type of additive manufacturing that can be used to fabricate 3D structures in a wide variety of materials. While this printing method is a valuable 3D fabrication process, in terms of mass production it is very slow compared to conventional methods, like injection molding. An attempt to increase the throughput was made with the development of a PMMA "multinozzle" printhead by Hansen, et al.[1]

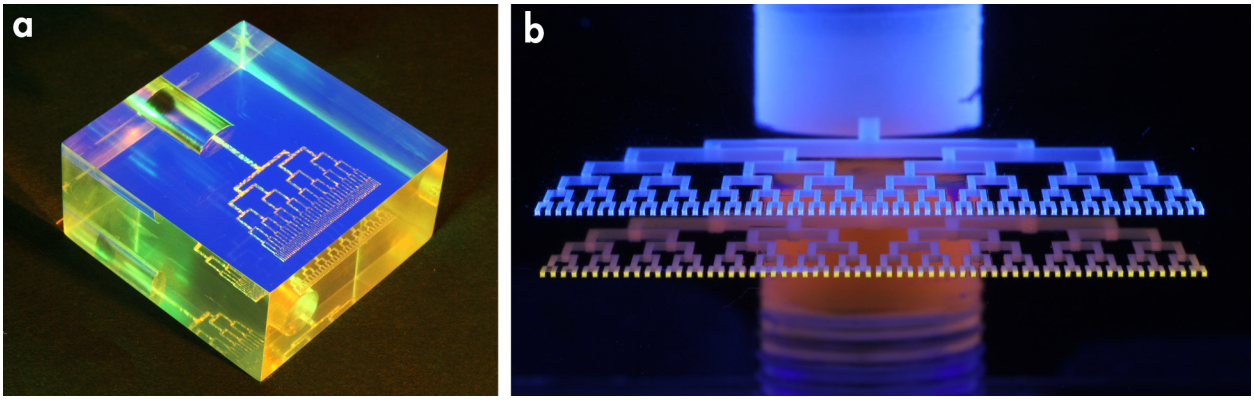

Figure 1.1: Multinozzle devices developed by Hansen, et al. [1] (a) A single network multinozzle device. (b) A dual-network multinozzle device with fluorescent orange and blue organic wax ink.

This thesis focuses on the optimal design and fabrication of multinozzle printheads for 3D printing. Specifically, a modified fabrication technique and 1D model for network design analysis are implemented to asses multiple nozzle designs. We also demonstrate that these printheads can be used to controllably pattern multiple materials.

1.1 Thesis objectives

The objectives of this thesis are to explore the design of a ”multinozzle” printhead device to quickly pattern small features over large areas and to expand the practical applications of the printheads for scalable 3D extrusion printing.

1.2 Thesis organization

In Chapter 2, an overview of additive manufacturing techniques, microfluidic devices, and concepts relevant to fluid flow in microchannels are presented. In Chapter 3, a 1D model for predicting relative volumetric flow rates in microfluidic networks is developed and compared to predictions made by a 3D COMSOL model. In Chapter 4, planar and 3D printed structures are produced from multiple inks using these multinozzle printheads. Finally, the conclusions of this thesis are summarized in Chapter 5.

Chapter 2

Literature review

2.1 Additive manufacturing

Additive manufacturing comprises a broad range of methods for fabricating physical, three-dimensional objects. In additive manufacturing, material is "added", often layer-by-layer, to build an object from the bottom up.[2, 3] Four general types of additive manufacturing are extrusion-based, inkjet, powder-bed, and photo-polymerization.[4]

In extrusion-based methods, a continuous filament is extruded through a dispensing nozzle as the nozzle is translated across a substrate.[2, 5] (Figure 2.1) In fused deposition modeling (FDM), the extruded material is a molten thermoplastic, commonly acrylonitrile butadiene styrene (ABS). After the material is deposited it cools and solidifies. Because of its molten state, the as-deposited filament can fuse with previously deposited filaments. The filaments are deposited in a pattern that matches a single 2D slice of the desired 3D object. Additional 2D layers are built on top of one another, where the layer thickness is equal to the filament diameter.[6] FDM-type machines have recently been adapted into inexpensive, commercially available 3D printers for the do-it-yourself (DIY) user community.[7, 8]

Another form of extrusion-based additive manufacturing is known as "robocasting" or "direct ink writing" (DIW).[5, 9] DIW is operates similar to FDM, but deposits functional inks under ambient conditions rather than thermoplastic filaments. These inks can be ceramic slurries,[10] metals nanoparticle inks,[11] and polymeric hydrogels.[12] Ideally, the inks are viscoelastic, i.e., have a yield stress, so they flow as a shear-thinning fluid through the deposition nozzle, but retain their shape like a solid after deposition. DIW can pattern planar structures like electronic bus bars as well as and 3D structures like scaffolds.[12, 13] DIW can precisely pattern small features. Printed feature size is primarily limited to the diameter of the nozzle that extrudes the material and the precision of the 3D translational axes that position the nozzle. Filament widths as low as 1 µm with positional accuracy of 50 nm have been achieved.[14]

Photo-polymerization methods, such as stereolithography, use an ultraviolet (UV) laser to solidify photo-curable resin. The laser beam exposes a small spot in a thin layer and

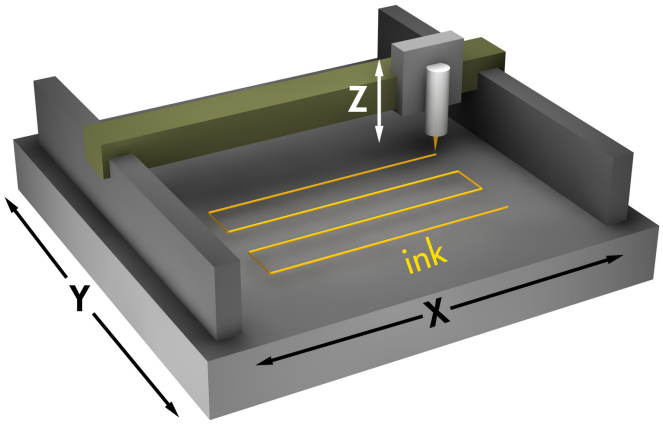

Figure 2.1: A schematic of a 3-axis gantry for 3D extrusion printing.

cures the resin into a solid volume element, or "voxel." The beam is selectively rastered to cure a pattern across a layer that is affixed to a platform. The platform moves incrementally downward, and at each stop, the uncured resin washes over the previous layer. The UV laser exposes another layer, and the cycle repeats. This type of method is limited to photo-curable materials, however filler particles can be suspended in the resin.[15] The resin acts as a binder that can be removed during a sintering process. Feature sizes as small as 5 µm have been achieved in stereolithography processes.[16]

Direct inkjet methods use inkjet printheads to eject material onto a substrate. Picoliter sized liquid droplets are thermally or piezoelectrically ejected from microscopic nozzles.[17] These inks are often composed of ceramic particle slurries,[17, 18, 19] but can also be liquid photo-curable polymers.[20] A layer is patterned by directly depositing a voxel, which is the size of a droplet, onto a substrate. After a layer dries (or is cured) it can support the weight of additional layers. Inkjet methods have been used to create dental implants, high vertical walls, and micro-beams.[17, 18, 19] While these methods can achieve resolutions down to 5 µm, they cannot create overhanging features without the use of support structures.[17]

Powder binding methods of additive manufacturing include methods that selectively bind polymer, ceramic, or metal powders to form a 3D object. The most common powder binding method is selective laser sintering (SLS). In SLS, a laser beam (typically CO_2) rasters across a bed of powder. The intense energy of the beam is absorbed by the particles quickly heating them and allowing them to fuse together. After a single layer is patterned, a thin layer of virgin powder is rolled over the first layer and the laser sintering process repeats.[21] Powder binding can also be done with inkjet printheads. A polymer binder is directly ejected onto ceramic or metal powders. The binder holds the particles together to form a green body. The green body can be sintered to form a dense, final object.[22]

Extrusion- and inkjet-based printing methods provide the greatest materials flexibility compared to other additive manufacturing techniques. However, they also require that the rheological properties of the inks be tightly controlled. Extrusion-based printing (or direct ink writing) can be used to pattern highly viscous inks, while ink-jet printing requires inks to possess low viscosities (<0.1 Pa-s).[5, 23]

A major drawback of additive manufacturing methods is that they are slow. Hence, to date, these technique have been used predominantly for rapid prototyping and small-scale research, because it doesn't require molds which are time consuming and expensive to create. However, if a mold is already made, it is faster to cast a part than to print a part. For additive manufacturing techniques to be viable for mass production, their throughput must be greatly increased. Parallelization of additive manufacturing processes can increase product throughput. For example, digital micromirror devices (DMD) have been used to parallelize curing in photo-polymerization-type additive manufacturing.[16] The DMD can selectively expose hundreds of thousands of voxels instantaneously.[24] The inkjet printheads for powder-binding methods have been designed to eject ink from 16 to hundreds of parallel nozzles.[25, 26] Recently, Hansen, et al., developed a multinozzle microfluidic device for increased throughput in filamentary-extrusion additive manufacturing applications.[1] The device serves as a printhead that accepts a single stream of ink as an input and passively distributes the ink into 64 parallel streams of equal flow. This thesis explores improvements in the design, manufacture and applications of this type of multinozzle printhead.

2.2 Microfluidic devices

Multinozzle printheads are akin to microfluidic devices, which utilize capillaries (10 to 1000 µm) in order to control the flow of small volumes of liquid. Most microfluidic devices are manufactured using poly(dimethylsiloxane) (PDMS), a soft, cross-linkable, silicon-based polymer.[27] (**Figure 2.2**) PDMS is used because the material is relatively inexpensive, can easily be cast onto molds, is optically transparent, inert, and can be bonded to itself.[28] However, PDMS is not a suitable material for DIW applications. Viscous fluids require high pressures to yield fast deposition speed. PDMS devices typically debond at pressures of 250 kPa (36 psi) or less.[29] Hence, while PDMS devices are well suited for applications requiring low viscosity fluids, they are of limited use for multinozzle printing of highly viscous inks. Poly(methylmethalcrylate) (PMMA) is an easily machined, transparent, rigid, thermoplastic that is commonly used to package microfluidic channels. The channels are machined or imprinted onto a face of a PMMA block. The block is bonded to a separate piece of PMMA

and can withstand internal pressures of over 30 MPa (4,500 psi).[30, 31]

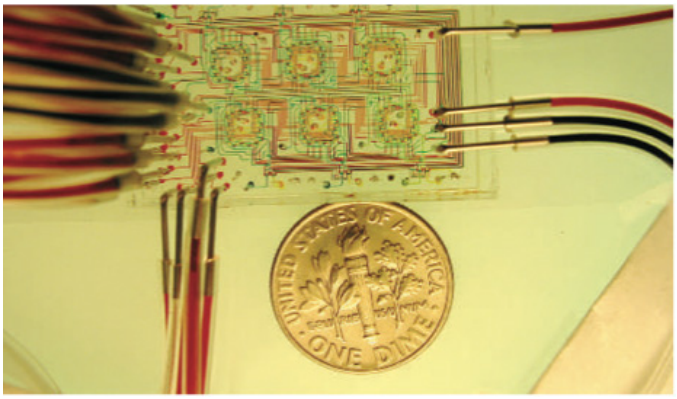

Figure 2.2: A PDMS microfludic device [32]

2.2.1 Creating PMMA microfluidic devices

Microchannels in PMMA devices can be created by computer numerically controlled (CNC) micromilling.[1] Milling is a form of subtractive manufacturing where a spinning cutting tool removes material to form a part. In CNC milling, a computer uses a script to control the axes of the mill that feed the tool through the material. Micromilling is simply milling where features sizes are hundreds of microns or smaller. The scale of features produced by micromachining is mostly limited by the size of the cutting tool (as small as 5 µm) and the precision of the 3D axes (can be less than <1 µm).

The channels in PMMA can also be created with commercially available carbon dioxide lasers.[33] These CO_2 lasers are very efficient at ablating PMMA, as the polymer is highly absorbent at the laser's output wavelength of 10.6 µm. The spot size of these lasers is between 300 and 100 µm, and depending on the power and raster speed of the laser, can produce features as small as 85 µm.[33] Laser ablation of microchannels is a powerful fabrication method because it is very quick and new designs can be easily implemented without any template. However, the limitations of this method are that the channels produced have a Gaussian cross section (because of the Gaussian nature of the laser beam), and often have wavy edges (because of the frequency at which the laser is pulsed).

Hot embossing is another method of forming microchannels in PMMA. This process involves heating a slab of PMMA above its glass transition temperature then pressing it into a quartz or silicon template.[34] The PMMA conforms to the template, and upon cooling it is removed and contains channels corresponding to elevated features on the template. The benefit of hot embossing is that many devices can be quickly fabricated from a single

template. However, a new microfluidic design requires the creation of a new template, which can be time consuming.

2.2.2 Bonding of PMMA microfluidic devices

The PMMA can be self-bonded by solvent welding. The solvent swells the polymer chains on the substrate surface.[35] The swollen chains are less dense and less tangled than in the bulk. When brought into contact with another surface of PMMA, the swollen chains of the two pieces entangle and upon solvent evaporation, collapse to form a strong bond. The solvent can be applied in a liquid or vapor phase.[30] PMMA can also be thermally bonded by pressing the two pieces together at a temperature at or above the glass transition.[31] Thermal bonding can be very strong, but the small embedded features are susceptible to deformation when the polymer softens in the heat.[30] (Figure 2.3)

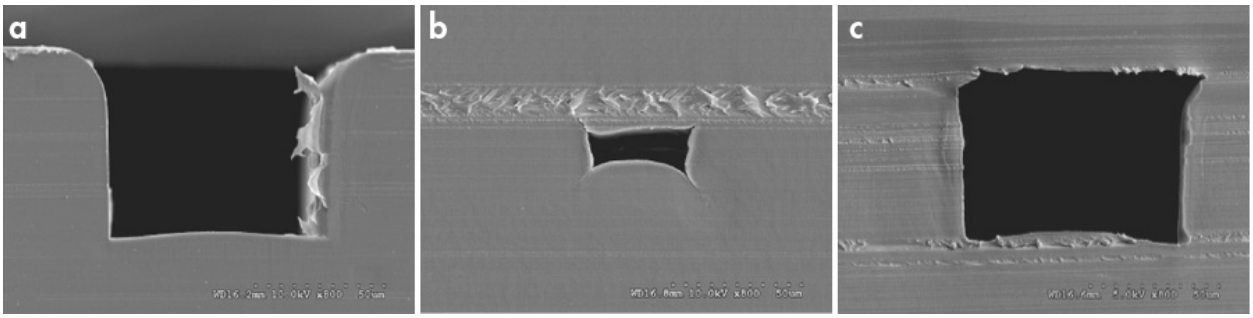

Figure 2.3: Bonding of PMMA channels. (a) Channel before bonding. The wide of the channel is roughly 60 μm (b) Channel after thermal bonding. (c) Channel after vapor solvent bonding. [30]

2.3 Fluid flow in enclosed channels

The flow of Newtonian fluid through a long cylindrical channel is described by the Hagen-Poiseuille equation:

$$\Delta p = \frac{128 \eta L Q}{\pi d^4} \tag{2.1}$$

where Δp is the pressure drop (Pa), L is the length of the channel (m), η is the dynamic viscosity of the fluid (Pa-s), Q is the volumetric flow rate (m^3/s), and d is the inner diameter of the channel.[36] While equation (2.1) can predict the volumetric flow rate of a fluid through a single channel, in most engineering applications (such as a branching microfluidic network), there exist more complicated systems of channels. These systems can include parallel flows with multiple inlets and outlets. In order to predict the relative pressures and volumetric flow rates of individual elements in those systems, it is useful to employ

the electric-hydraulic analogy.[37] In this analogy, the flow of a Newtonian liquid through channels can be compared to the flow of electricity through a direct current circuit. Most importantly, voltage (ΔV) is to pressure (Δp), as current (I) is to volumetric flow rate (Q), and as electrical resistance (R_{elec}) is to hydraulic resistance (R_{hyd}). Physically, a voltage source, like a battery is analogous to a pump that applies pressure. A wire is like a very wide pipe that has negligible resistance. An electrical resistor is like a capillary that has a small diameter or a long length. Thus, Ohm's law is analogous to the Hagen-Poiseuille equation:

$$\Delta V = IR_{\text{elec}} \tag{2.2a}$$

$$\Delta p = QR_{\text{hyd}} \tag{2.2b}$$

where the hydraulic resistance depends on the geometry of the channel (the length and diameter) and the viscosity of the fluid.

$$R_{\text{hyd}} = \frac{128}{\pi}\frac{L\eta}{d^4} \tag{2.3}$$

Akin to circuits, the resistances of hydraulic channels can be simplified to find a total equivalent resistance for a system. The equivalent resistance of channels in series is the sum of the individual resistances.[37, 38]

$$R_{\text{series}} = \Sigma R_i \tag{2.4}$$

The equivalent resistance of channels in parallel is the inverse of the sum of the inverse individual resistances.

$$\frac{1}{R_{\text{parallel}}} = \Sigma\frac{1}{R_i} \tag{2.5}$$

Given the dimensions of each channel in a fluidic network, the viscosity of the fluid, and the total applied pressure, the system can be solved such that the flow rates and relative pressures at every junction can be calculated.

2.4 Murray's law

The microfluidic channels in the original multinozzle printhead form a bifurcating array that conforms to Murray's law.[1] Murray's law provides a framework for designing the diameters of channels in a branching fluidic network.[39] Specifically, the cube of the mother channel

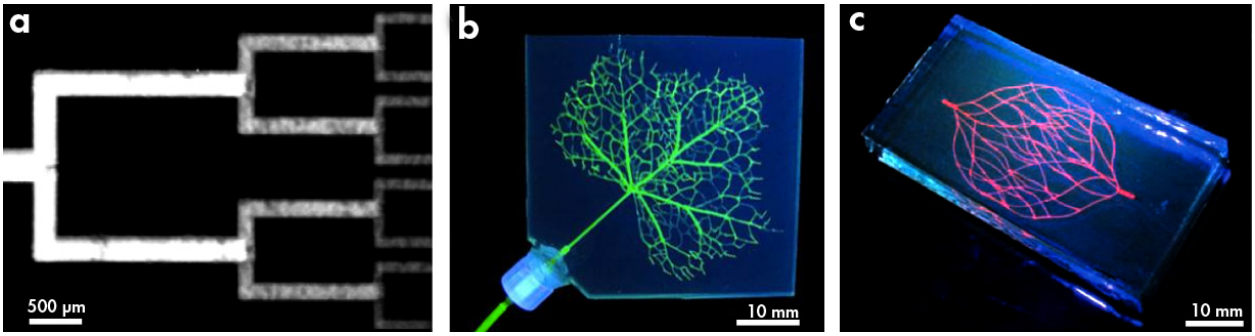

Figure 2.4: Artificial microfluidic vasculature conforming to Murray's law (a) A laser machined artificial vasculature system. Brighter areas indicate greater channel depth.[40] (b) A 2D microchannel architecture that mimics ivy leaf venations.[41] (c) A 3D microvasculature system created with omnidirectional printing in a gel.[42]

diameter is equal to the sum of the cubes of the daughter channel diameters:

$$d^3_{\text{mother}} = \Sigma d^3_{\text{daughter}} \tag{2.6}$$

For the case of a bifurcating network, a mother channel will have a diameter roughly 1.25 times that both daughter channels. Murray's law is an optimization of power. A system requires power (P_{f}) to flow fluid through channels and also metabolic power (P_{m}) to generate the volume of fluid that fills the vasculature. The total power, P, is

$$P = P_{\text{f}} + P_{\text{m}} \tag{2.7}$$

Both types of power are dependent on the channel dimensions. An increase in diameter, d, requires less power to maintain flow, but requires more metabolic power to fill the larger channel volume.

$$P_{\text{f}} = aQ^2 d^{-4} \tag{2.8a}$$

$$P_{\text{m}} = bd^2 \tag{2.8b}$$

The value of a is proportional to the fluid viscosity and b is proportional to the metabolic cost of producing a unit volume of fluid. The minimum total power can be found by differentiated it with respect to d and setting it equal to zero. Solving for the volumetric flow rate shows that it is proportional to the diameter cubed.

$$Q = \left(\frac{b}{2a}\right)^{1/2} d^3 \tag{2.9}$$

This minimum in a single channel can be applied to an entire branching system, which yields Murray's law. Many natural fluidic systems obey Murray's law, such as human vasculature and lung alveoli.[43] Murray's law has also been applied to microfluidic designs.[40, 41] However, for systems in which metabolic power requirement is negligible—e.g., multinozzle printheads—this microchannel design may not be optimal.

2.5 Fluid viscosity models

Fluids can be categorized by their viscous behavior as a function of strain rate. The simplest and most common model for fluids is the Newtonian model. Newtonian fluids exhibit a constant viscosity that is independent of strain rate.[36] (**Figure 2.5**) Water and glycerol are typical Newtonian fluids. The one-dimensional method of calculating a network resistance as outlined above assumes that the viscosity is constant at all shear rates. For many fluids in biological[44] and engineering applications[45, 46] this is not true. Fluids with viscosities that depend on strain rate are broadly termed non-Newtonian fluids. Fluids that become more viscous with increased strain rate (like mixtures of corn starch and water) are shear-thickening, while fluids that become less viscous with increasing strain (like polymer melts and colloidal gels) are shear-thinning.[47, 48] It is useful to have a model that predicts the viscosity of a liquid at a given strain rate. For non-Newtonian fluids, a common and simple model is the power-law model:[49]

$$\eta = m\dot{\gamma}^{n-1} \tag{2.10}$$

where η is the dynamic viscosity (Pa-s), $\dot{\gamma}$ is the shear rate (s^{-1}), and m and n are material parameters. The parameter m is equal to the viscosity at unity shear rate, while n is the power law exponent. If $n = 1$, the fluid's viscosity is constant (with a value of m) at all shear rates and is therefore Newtonian. If $n < 1$, the material is shear-thinning, and if $n > 1$, it is shear-thickening. In this model, if $n < 1$, as the shear rate approaches zero, the viscosity goes to infinity, and as the shear rate goes to infinity, the viscosity goes to zero. Real materials do not exhibit such extreme viscosities at these extreme shear rates. Real non-Newtonian fluids tend to have Newtonian behavior at very high and very low shear rates. A more complicated viscosity model, the Carreau model, takes into account the viscosity plateaus at high and low shear rates:[50]

$$\eta(\dot{\gamma}) = \eta_\infty + (\eta_0 - \eta_\infty)(1 + (\lambda\dot{\gamma})^2)^{\frac{n-1}{2}} \tag{2.11}$$

where η_∞ and η_0 are the constant viscosities (i.e., the plateaus) at very high and very low shear rates, respectively. The parameter n is the power law index that describes the shear-thinning behavior at intermediate shear rates. The value of λ describes a relaxation time of the fluid.

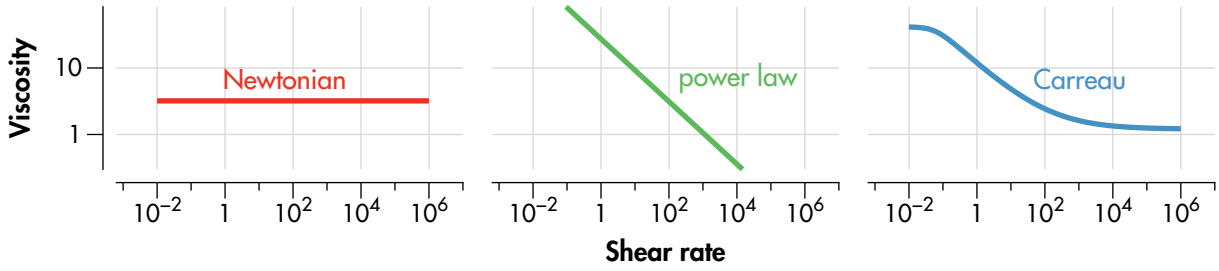

Figure 2.5: Viscosity models of Newtonian, power-law and Carreau fluids.

2.6 Reynolds number

The Reynolds number is a dimensionless measure of inertial forces to viscous forces in a fluid. For fluid flow in a pipe, the Reynolds number, Re, is given by

$$\mathrm{Re} = \frac{\rho \bar{v} d}{\eta} \tag{2.12}$$

where ρ is the fluid density, v is the fluid velocity, d_{hyd} is the hydraulic diameter of the pipe, and η is the dynamic viscosity of the fluid.[36] Reynolds number can be calculated for semi- or completely enclosed channels (like a pipe or a river) as well as an object in a fluid. At high Reynolds numbers (>3000), inertial forces dominate the fluid flow and turbulence can occur. At low Reynolds numbers (<100), viscous forces dominate and the fluid flow is laminar.[51] The range of Reynolds numbers between several hundred and several thousand are a transition regime that can have both laminar and turbulent characteristics.[52] The small nozzle dimensions and the high ink viscosities used in extrusion printing lie in the laminar regime. (Fig 2.5) The laminar flow of fluids in microchannels allows us to accurately utilize the Hagen-Poiseuille equation. Pressure losses associated with bifurcations, sudden changes in hydraulic diameter, and surface roughness of channel walls are significant for turbulent fluids, but can be ignored if the Reynolds number is low.[38, 53] Because of the very low Reynolds numbers of fluids in this work, we can neglect many high-Reynolds number phenomena and create a simple 1D model useful for analyzing the design of microfluidic networks.

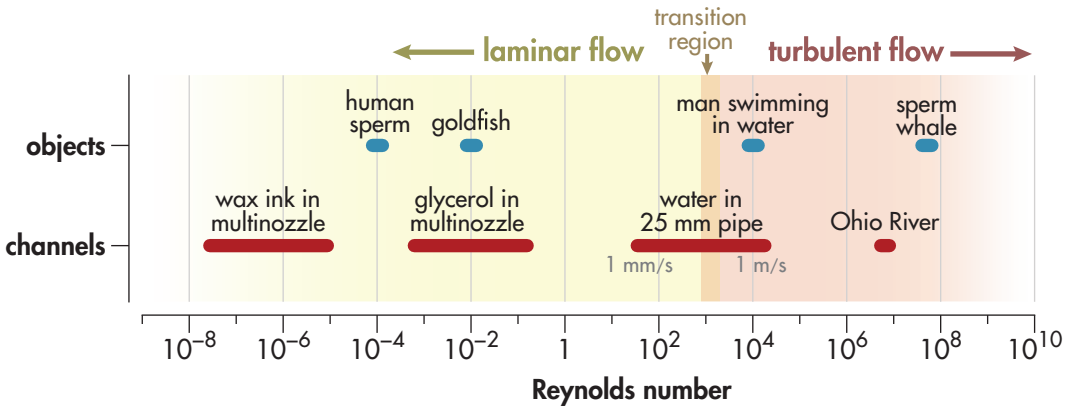

Figure 2.6: The range of Reynolds numbers for various objects and channels. [51, 54]

Chapter 3

Multinozzle printhead design, fabrication, and modeling

3.1 Introduction

In this chapter, four types of symmetric, 64-output, multinozzle designs are investigated. The goal of these multinozzle designs is to split a single stream of ink into 64 streams of equal flow through embedded microfluidic networks of varying architecture. These microfluidic networks are machined into PMMA, and then packaged into printheads that can withstand high internal pressures. We experimentally measured the pressure dependence on the volumetric flow rates of Newtonian and non-Newtonian fluids through each network. These results are compared with 3D finite element analysis (FEA) software (COMSOL), as well as the results of a 1D model written using a Matlab script. The 1D model, which is computationally fast, calculates the pressure drops and flow rates at each junction within a given microfluidic network design. The 1D model is employed to model deviations in flow rates when geometric asymmetries are introduced into the networks. The analysis of these results aims to identify geometric parameters of the network that optimize the design with respect to the total pressure drop and ink volume, which is tolerant to defects in the geometry that might give rise to differential flow rates across the printhead.

3.2 Experimental methods

3.2.1 Microfluidic network design

All of the microfluidic networks considered have common exit nozzle geometry. The exit nozzles are square channels, 2 mm long, 0.2 mm $\times$ 0.2 mm in cross-section, from which printed filaments are extruded. They are arranged linearly, equally spaced, with a 0.4 mm center-to-center spacing. Three of the network designs, referred to as Murray's law, Wide, and Extra-wide, are composed of a fractal network of 6 generations of bifurcating square channels (**Figure 3.1**). Starting at the 64 outlets and moving upwards, each generation increases in hydraulic diameter. The hydraulic diameters of these three network designs—which are

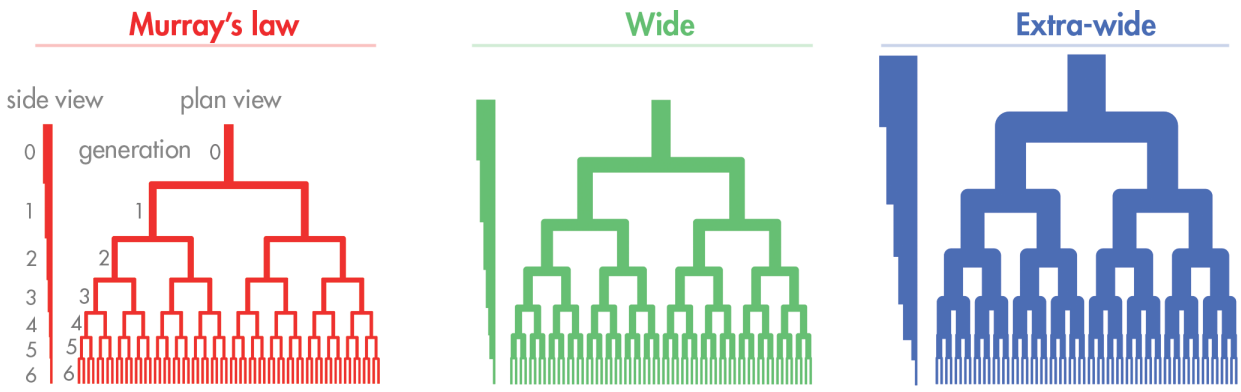

Figure 3.1: The three bifurcating microfluidic network designs. Generation 6 is constant in these three designs. The Wide and Extra-wide designs employ wider and deeper channels in earlier generations.

Table 3.1 Hydraulic diameters of each microfluidic channel per generation (mm)

	Network designs		
gen.	**Murray's law**	**Wide**	**Extra-wide**
0	0.8	1.6	3.2
1	0.65	1.3	2.6
2	0.5	1.0	2.0
3	0.4	0.8	1.6
4	0.3	0.6	1.2
5	0.25	0.5	0.5
6	0.2	0.2	0.2

equal to the width and depths of the square channels—are provided in **Table 3.1**.

Each child of a junction has a horizontal segment, a 90° bend, and is followed by a vertical segment. The length of the horizontal segment is dependent on the generation number i, and the center-to-center spacing of the ith generation, C:

$$L_{\text{horz}} = C(2^{i_{\text{final}}-i})/2 \tag{3.1}$$

In the Murray's law network, the vertical length of a child is equal to 6 times the child's hydraulic diameter. For the Wide and Extra-wide designs, the vertical length is 3 and 1.5 times the hydraulic diameter, respectively. The total length of a channel in a generation is defined as the vertical length plus half the width of the channel plus half the horizontal center-to-center spacing (**Figure 3.2**). The fourth network, the Plenum design, has only two generations of bifurcations with diameters much larger than the outputs (3 mm), which flow into a single open chamber, or plenum. The plenum is a roughly 30 mm wide, 4 mm tall and 2 mm deep (**Figure 3.3**). Since the widths of the upper generations and plenum are

Table 3.2 **Length of each microfluidic channel per generation (mm)**

	Network designs		
gen.	**Murray's law**	**Wide**	**Extra-wide**
0	4.8	4.8	4.8
1	10.6	11.0	11.6
2	6.5	6.7	7.2
3	4.2	4.4	4.8
4	2.75	2.9	3.2
5	2.0	2.2	2.2
6	2.3	2.3	2.3

much larger than the diameters of the output channels, very little pressure drop is expected according the Hagen-Poiseuille equation.

These different network designs are created by milling channels into a block of poly(methyl-methacrylate) (PMMA), i.e., acrylic, using a 3-axis CNC mill. Each channel is machined using and endmill with a diameter between 50% and 90% of the width and depth of the channel (between 175 µm and 3.175 mm in diameter) (**Figure 3.4**). The feed rates used varied between 100 and 800 mm/s, while the spindle speeds ranged from 25,000 to 45,000 rev/min.

In addition to a microfluidic network for evenly distributing ink, some multinozzle printheads have a filter machined into the channel block upstream of the bifurcating network (**Figure 3.5**). This filter consists of two rows of parallel square channels with widths of 300 and 180 µm. The filter traps debris, such as hair or dust, which can inadvertently be in the ink supply. The filter prevents the debris from entering the bifurcating network and clogging the small nozzle channels. The filter does produce a significant pressure drop and was not included in printhead devices used to measure the pressure drop of the microfluidic networks (§3.3.2).

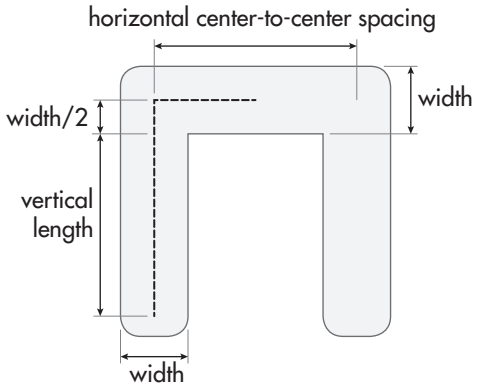

Figure 3.2: A schematic for calculating the total length of a channel in a given generation.

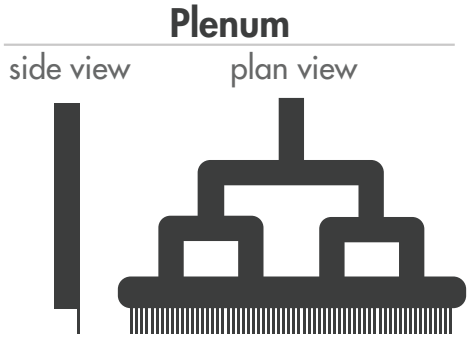

Figure 3.3: The plenum design has the same nozzle geometry as the Murray's law, Wide, and Extra-wide designs. However, before the nozzles, fluid flows into an open chamber, or plenum.

3.2.2 Multinozzle printhead fabrication

Each multinozzle printhead is composed of three individual pieces of cast acrylic, which are machined using a 3-axis CNC mill (V6, Wabeco). The parts are bonded together by a solvent welding process, and the bonded parts are machined and polished to their final form. There are three parts that form a multinozzle printhead: the channel block, the blank block, and the top cap. The blank block is a rectangular block of cast acrylic that is machined to a size of 70 mm wide (X), 35 mm tall (Y) and 8 mm thick (Z) (**Figure 3.6**). There are two semi-circular slots (1.6 mm radius) on the XY face located 19.25 mm to the left and 19.25mm to the right of the X center of the face. These slots run along in the Y direction from $Y = 0$ to $Y = 35$. These slots will eventually allow screws to fasten the completed multinozzle printhead to the 3D positioning gantry. The channel block is manufactured to the same dimensions using this procedure, while additionally machining a bifurcating network of channels onto the XY face of the block in between the two slots. The third piece, the top cap, is also made from acrylic. It measures 70 mm wide, 16 mm tall and 12 mm thick. It has a 9 mm hole and 1/8" NPT threads, centered hole that goes through the thickness of the block. Two smaller, 3.2 mm holes, located 19.25 mm to the left and to the right of the central hole. These small holes will match up with the semi-circular slots in the channel and blank blocks.

The multinozzle printhead is assembled from these parts using a solvent welding process (**Figure 3.7**). During the solvent welding of PMMA, a solvent (e.g., acetone or acetonitrile) swells the polymer at the surface, solvating the polymer chains. These solvated chains can entangle with chains from the opposing surface. When the solvent evaporates, the entangled polymer chains bond the two pieces. To prepare the channel and blank blocks for solvent welding, the XY faces of the channel and blank blocks are polished to an 800-grit (CarbiMet 2 grinding paper, Buehler) on a polishing wheel (EcoMet 250, Buehler). This process removes

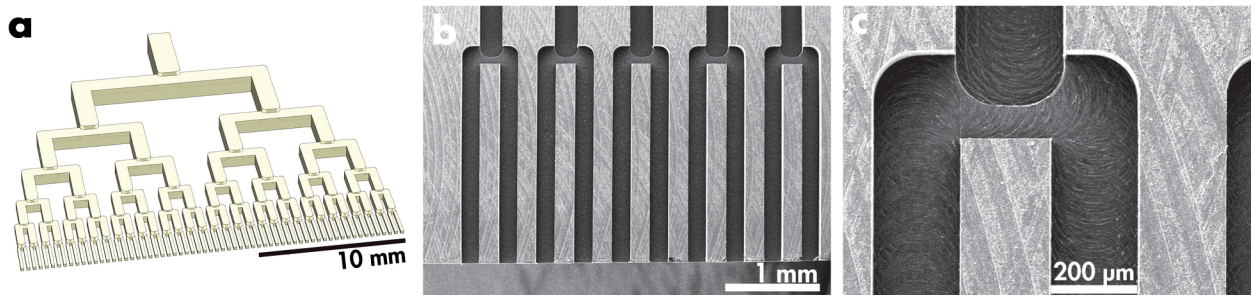

Figure 3.4: Microfluidic channels in a multinozzle printhead. (a) 3D rendering of Wide design network. (b,c) Scanning electron micrographs of final generation of channels in a Murray's law design.

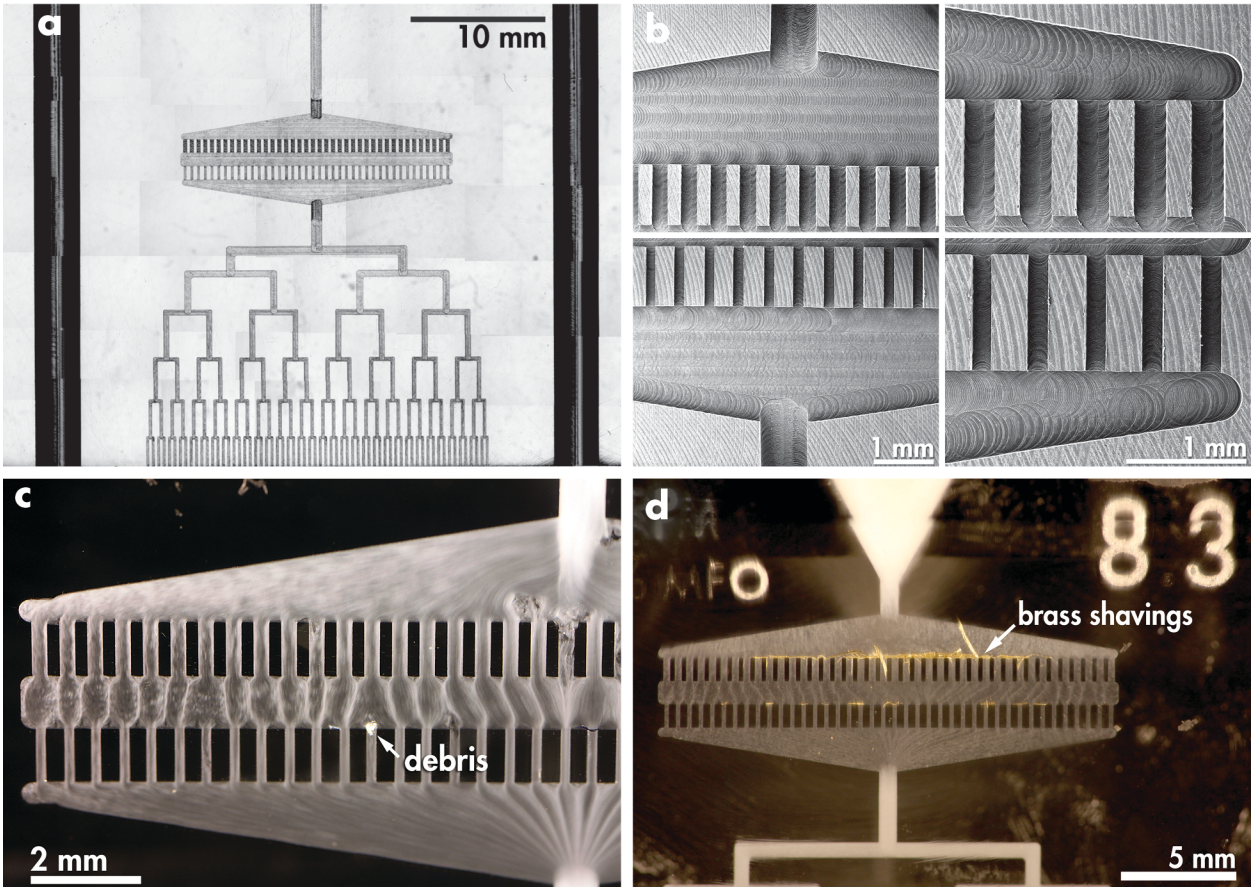

Figure 3.5: Filters embedded in mutlinozzle printhead. (a) Micrograph mosaic of a completed channel block with a filter. (b) Scanning electron micrographs of a filter. (c) A filter with wax ink flowing through it. A piece of debris is caught in the a 180 µm channel. (d) Brass shavings are caught in a filter.

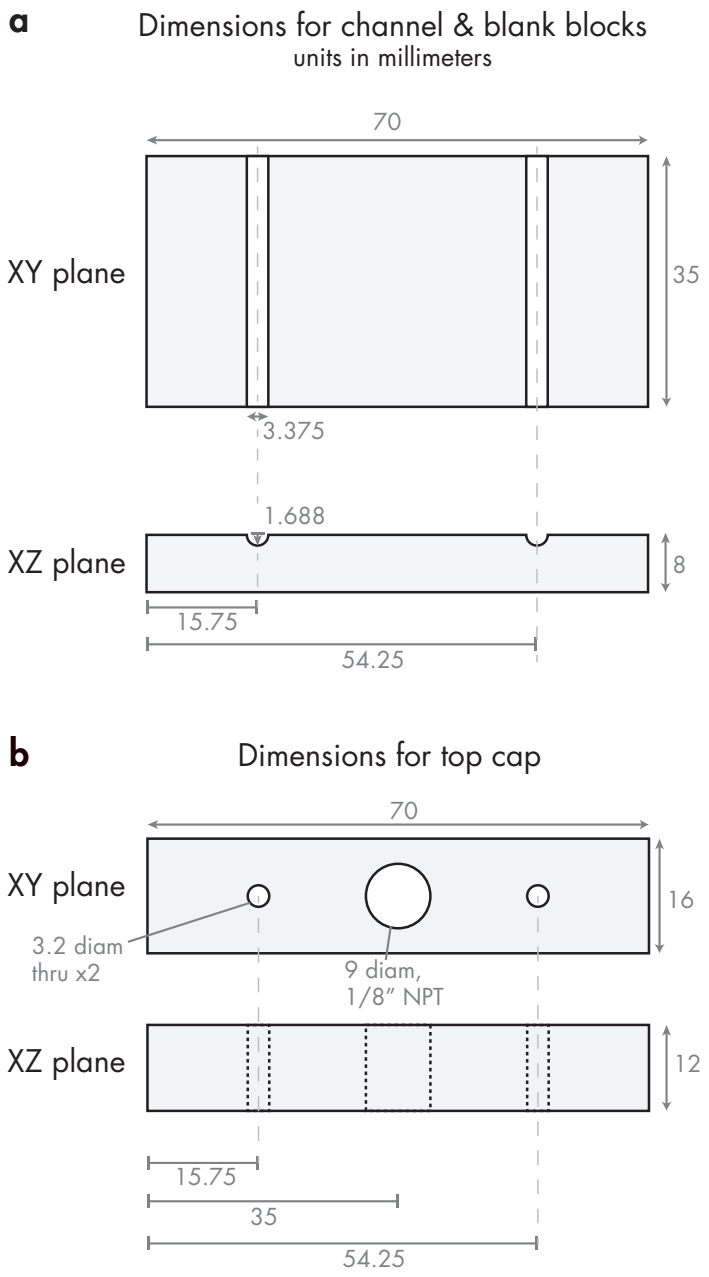

Figure 3.6: (a) Dimensions for channel and blank blocks. Both channel and blank blocks are identical, except microfluidic channels are milled into the channel block. (b) Dimensions for the top cap. The top cap connects the ink input (1/8" NPT) to the microfluidic network. All units are in mm.

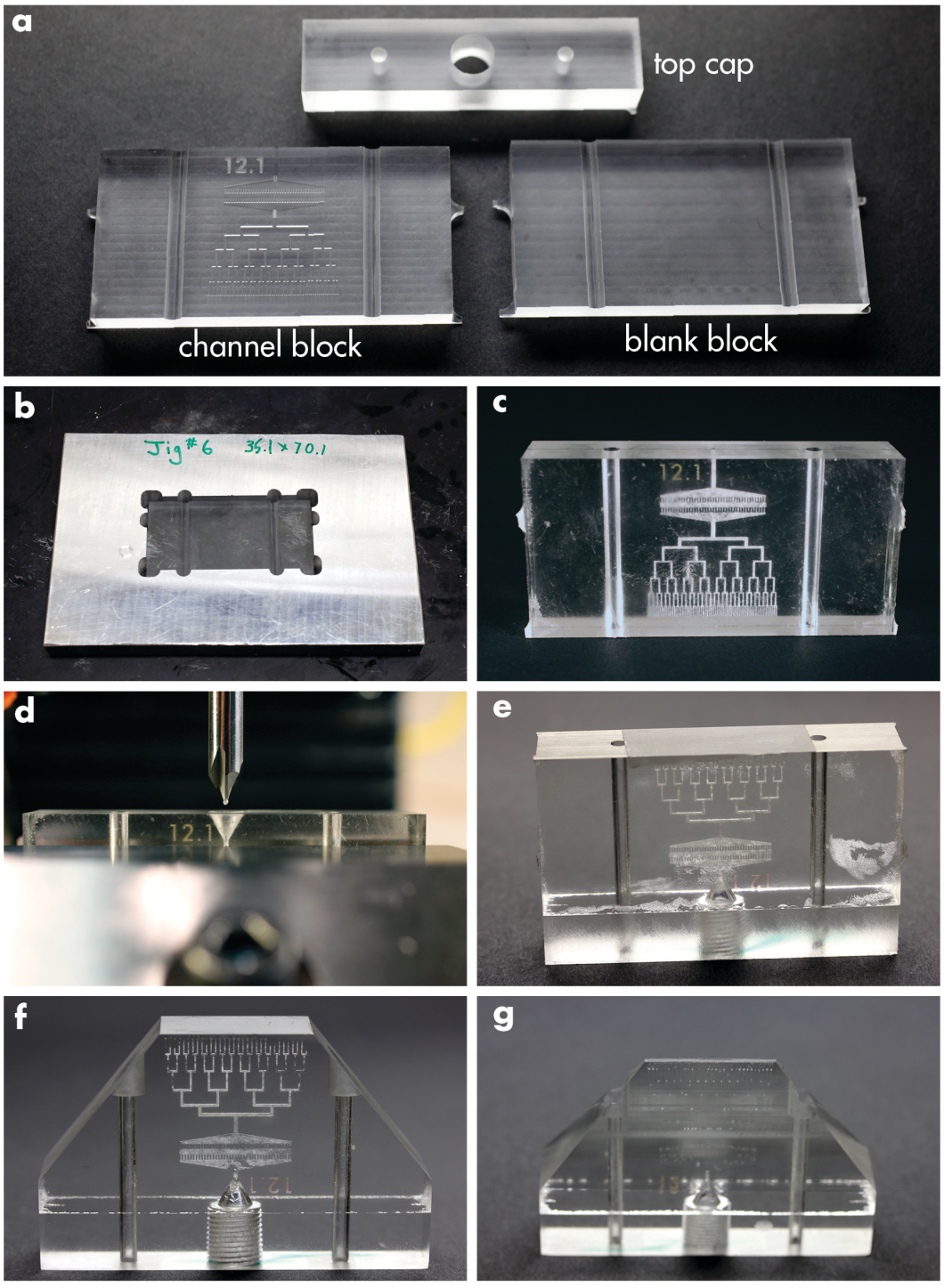

Figure 3.7: (a) Parts that compose the multinozzle printhead: the top cap, channel block, and blank block. (b) Aluminum jig used to align the channel and blank blocks for solvent welding. (c) The mated channel and blank block; or the *block assembly*. (d) A chamfered endmill creates a cone that joins the input in the top cap to the bifurcating network. (e) The top cap bonded onto the block assembly; or the *multinozzle assembly*. (f) The left and right corners are cut off. (g) The front and back corners are cut to bring the device to a taper.

the tool marks from the machined surfaces, which are about 10 µm deep. The channels of the channel block are filled in with molten low-melting-point (24-26°C) wax (Purester 24, Strahl & Pitsch). After cooling to room temperature (22°C), the wax solidifies, and excess wax above the surface is removed with a razor blade. The wax completely fills in the channels and is flush with the polished surface. Air is blown across the surfaces of the channel and blank blocks to remove dust particles. A jig is created to hold the channel and blank blocks in place during solvent welding. The jig is a piece of aluminum 150 mm × 100 mm × 12 mm thick, with a rectangular hole marginally larger than the 70 mm × 35 mm blocks. The blank block is set into the jig with the face containing the slots facing upward. Solvent (acetonitrile, Fisher) is pipetted onto the exposed surface, using enough to completely cover the entire surface (~2 mL). After about 10 to 15 s, the channel block is placed in the jig, on top of the blank block. The face with the embedded channels and slots is facing down, and is mated with the blank block. A weight (2.5 kg) is placed on top of the two blocks and is allowed to sit for 15 min. The mated blocks are referred to as the block assembly. The assembly is removed from the jig and allowed to sit for at least 24 h. The microfluidic network is machined into the channel block such that the exit nozzles of the network do not extend all the way to the outside of the assembly, but are completely encased ~2 mm from the edge. To expose the nozzles, the CNC mill is used to machine away 2 mm of the "bottom" of the block assembly, thus opening the 64 outputs to ambient. The "top," or input-side, of the block assembly ensured to be smooth by machining approximately 0.5 mm off of the surface. One of the 70 mm × 16 mm faces of the top cap is bonded onto the 70 mm × 16 mm input-side face of the block assembly. The top cap is laid flat such that the centerlines of the three holes are oriented vertically. Steel dowel pins (3.17 mm diameter, 35 mm length) are inserted into two 3.2 mm holes of the top cap. Solvent (Weld-On, acrylics

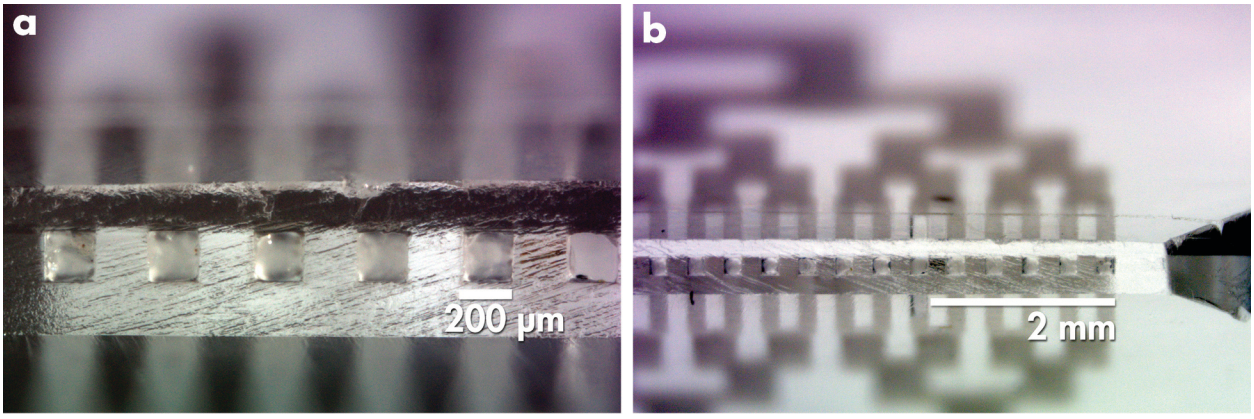

Figure 3.8: (a,b) End-on micrographs of the printhead's nozzles as they exit the device. The nozzle cross section is a 200 µm square.

#3) is pipetted onto the top cap surface. The block assembly is inverted such that the input side is oriented downward. The two dowel pins in the top cap are inserted into the two slots of the block assembly. The block assembly is pressed into contact with the top cap and a weight (2.5 kg) is placed on top of the block assembly. After ~15 min, the weight is removed and the mated top cap-block assembly is left to sit for at least 24 h. The mated three pieces are collectively called the multinozzle assembly. The multinozzle assembly goes through a final machining step, wherein the packaging of the assembly is brought to a taper, with the exit nozzles at the tip (**Figure 3.8**). It is polished, and the completed device is ready for use.

3.2.3 Fabrication of dual network multinozzle printheads

In §4.2.3, we use a multinozzle printhead with two sets of parallel, but offset 64-output arrays. To construct this "dual network" multinozzle printhead, two blocks of cast acrylic (70 mm wide, 35 mm tall, 8 mm thick) are machined on a 3-axis CNC mill (V6, Wabeco). A six-generation, 64-output, bifurcating, Murray's Law network is machined on the large faces of both acrylic blocks. One of the networks is centered on the block with respect to the 70 mm edge. The other network is offset by 200 µm, which is equal to the feature size and spacing between outputs. In the channel block designated for the epoxy, a 9 mm circular hole is drilled 4 mm from the top edge and centered horizontally. This hole is hand-tapped to cut 1/8" NPT threads, and the hole serves as an input for tubing supplying the epoxy. A thinner, third acrylic piece (70 mm wide, 35 mm tall, 1.6 mm thick) is machined and acts as a separator between the two channel blocks. The channel-face of the channel block designated for the wax is solvent welded to the thin, center piece. The channel-face of the epoxy channel block is then solvent welded to the opposite side of the center piece. A top cap (70 mm wide, 17.6 mm tall, 10 mm thick) with a threaded 1/8" NPT hole is solvent welded to the top of the three-block assembly. The entire mated device is cut such that the exit nozzles are exposed at the tip of a taper. The device is polished to optical clarity and is ready for printing.

3.2.4 Ink compositions

Two inks are used in the experimental fluidic measurements of the multinozzle printhead network designs. One ink is glycerol, which is commercially available (Fisher) and has well-established Newtonian rheology. The second ink is a two-component ink with shear thinning properties. This ink is composed of 60 wt% petroleum jelly (Vaseline, Unilever) and 40 wt% microcrystalline wax (SP-18, Strahl & Pitsch). The two components are placed in a glass

beaker with a magnetic stir bar. The beaker is heated on a stir/hot plate heated at around 120°C until both components are completely molten and mixed. The heated mixture is drawn by suction into a syringe barrel (60 mL, Becton, Dickinson and Company), a filter is attached to the syringe (2 µm pore size, Millex AP-20, Millipore), and the filtered mixture is extruded into a clean beaker. The beaker of clean ink is remelted, then poured into a pump (500D, Teledyne Isco), where it solidifies prior to printing under ambient conditions.

3.2.5 Experimental viscometry and hydraulic resistance measurements

The shear rate dependence of the viscosity of a fluid can be determined by commercially available, controlled-stress rheometers. However, the bulk viscosity of a material determined this way can differ by several orders of magnitude compared to the apparent viscosity of the same material in a microchannel.[55] In order to measure the apparent viscosity in sub-millimeter channels an experimental setup reported by Bruneaux, et al.[55] is created (**Figure 3.9**). A pressure control box (Ultimus V High Precision Dispenser, Nordson EFD) supplies controlled air pressure to a syringe barrel, which is loaded with the material to be tested. A cylindrical dispensing tip of known geometry is attached to the other end of the syringe barrel (**Figure 3.10**). When air pressure is applied, fluid flows through the dispensing tip and is extruded onto a weigh boat. The weight boat is weighed before and after the extrusion so the total mass, M, extruded (~0.5 to 10 g) can be calculated. The time of extrusion, t, (20 s to 10 min) is measured manually with a timer. Using these values along with the density, ρ, of the material, the volumetric flow rate, Q, can be calculated as

$$Q = \frac{M}{\rho t} \tag{3.2}$$

The Hagen-Poiseuille law states that the pressure drop, Δp, over a length of circular pipe is

$$\Delta p = \frac{128}{\pi} \frac{\eta L Q}{d^4} \tag{3.3}$$

where L is the length of the pipe, d is the inner diameter of the pipe, η is the fluid viscosity. The pressure drop dependence on diameter is so strong that we can assume that virtually the entire pressure drop in the experimental set up is occurring across the dispensing tip. Because the applied pressure is experimentally controlled, the length and diameter of the dispensing tip are known, and the volumetric flow rate is measured and calculated, the

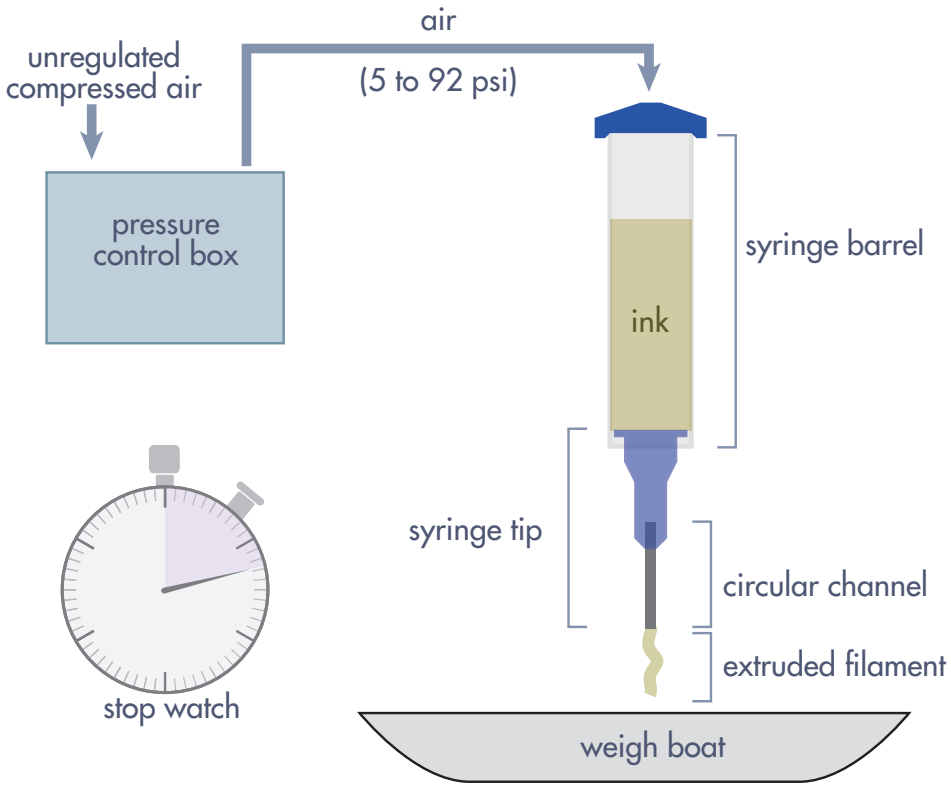

Figure 3.9: The microextrusion experimental set up. Applied pressure extrudes ink through a steel tube in a syringe tip. The extrusion time is recorded, and the mass change of a disposable weigh boat is measured. With knowledge of the ink density, volumetric flow rate can be calculated.

Figure 3.10: The three syringe tips used in the microextrusion experiment. The labels refer to the inner diameter of the steel tubes.

Hagen-Poiseuille equation can be solved for the dynamic viscosity.

$$\eta = \frac{\pi}{128}\frac{\Delta p d^4}{LQ} \tag{3.4}$$

And the shear rate of a Newtonian fluid can be calculated by

$$\dot{\gamma} = \frac{32}{\pi}\frac{Q}{d^3} \ . \tag{3.5}$$

The experiment is carried out using wax ink in order to calculate the material parameters of a power-law viscosity model. This viscosity model is used in other hydraulic resistance measurements.

A similar experiment is performed with bifurcating microchannel arrays in order to measure the hydraulic resistance of the array. In this case, the dispensing tip is removed and replaced with a multinozzle printhead. The volumetric flow rate is measured for a range of applied pressures and the hydraulic conductance, K_{hyd}, is calculated as

$$K_{\text{hyd}} = R_{\text{hyd}}^{-1} = \frac{Q}{\Delta p} \ . \tag{3.6}$$

The hydraulic conductance of the multinozzle printhead is important because it is a measure of how easily material can be extruded at a given pressure.

3.2.6 One-dimensional modeling of fluid flow

The flow of a Newtonian fluid through a bifurcating microfluidic network can be modeled by first simplifying the geometry of the network. The geometry of the network is approximated by an array of 1D pipes each with a defined length and diameter. The diameters of the pipes are equal to the hydraulic diameter of a given channel. The lengths of the pipes are equal to the sum of the vertical and horizontal lengths of each channel. Along with the geometry, the viscosity of the fluid is used to calculate the hydraulic resistance of each individual pipe.

$$R_{\text{hyd},i} = \frac{128}{\pi}\eta\frac{L_i}{d_i^4}A \tag{3.7}$$

where A is a geometric factor dependent on the tube's cross sectional shape. For circles $A = 1$, and for this work's case of squares $A = 0.697$.[38] The hydraulic resistances of the 90° elbows, the bifurcating junctions and the sudden changes in hydraulic diameter are neglected. This is a good assumption when low-Reynolds number fluids ($\text{Re} \ll 1$) are considered.[53] The hydraulic-electric analogy is employed and each section of pipe is treated as an electrical

resistor. The equivalent resistance of the entire network can be calculated using Kirchhoff's circuit laws for resistors in series and in parallel. The total "current" or volumetric flow rate can be calculated by dividing the "voltage" or pressure drop by the resistance. A custom Matlab script was written that calculates: the individual tube resistances for given geometric dimensions, the total equivalent resistance, and the total volumetric flow rate. It then calculates the volumetric flow rate and potential drop at each bifurcation. The script allows for the theoretical total volumetric flow rate to be compared to the experimentally measured values. It also allows for the study of the effects of systematic geometric defects on the evenness of volumetric flow rates of individual exit nozzles.

In the case of non-Newtonian fluids, the apparent viscosity is dependent on shear rate and cannot be assumed to be constant. The shear rate depends on the volumetric flow rate; the volumetric flow rate depends on the hydraulic resistance; and the hydraulic resistance depends on the apparent viscosity. This cycle of dependence renders the above script unable to accurately model non-Newtonian flow. To circumvent this cycle, an iterative model was created to calculate the flow rate at an applied pressure for a power-law fluid in a single pipe. First, an initial volumetric flow rate is guessed. This guess must a positive, non-zero value, but otherwise can be off by as much as 100 orders of magnitude. It is used to calculate the shear rate.

$$\dot{\gamma} = \frac{32}{\pi}\frac{Q_a}{d^3} \tag{3.8}$$

This shear rate is in turn used to calculate the apparent viscosity.

$$\mu = m\dot{\gamma}^{n-1} \tag{3.9}$$

This viscosity is used to calculate the hydraulic resistance.

$$R_{\text{hyd}} = \frac{128}{\pi}\frac{L\eta}{d^4} \tag{3.10}$$

The resistance is used to calculate a new volumetric flow rate.

$$Q_b = \frac{p_{\text{applied}}}{R_{\text{hyd}}} \tag{3.11}$$

This new flow rate is fed into the shear rate equation and the cycle is continued until the difference between the new calculated flow rate and the previous value is insignificant.

$$\frac{|Q_a - Q_b|}{Q_a} < 10^{-4} \tag{3.12}$$

Once the difference is small enough, the model is converged, and this value is used in analysis.

A direct, approximate solution to the volumetric flow rate of power-law fluids through pipes has been previously developed:[5]

$$Q = \frac{\lambda(n) h^{3+(1/n)} (-\frac{\Delta p}{L})^{1/n}}{m^{1/n}} \tag{3.13}$$

where $\lambda(n)$ is a geometric factor that depends on the cross sectional shape of the pipe, and h is the square root of the pipe's cross sectional area. This direct solution is simpler in the case of a single pipe. However, because the volumetric flow rate depends on Δp to the $1/n$ power, the hydraulic resistance ($R_{\text{hyd}} = \Delta p/Q$) cannot be solved for independently of both Δp and Q. This means that the method of directly calculating the total network resistance (a la electrical resistors) with Newtonian fluids cannot be used with Liu's[5] direct solution of power-law flow.

The iterative non-Newtonian script can be adapted to model fluid flow through multiple generations of bifurcations. The inputs of this model are the total applied pressure, the geometry (length and width) of each channel, and the material properties (m, n) of the ink's dynamic viscosity. This model operates by estimating a total volumetric flow rate for the entire network, $Q_{0,i}$, and flow rates for each channel in each generation. These values of Q_i are used to calculate the shear rates and the dynamic viscosities in all 127 channels of each of the six generations ($2^6+2^5+2^4+2^3+2^2+2^1+2^0 = 127$). The individual hydraulic resistances of each channel are calculated and summed to find the total network hydraulic resistance. A total volumetric flow rate and individual channel flow rates are calculated. These flow rates are used to calculate the next iteration of shear rates, viscosities and resistances. This procedure iterates until the difference of flow rates between one step and the previous is insignificant.

3.2.7 3D modeling of fluid flow

Finite element analysis (FEA) computational fluid dynamics (CFD) was performed using COMSOL multiphysics simulation software. The results from the 3D COMSOL simulations are compared to experiment and the results of the Matlab scripts.

The FEM models are created in COMSOL 4.3a. The 3D models use the single phase, laminar flow physics, and are stationary type studies. The geometries used include single, straight channels with circular or square cross-sections; square channels with 90° elbows; and bifurcating networks with a single inlet and between 2 and 64 outlets. The inlets of these models are set to "Pressure, no viscous stress" where the value of the applied pressure

ranges from 10 to 1000 psi. The outlets are set to "Pressure, no viscous stress" with a value of zero. The walls of the channels are set to no-slip boundary conditions. In some instances, boundaries of geometric symmetry are employed to reduce the computation time of the solutions. The geometry is meshed with tetrahedral elements. The largest mesh element is no more than one-seventh the width of the given channel. The analysis or "study" employs the default iterative, multigrid solver. The volumetric flow rates are calculated by boundary integration-type model couplings.

3.3 Results and discussion

3.3.1 Bifurcating microfluidic network design

The goal of bifurcating microfluidic network designs is to split a single stream of ink into multiple streams of equal flow. The network that evenly distributes the ink should have a small hydraulic pressure drop. Reducing the pressure drop has two main benefits: (1.) For a given applied pressure, a network with a lower pressure drop will have a higher flow rate. A higher flow rate results in extruded features being patterned faster, thereby increasing throughput. (2.) The multinozzle printhead device has a finite strength and the printhead device can fail at the welded seems at high applied pressures. By testing a small fraction of total printhead devices (4 of ~60), they could withstand maximum pressures of 1000 to 1750 psi before failing. In practice, the devices are utilized at 750 psi or below. Aside from reducing the pressure drop, the bifurcating network design should have a small volume. While the principle ink used in this work (organic wax) is inexpensive (~$35/L), other functional inks may be orders of magnitude higher. Thus, a small network volume within the printhead results in less wasted material. The first network designed approximately follows Murray's Law, which optimizes for both low pressure drop and ink volume. Although some inks are expensive, the model inks used here are not, and thus we moved to optimize the design favoring a reduced pressure drop, while tolerating a larger total network volume.

The focus on optimizing the reduction of the pressure drop lead to three additional designs termed, *Wide* (W), *Extra-wide* (EW), and *Plenum* (Plen). The most dramatic way to reduce the pressure drop of fluidic channels is to increase the hydraulic diameter. Since it was a design requirement that the extruded filaments be 200 µm square and be separated by 200 µm gap (400 µm center-to-center spacing), the last generation (i.e., the exit nozzles) remained the same in all four designs. In order to quantify the efficacy of these designs, volumetric flow rates versus applied rates were measured, calculated, and simulated in following sections.

3.3.2 Shear viscometry and hydraulic resistance measurements

The apparent viscosity of the organic ink in a microchannel is measured using the microextrusion-viscometry experiment outlined above. Two single, circular channel geometries are used for these experiments: one channel is 510 µm in diameter and 12.65 mm long, the other is 200 µm in diameter and 12.25 mm long. Wax ink is extruded at pressures ranging from 50 to 630 psi. The volumetric flow rate versus applied pressure is measured, and this data is used to calculate the apparent dynamic viscosity versus shear rate, shown in **Figure 3.11**. For both channel diameters, the ink shows a clearly shear thinning behavior over the shear rates, ~10^1 to 10^4 s^{-1}, examined. Both sets of data are very good fits to power law viscosity models:

$$\eta = m\dot{\gamma}^{n-1} \tag{3.14}$$

For the 510 µm diameter channel the power law parameters are m=730 Pa-s^n, n=0.44, and for the 200 µm diameter channel, m=230 Pa-s^n, n=0.56. These parameters agree well with work by Bruneaux, et al.[55] who used the same ink formulation and a similar experimental set up. Note, that the apparent viscosities of the wax through microchannels are 2 or 3 orders of magnitude lower than the viscosity of the bulk ink, as measured in a parallel plate rheometer, **Figure 3.12**. Although the final generation of the network designs have a hydraulic diameter of 200 µm, the values from the 510 µm channels were used in the simulations below (§3.3.3). The 510 µm channel dataset is used due to its larger sample size and range of shear rates.

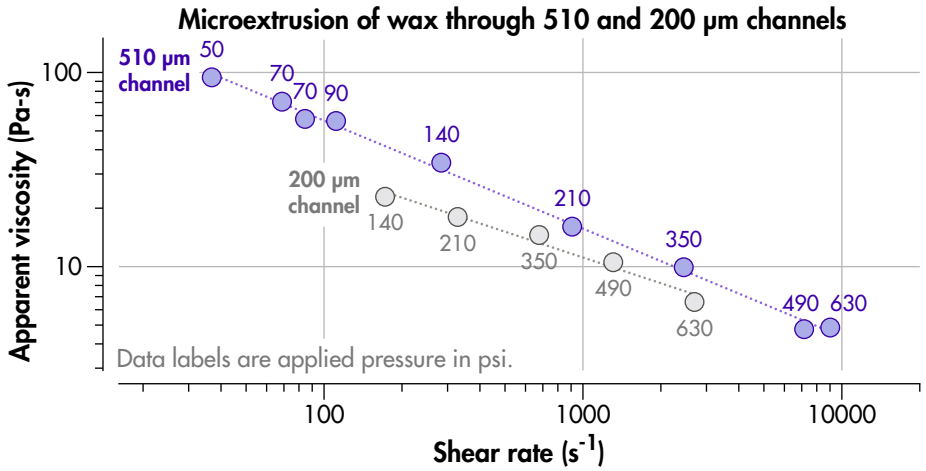

Figure 3.11: The apparent viscosity versus shear rate data for the organic wax ink extruded through 510 and 200 µm channels. This data is calculated from the volumetric flow rate versus applied pressure measured using the experimental setup in Figure 3.9.

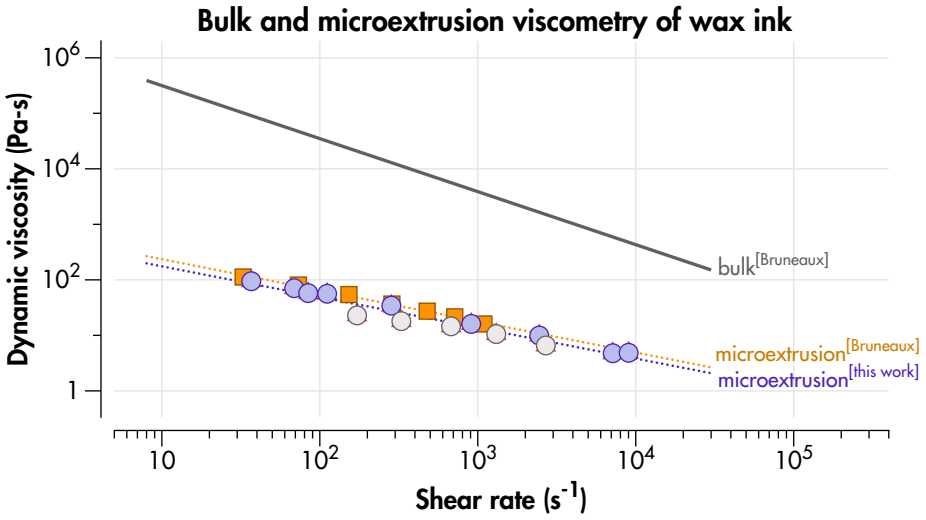

Figure 3.12: Viscosity vesus shear rate for organic wax ink. The data from Figure 3.11 plotted along with bulk and microextrusion viscometry by Bruneaux [55].

While the microextrusion viscometry experiment matched previous work, a separate effort was carried out to verify the validity of the experiment with regards to calculating viscosity. With the same experimental setup, the organic wax ink is replaced by glycerol (Fisher Scientific). Glycerol is a Newtonian fluid with well-established viscosity.[56] These experiments are performed and plotted in **Figure 3.13**. Three geometries are examined, the same 510 µm and 200 µm channels used with the wax, as well as a 100 µm inner diameter, 12.6 mm length channel. Applied pressures between 5 and 490 psi yielded shear rates between 3×10^2 and 2×10^4 s^{-1}. The viscosities calculated ranged from 0.55 to 1.15 Pa-s. The expected value of the viscosity of glycerol at 22.5°C is 1.19 Pa-s for all shear rates. The viscometry data for glycerol is significantly more scattered than for the wax ink (**Figure 3.11**). There also appears to be a very slight shear-thinning tendency. This experiment is performed with each of the three channel sizes on two separate days. On both days, the ambient temperature was between 22°C and 23°C. Since glycerol is hygroscopic, it may have absorbed water, which would lower its viscosity.

Interestingly, using the same experimental procedure on water ($\eta \approx 1$ mPa-s)[56] produced more anomalous results (**Figure 3.14**). De-ionized water (18 MΩ) is extruded through 200 µm and 100 µm channels. In both geometries a similar trend was seen at low shear rates the viscosity is high, quickly dips at slightly higher shear, then increases nearly linearly at even higher shear rates. We could find no other reports of non-Newtonian behavior of water at small length scales and we believe these anomalous results are the product of the limitations of the experimental setup. Because water has such low viscosity—about 10^3 times less than glycerol and 10^4 to 10^5 times less than the wax ink[56]—very little pressure is required

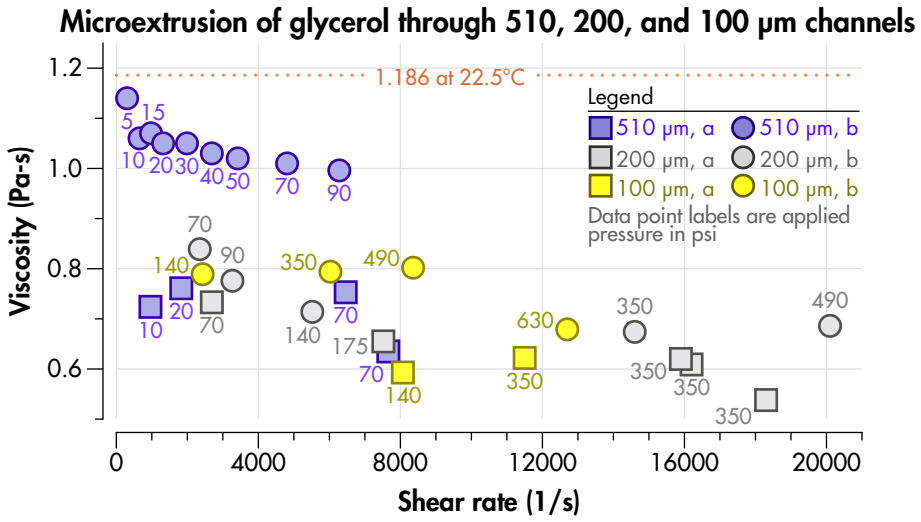

Figure 3.13: The calculated apparent viscosity versus shear rate for glycerol extruded through syringe nozzles of 510, 200 and 100 µm diameters. Experiments *a* and *b* were performed on different days.

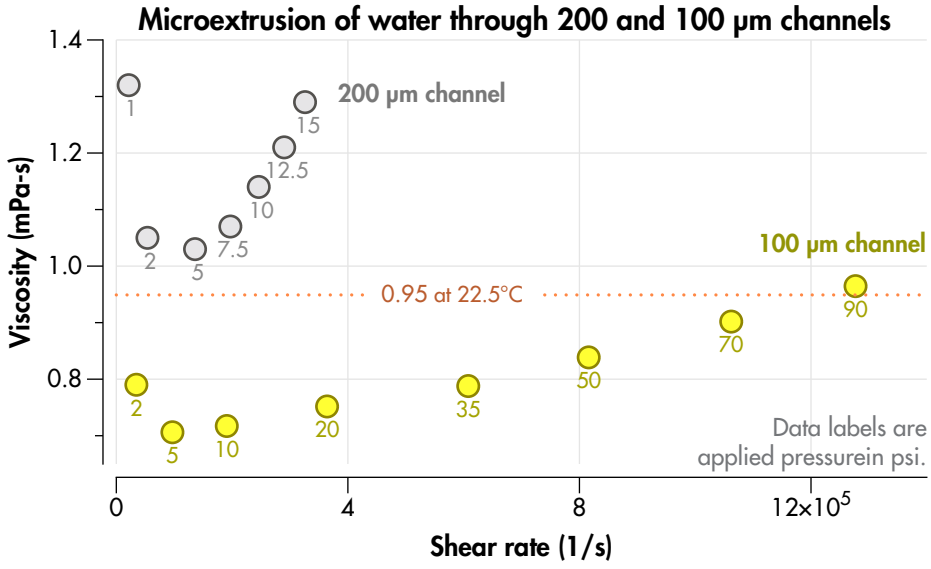

Figure 3.14: The calculated apparent viscosity versus shear rate for water extruded through syringe nozzles of 200 and 100 µm diameters.

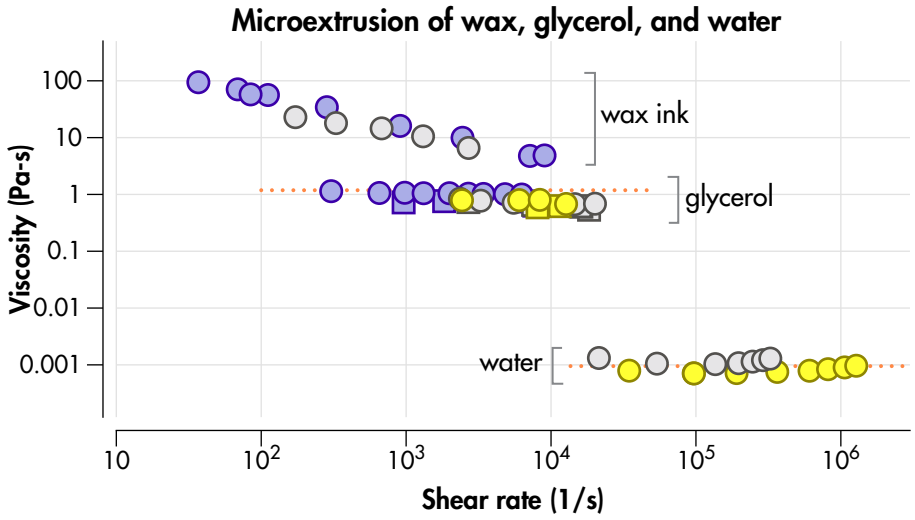

Figure 3.15: Log-log plot of viscosity versus shear rate for microextrusion experiments of wax, glycerol, and water. This is the same data from Figures 3.11, 3.13, and 3.14.

to produce measureable flow rates. Thus, for small shear rates, the applied pressure is very low (1 and 2 psi). At these low pressures, it is possible that we can no longer assume that the only resistance to flow is due to the hydraulic resistance of the 200/100 µm channel. It is plausible that the frictional resistance of the plunger against the inner sides of the syringe barrel becomes significant, thus making the water appear more viscous. At slightly higher pressures, this internal friction is no longer significant. At even higher pressures, the expected volumetric flow rates are higher than can be supplied by the pressure controller. Thus, a lower flow rate for the higher pressures results in an apparent rise in viscosity. When the results of the microextrusion of wax, glycerol, and water are plotted on a single log-log plot (**Figure 3.15**), it is clear that the apparent shear-thinning behavior of glycerol and water are insignificant compared to the wax ink.

In the experimental setup for the single-channel extrusion measurements, the EFD tip housing the single channel can be replaced by a multinozzle printhead. This allows for the direct calculation of the hydraulic resistances of the networks. These measurements were performed for three network designs, Murray's law, Wide, and Extra-wide; and with two fluids, glycerol and the organic wax ink. The volumetric flow rates versus applied pressure for glycerol flowing through the three designs is plotted as filled circles in (**Figure 3.16**). The fits for the three designs are linear with a zero intercept, as expected for a Newtonian fluid. The slopes of these fits are equal to the hydraulic conductance (mL/psi-s), which is simply the inverse of the hydraulic resistance. With glycerol as the fluid, the hydraulic conductances of the Murray's law, Wide channels and Extra-wide channels networks are

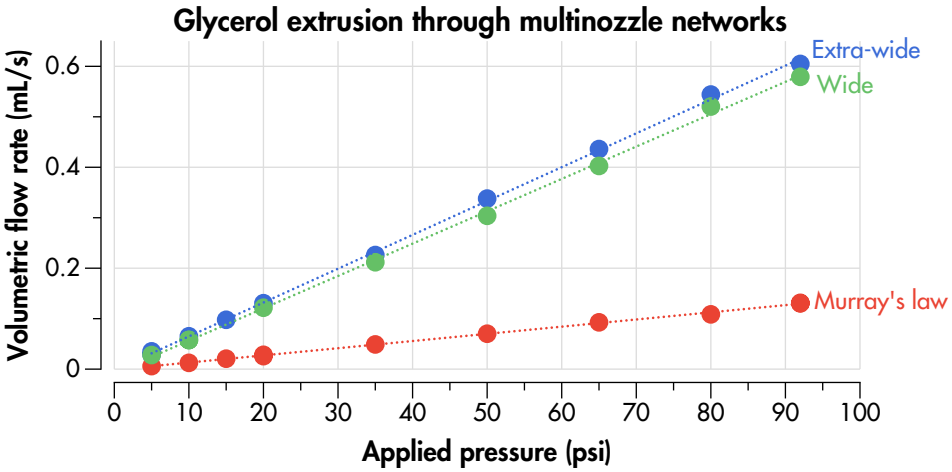

Figure 3.16: Linear plot of volumetric flow rate of glycerol extruded through multinozzle networks versus applied pressure. The same experimental procedure in Figure 3.9 is used, except the syringe tip is replaced with a multinozzle network.

1.4×10^{-3}, 6.4×10^{-3} and 6.7×10^{-3} mL/psi-s, respectively. The Wide channels network is 4.5 times more conductive than the Murray's law network, while the Extra-wide channels network is only 1.05 times more conductive than the Wide channels network.

The three multinozzle printheads used for the glycerol flow rate versus pressure experiment are washed out with water and isopropanol. The printheads are re-used for the same experiment, except that organic wax ink replaces the glycerol. The volumetric flow rate versus applied pressure is plotted as filled circles in (**Figure 3.17**). Because the ink exhibits power-law rheology, the data is plotted on a logarithmic scale for clarity. As expected, the increasing width of the upper generations of the network correlates with higher flow rates at a given pressure. The volumetric flow rates of the Wide network are between ~2 to 14 times higher than the Murray's law network at pressures between 70 and 420 psi. Across the same pressures, the flow rates of the Extra-wide network are about 2.4 times higher than the Wide network, and between ~5 and 35 times higher than the Murray's law network. The three sets of data each fit a power function of the form $Q \propto \Delta p^{1/n}$. For both the Wide channels and Extra-wide channels, the value of n is equal to 0.44. This matches the calculated value by the single channel extrusion experiment. Curiously, for the fit of the Murray's law network, $n = 0.87$. The apparent rheology of the organic wax in the Murray's law network is still shear-thinning, but is closer to a Newtonian fluid. This unexpected behavior could be explained by the experimental reality of power-law fluids: while the viscosity of a fluid may match a power-law model over a given range of shear rates, at very high and very low shear rates the fluids tend to exhibit plateau behavior akin to a Newtonian response. It is possible that the flow rates through the more resistive Murray's law network are so low that

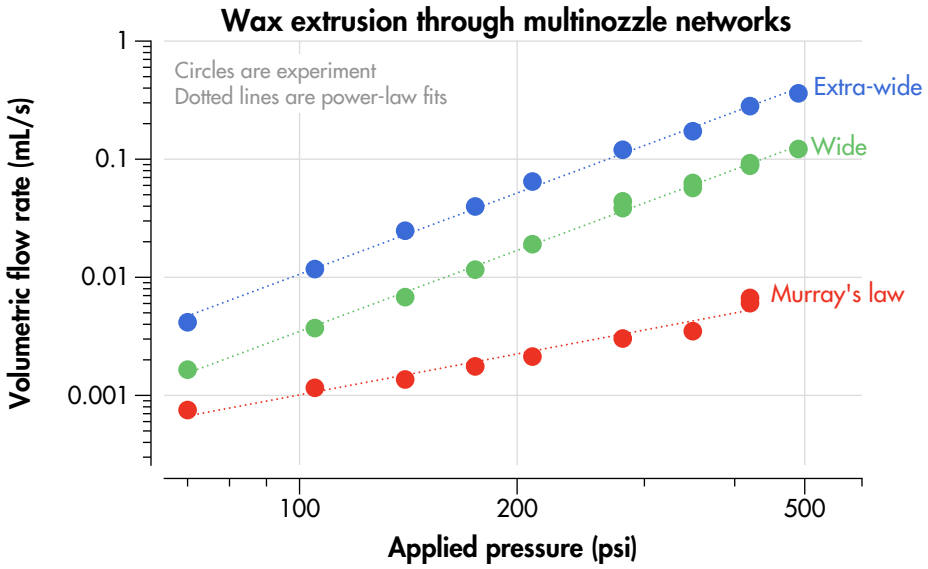

Figure 3.17: Log-log plot of volumetric flow rate of wax ink extruded through multinozzle networks versus applied pressure. Networks used in Figure 3.16, are cleaned of glycerol and the experiment is performed again with the organic wax ink.

the ink viscosity is approaching a plateau region. The Murray's law data set was repeated in order to determine if the anomalous results were due to an experimental error. This second dataset fits a power function with $n = 0.69$. While this value is closer to the expected value, it is still markedly different. It should be noted that the correlation of the Murray's law network data to their power fits are both weaker than the correlation of Wide channels and Extra-wide channels to their data: 98% for both Murray's law datasets and 99.8% for both Wide and Extra-wide datasets. The lower correlation of the Murray's law network data sets suggests that the accuracy of the experimental procedure may be limited at low flow rates.

3.3.3 1D and 3D modeling

While our experimental results (§3.3.2) are useful for comparing the hydraulic resistances of networks, mathematical models can yield the same results more easily and quickly. With these models, the systematic analysis of network geometry and its effect on flow rate can be performed. We use two methods of fluid modeling: The first is a custom-made script that employs the Hagen-Poiseuille equation, and is implemented in Matlab. The second uses COMSOL, a proprietary, finite element analysis, computational fluid dynamics software. While modeling fluid flow of through multinozzle network using COMSOL is much quicker than the physical experiment, it is still relatively time consuming. The modeling of a single straight channel can take a couple of minutes, while modeling an entire network can take

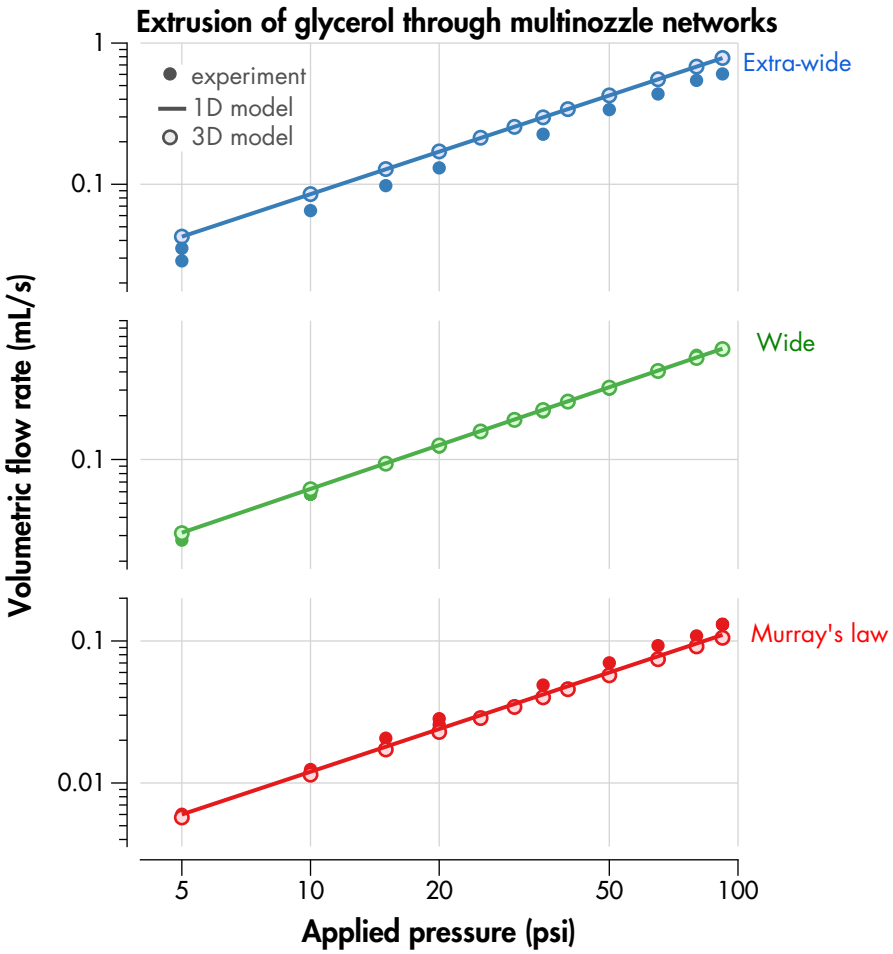

Figure 3.18: The experimental data of glycerol extrusion through network designs from Figure 3.16 is replotted with results from the 1D and 3D models. Data for each network is plotted in a separate log-log plot for clarity.

around 30 min. The power of COMSOL for computational fluid dynamics is that it can model complex 3D geometries, flow profiles, lamellar streamlines, and other relevant properties of fluids in channels. While these calculations can be useful, in this investigation, the focus is directed towards calculating pressure drops and average volumetric flow rates.

The Matlab modeling script was developed in order to simplify and speed up the fluid modeling process. In COMSOL, fluid velocities and pressures are calculated for every single mesh element of each channel (of which there can be hundreds of thousands to millions). But in the Matlab model, only a single volumetric flow rate and a pressure drop are calculated for each channel. While this speeds up the modeling time by a factor of roughly 10^5, there are some limitations. Namely, asymmetric flow profiles that might develop after bends in the channel will not be calculated. A brief COMSOL investigation (Appendix B) shows that this only becomes a problem when the Reynolds number approaches 1, while in our

Table 3.3 **Hydraulic conductances of networks with glycerol as the fluid (mL/psi-s)**

	Network designs		
	Murray's law	**Wide**	**Extra-wide**
experiment	1.40×10^{-3}	6.29×10^{-3}	6.67×10^{-3}
3D (COMSOL)	1.14×10^{-3}	6.24×10^{-3}	8.52×10^{-3}
1D (Matlab)	1.20×10^{-3}	6.28×10^{-3}	8.51×10^{-3}

experimental cases the typical Reynolds number is much smaller ($<10^{-4}$).

Several calculations are made to verify the accuracy of the computational models (1D Matlab and 3D COMSOL) to each other and to experiment. The experiment where glycerol is extruded through the Murray's law, Wide and Extra-wide networks at pressures from 5 to 92 psi, is modeled with both the 1D and 3D models. The results for each network design are plotted separately in (**Figure 3.18**) and are on a logarithmic scale for clarity. The conductances for the three designs and three measurement types are listed in **Table 3.3**.

For the three designs, the conductances predicted by the 1D and 3D models are within 6%. The calculated Matlab conductance for the Murray's law design is 17% lower than the experimental value; the two conductances are nearly identical for the Wide design; and the 1D conductance is 22% higher than the experimental conductance for the Extra-wide design. The good agreement between ($\leq 6\%$) the 1D and 3D models suggests that the Matlab script yields reasonably accurate flow rates for multiple geometries and over a wide range of flow rates. A partial explanation could be due to variations in ambient temperature. Before experimentation, the ambient temperature was measured between 22 and 23°C. Thus, the viscosity of glycerol at 22.5°C[56] (1.186 Pa-s) was used in both 1D and 3D models. A change in temperature ±1°C would result in the glycerol becoming less or more viscous, respectively, by roughly 10%. While it is curious that the trend of the predicted volumetric flow rates being below, at, and above the measured flow rate with increasing network conductance; this data is insufficient to form a conclusion based on this trend. The important conclusion from this comparison of data is that for the examined case of low-Reynolds number fluids, the 1D model provides a computationally fast and accurate alternative to the 3D model. While these models yield total network volumetric flow rates that differ significantly from experimental results, the models and experiments agree well within an order of magnitude.

The iterative 1D model is compared to a direct 1D solution for power-law fluids in ducts developed by Liu.[49] For values of n=1, both iterative and direct 1D models provide identical solutions. However, for values of n<1 and n>1, the predicted volumetric flow rate of the iterative relative to the direct model was exactly $(3 + 1/n)/4$. This factor is termed the Rabinowitsch correction factor and takes into account non-Newtonian effects on the shear

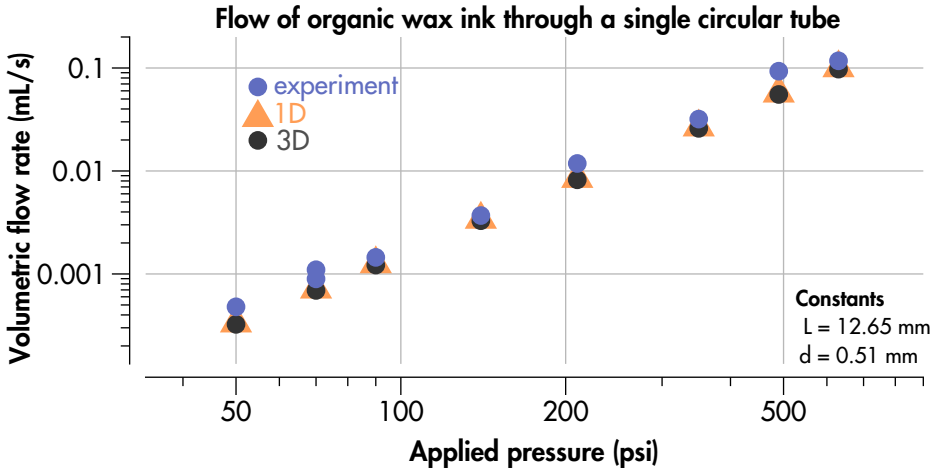

Figure 3.19: The 1D and 3D models are used to compute the volumetric flow rate for the wax ink through a single channel. These results are compared to experiment (the 510 µm data set in Figure 3.11).

rate.[55]

To account for this in the iterative model, a modified apparent viscosity equation is used:

$$\eta = \left(\frac{3 + 1/n}{4}\right)^n m\ \dot{\gamma}^{n-1} \tag{3.15}$$

When this correction factor is taken into account, the 1D iterative and direct models yield the exact same solutions for all values of n, all other parameters being equal (m, d, L, p).

The 1D model was modified to iteratively calculate the hydraulic resistances and volumetric flow rates of power-law fluids through bifurcating channel networks (described in §3.2.6). The accuracy of this iterative 1D model was compared to experiment and to the 3D model. In one case, a single, straight, circular channel, 0.51 mm in diameter and 12.65 mm long was used for the geometry (**Figure 3.19**). For applied pressures ranging from 50 to 630 psi, the volumetric flow rate of the organic wax through the channel ranged from 5×10^{-4} to 1×10^{-1} mL/s. It was well correlated to a power function fit ($Q = ap^{1/n}$) where n=0.44. The results yielded by the 3D and iterative 1D models both have exponents that match the experiment. However, their a values, which are proportional to the relative magnitudes of the volumetric flow rates differ. The 1D and 3D models have similar a values (within 3%), but are approximately 30% lower than the experimental value.

The experimental values of volumetric flow rates versus applied pressures for wax extrusion through multinozzle networks are compared to expected values calculated with the iterative 1D model and plotted in (**Figure 3.20**). For the Wide and Extra-wide designs, the calculated flow rates were roughly twice what was measured experimentally across all applied

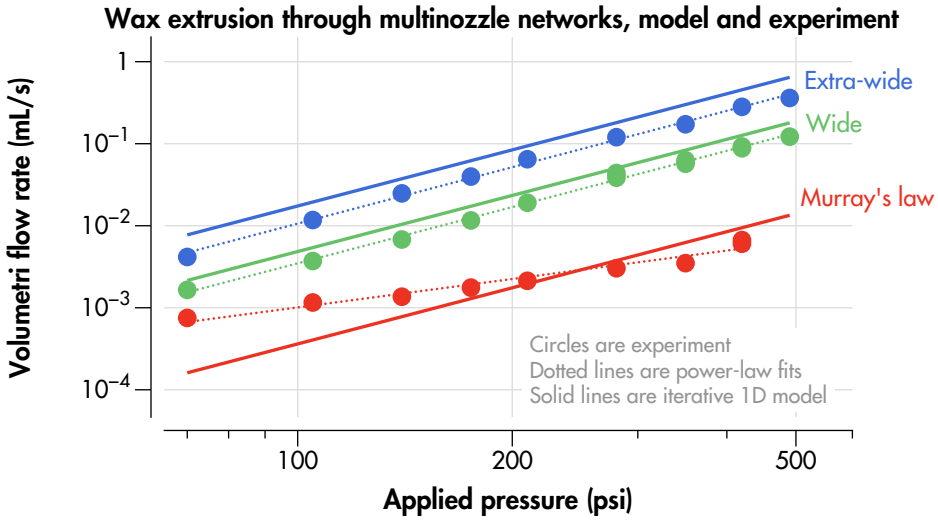

Figure 3.20: Log-log plot of volumetric flow rate of wax extrued through network designs versus applied pressure. The experimental data from Figure 3.17 plotted with expected values of iterative 1D model.

pressures. This discrepancy could be due to unaccounted pressure drops in the experimental setup. While the calculated flow rates for the Murray's law network are close the experimental values at some applied pressures (210 psi), the slopes of the two data sets do not match. This is possibly an experimental phenomena, as discussed previously (§3.3.2).

To verify the accuracy of the iterative model's ability to calculate relative volumetric flow rates, a 1-generation, bifurcating array was simulated in COMSOL (3D), and with the 1D direct and iterative models (**Figure 3.21**). In the geometry, the two child channels have the same diameter, but the left child-channel has half the length of the right child. For a Newtonian fluid twice as much material would be extruded per time through the left child (Q_{left}) compared to the right (Q_{right}) according to the Hagen-Poiseuille equation ($Q \propto d^4/L$). For shear thinning materials (n<1) the ratio Q_{left} to Q_{right} is exponentially greater than $Q_{\text{left}}/Q_{\text{right}}$ for Newtonian fluids (n=1). For shear-thickening materials (n>1), $Q_{\text{left}}/Q_{\text{right}}$ becomes slightly less the Newtonian value. The results of the direct and indirect 1D models are exact. These 1D models agree well with COMSOL simulation at four different values of n (0.44, 0.8, 1, 1.4).

To gain a better intuition in the behavior of power-law fluids, a brief study of 3 different types of 1-generation geometries is performed. In case (a) (**Figure 3.22**), the left child-channel has a length of 1 and diameter of 0.2 (relative units, as results are independent of the scale), while the right child has a length of 0.5 and diameter 0.168. Thus, for the case of Newtonian fluids (n=1), the flow rate through the left and right children will be equal as both children's hydraulic conductances ($\propto d^4/L$) are equal. For non-Newtonian fluids,

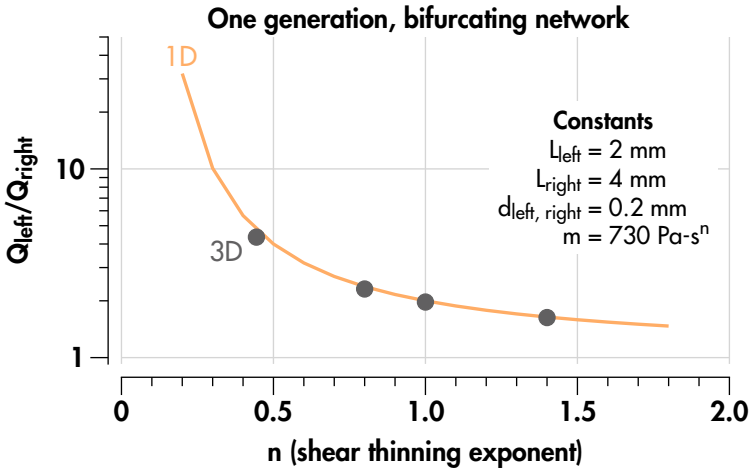

Figure 3.21: Relative volumetric flow rates calculated with 1D and 3D models for different values of shear thinning exponent, *n*.

the hydraulic conductance and volumetric flow rate are proportional to $d^{3+1/n}/L^{1/n}$. Thus, when n decreases below 1 (shear-thinning regime), the relative flow diverges strongly with more fluid flowing through the short, narrow (right) child than the long, wide (left) channel. When n increases above 1 (shear-thickening regime), the relative flow diverges weakly, but in the opposite direction more fluid flows through the wide, long channel. In case (b), the children have the same diameter, but the left child is half as long as the right. At n=1, the flow through the left is twice that through the right. With decreasing n the divergence of flow increases dramatically. As n increases about 1, the fluid tends closer to more even flow. In case (c), both children have the same length, but the right child has a diameter 84% ($0.84^4 \approx 0.5$) that of the left child. For the Newtonian fluid, the relative flow is the same as case (b) twice as much fluid flows through the left than the right. For the non-Newtonian fluids, the same left/right trend is observed, except the magnitude of the convergence is reduced. In the trivial case of both children have equal lengths and diameters, the flow through the left and right channels is equal for all values of n. The point of this study is to illustrate that if one is designing an asymmetrical network where the geometry is used to influence relative flow rates, the shear thinning behavior of the fluid must be taken into account. It should be noted that the results of this study are independent of the applied pressure and the value of m (power-law viscosity coefficient). While these variables influence the magnitude of the volumetric flow rates through channels, they have no effect on the relative flow rates from one channel to the next in a network.

While it is confirmed that the flow behavior of power-law fluids predicted by the iterative 1D model matches both the direct and 3D COMSOL models for a 1-generation bifurcating

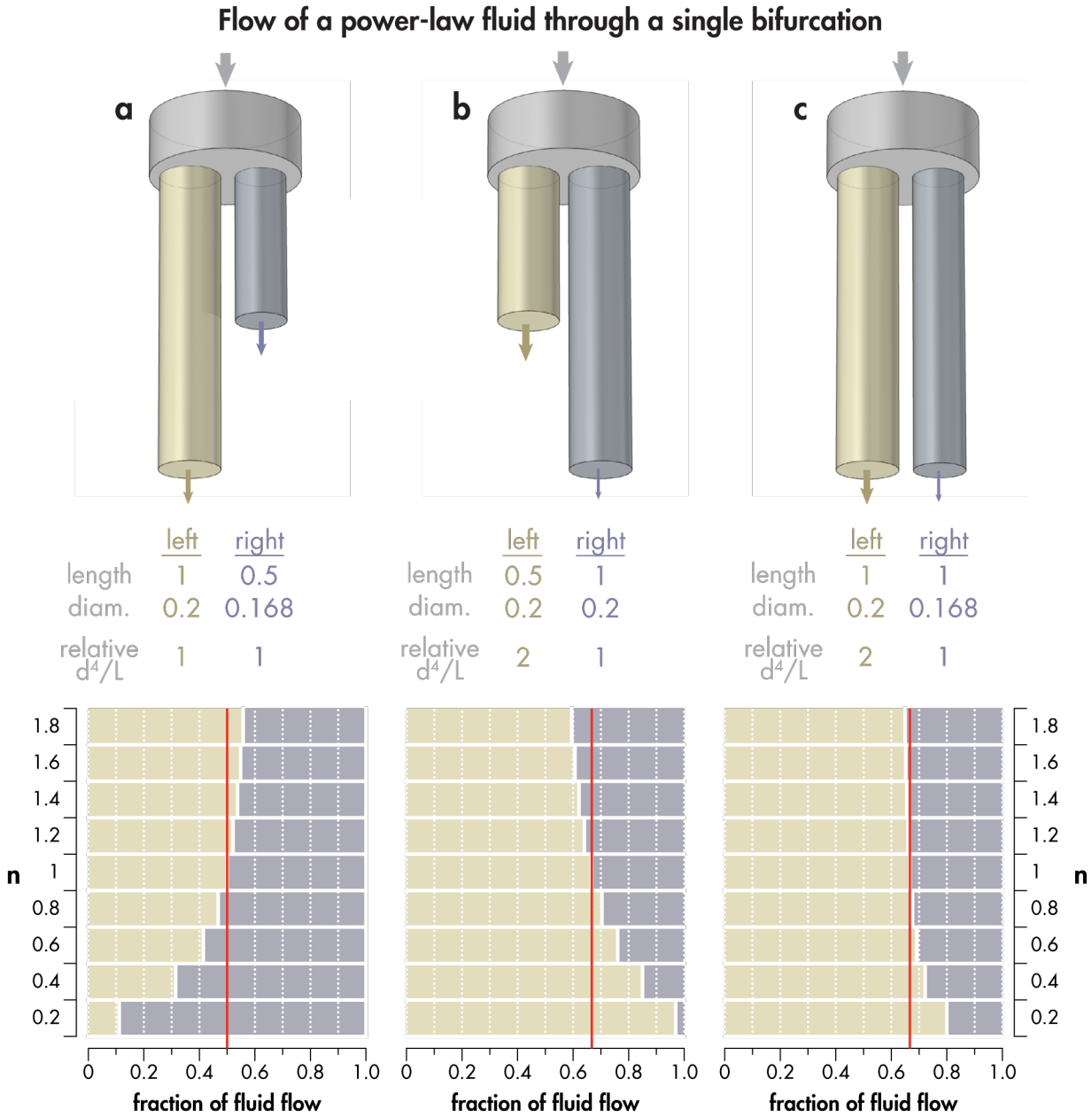

Figure 3.22: In case (a) the left channel is half the length of the right. Newtonian fluids (n=1) will flow at twice the rate through the left than through the right. For shear thinning fluids (n<1) an even greater fraction of the flow diverts through the shorter channel. For shear thickening fluids (n>1) the flow tends towards evenness. In case (b) both channels are the same length, but the diameter of the right is reduced to 84%, so the relative d^4/L ratios of (a) and (b) are the same. Dimensions of the channels' length and width are in arbitrary units. The red line indicates the value at n=1.

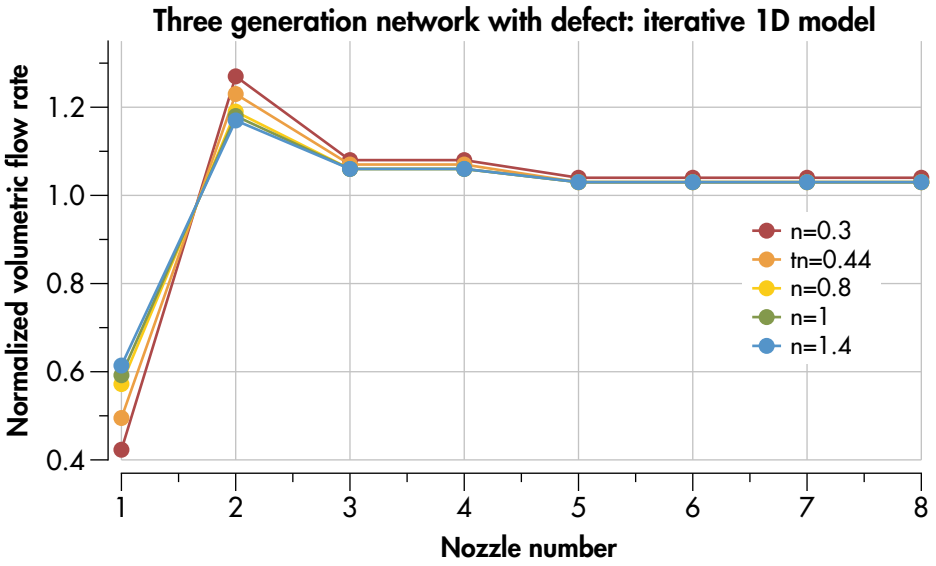

Figure 3.23: The output flow rates of 3-generation bifurcating network calculated by the iterative 1D model. The diameter of nozzle 1 is reduced to 84% simulating a clog or defect.

network, another brief study was performed to confirm the validity of the iterative 1D model for a 3-generation network. A 3-generation, bifurcating network, conforming to Murray's Law was modeled with the iterative model and compared to 3D model predictions. The eight output channels are all 2 mm long, with 0.2 mm hydraulic diameters, with the exception of the first channel, which has a hydraulic diameter of 0.168 mm. The relative volumetric flow rates of the 8 channels in the final (3^{rd}) generation are calculated by the iterative model and plotted in **Figure 3.23**. The reduced diameter of the first exit channel results in its flow rate is lower than the 7 others. Due to the bifurcating design of the network, the flow rates of the 4 exit channels on the opposite branch (numbers 5 through 8) are equal to each other and slightly higher than the average. This is because at the first junction, there is a slight increase in the hydraulic resistance in the left child compared to the right. The 2^{nd} generation junction in the left branch sees a similar trend, thus the two right-most nozzles of this branch (numbers 3 and 4) are even higher than the average. At the 3rd generation junction of the left-most branch there is a dramatic difference in hydraulic resistance between the left (nozzle number 1) and the right (nozzle number 2) and this is reflected in the very low flow rate in nozzle number 1 and very high flow rate in number 2.

The normalized flow rates calculated by the iterative 1D model are compared to those calculated by a 3D model. The differences for each nozzle is plotted in **Figure 3.24**. For the more highly shear thinning fluids (n=0.3, 0.44), the difference between the iterative 1D model and the 3D model for any given nozzle is less than 4%. When n=1 the differences

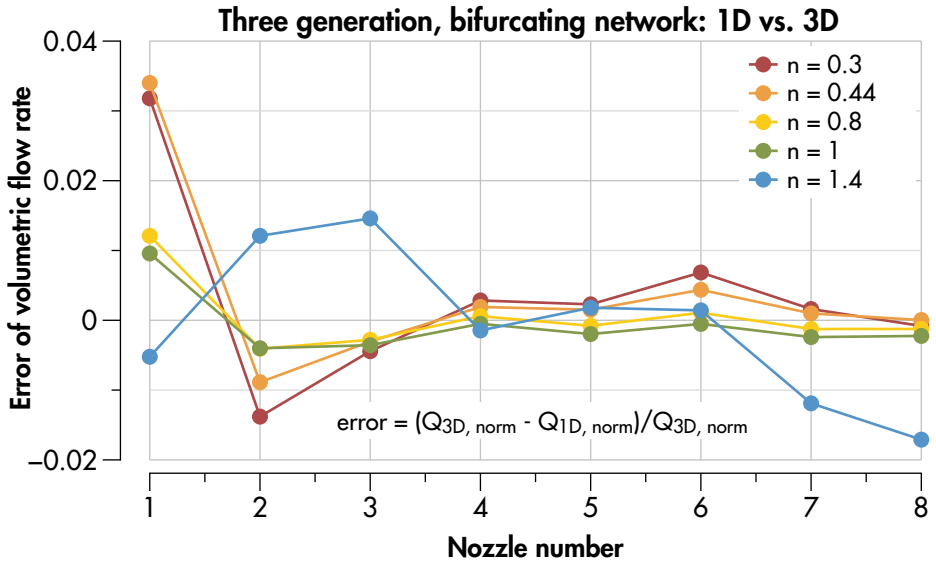

Figure 3.24: Error in volumetric flow rate for a given nozzle. The flow rates for the same 3-generation network in Figure 3.23 are calculated with the 3D and the relative differences are plotted.

are $\leq$1%. These differences are relatively small and the two models are qualitatively very similar. These results further support that the iterative model is a reasonable alternative to the COMSOL model for determining the effects of channel geometry on the evenness of flow rates across a microfluidic network.

With this establishment of a computational fast, relatively accurate 1D model for low-Reynolds number fluids in a bifurcating network, several systematic studies can be performed that analyze network designs for susceptibility to geometric defects (**Figure 3.25**). In the process of manufacturing a multinozzle, it is possible to unintentionally create a network where there is a linear variation in the length of the channels in the final generation. This occurs in the manufacturing step where the block assembly is placed in the vise on the mill for the encased nozzles to be opened to the environment. If the block assembly is askew in the vise, it will be machined at an angle resulting in uneven lengths for the final generation. Another defect can occur if the network-face of the channel block is polished unevenly so that the channel depths on the right side are deeper than on the left. For the multinozzle device to function properly, all of the filaments must be extruded at almost equal flow rates (experimentally determined to be within roughly 5%). In our study of the two types of geometric defects we calculated the relative range of volumetric flow rates for given angles of misalignment.

The relative volumetric flow rates of exit channels of the Murray's law, Wide and Extra-wide network designs are plotted (**Figure 3.26**) for a Newtonian fluid, where the angle of

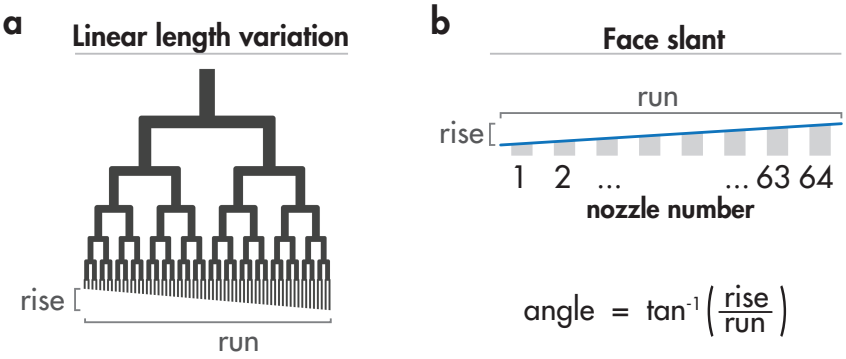

Figure 3.25: Two types of geometry variation. (a) The channels of the final generation (the nozzles) have equal hydraulic diameters, but the length of each varies. This geometry simulates a misalignment in the machining process. (b) The depth of channels in the entire network vary in depth from left to right. This simulates uneven polishing of the channel block prior to solvent welding.

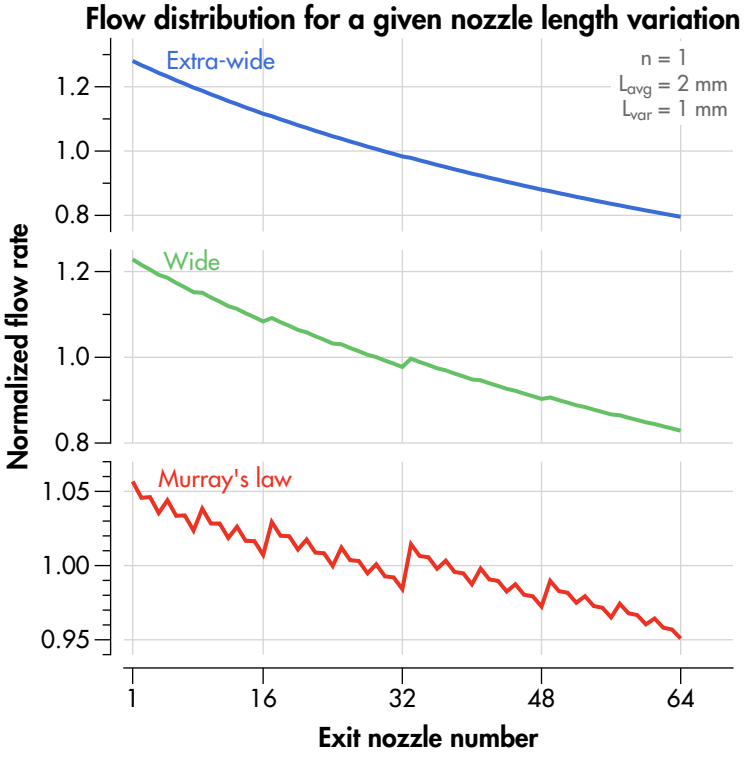

Figure 3.26: The flow rate distribution across the 64 nozzles for a length angle of 2.3°

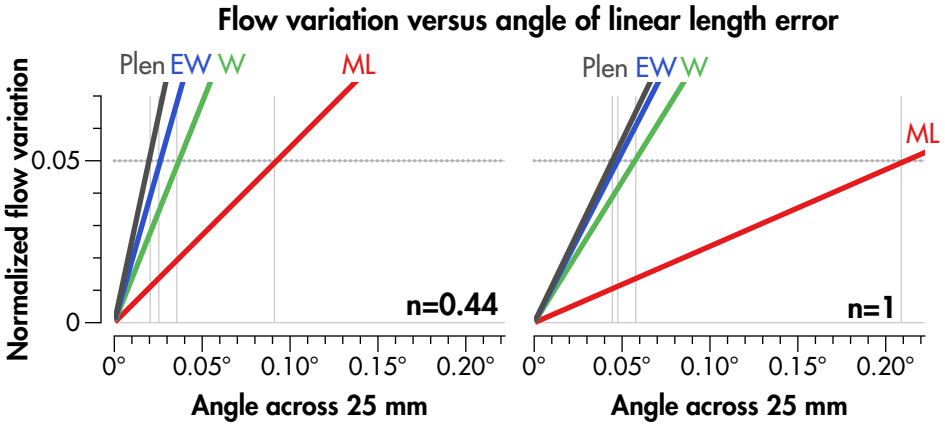

Figure 3.27: The range of flow rate variation for a given angle of length difference across the nozzles of each network design.

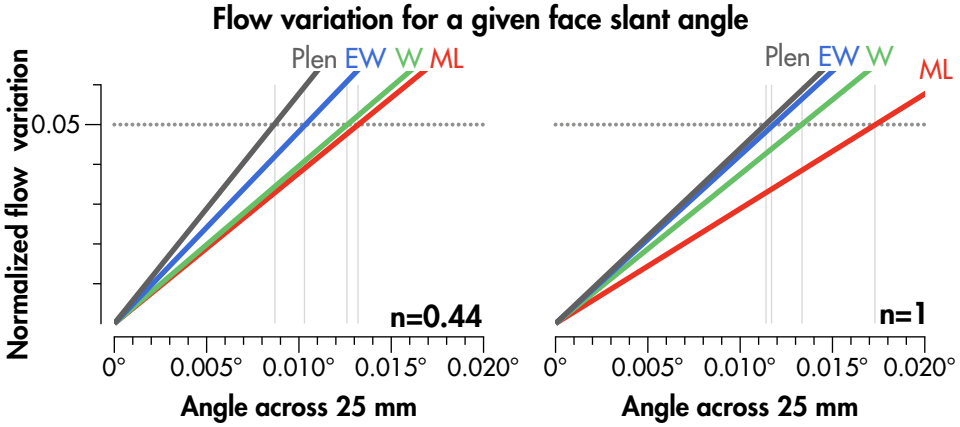

Figure 3.28: The range of flow rate variation for a given "slant" angle across each network design.

linear length variation is 2.3° (or 1 mm variation across ~25 mm). For all three designs, the flow rate is highest at exit nozzle number 1 (where the length is the shortest) and the flow rate is lowest at nozzle 64 (where the length is the longest). For the Murray's law design, the outputs flow rates have a jagged fractal pattern, as they tend to decrease from the shortest to longest channels. The fractal pattern is a result of the bifurcating nature of the network. In the cases of the Wide and Extra-wide designs, the decreases in flow rates from nozzles 1 to 64 are more monotonic. At the same length error, the flow rate distribution of the Plenum network is qualitatively similar to the Extra-wide network.

The linear length error tolerance of the various networks designs is calculated with the iterative 1D model. For each network design, the average length the exit nozzles (last generation channels) is kept constant at 2 mm, while the length of each nozzle varies linearly across the 64 outputs at angles between 0 and 0.2° (0 to ~0.1 mm over ~25 mm). The total variation in flow rates across the 64 outputs as a fraction of the average flow rate is plotted

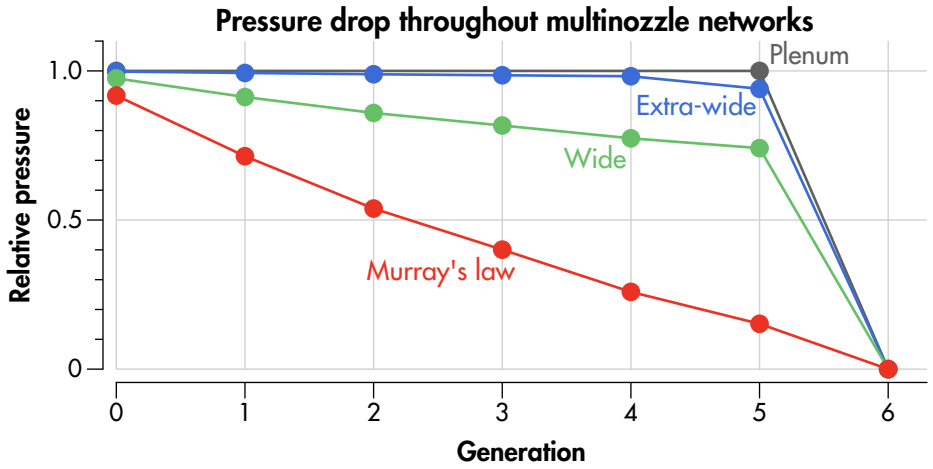

Figure 3.29: The relative pressure at the end of each generation of bifurcations in the multinozzle networks.

in **Figure 3.27**. These results are calculated for a Newtonian fluid (n=1) and for a shear-thinning power-law fluid (n=0.44). In general, the shear-thinning fluid is more susceptible to geometry variations than the Newtonian fluid. Also, for a given value of n, the wider designs are significantly more susceptible to geometry variations. For the least susceptible design, at n=1, the Murray's law network could tolerate a 0.21° length slant, while the most susceptible design, the Plenum design, can only tolerate 0.04° slant, while maintaining less than 5% flow variation. An angle of 0.04° over the width of the microfluidic network (~25 mm) is about 17 µm. For the shear-thinning wax ink (n=0.44) in the Plenum design, the tolerable variation is roughly 9 µm. In practice,-- the tolerance in length can easily be less than 10 µm. For the case of the face-slant defect, the flow rate variance is much more sensitive than the linear length error (**Figure 3.28**). This is because the face-slant defect alters the channels' effective hydraulic diameters, and the pressure drop is much more dependent on diameter than length ($\sim d^4/L$). For the shear-thinning ink, the Plenum design can only tolerate a linear variation in depth of about 4 µm across the entire output array.

To understand the susceptibility of the wider designs, it is helpful to plot the pressure drop after each generation in each of the different designs (**Figure 3.29**). In the Murray's law network, the pressure drop after each generation is approximately equal to one-sixth of the total pressure drop. Thus, only 15% of the total pressure drop occurs over the final generation. For the wider designs, the fraction of the total pressure drop occurring over the final generation is much higher. Specifically, for the Wide, Extra-wide and Plenum designs, the fractional pressure drops over the final generation are 74%, 94%, and ~100%, respectively. Because most of the pressure drop is concentrated at the final generations of the

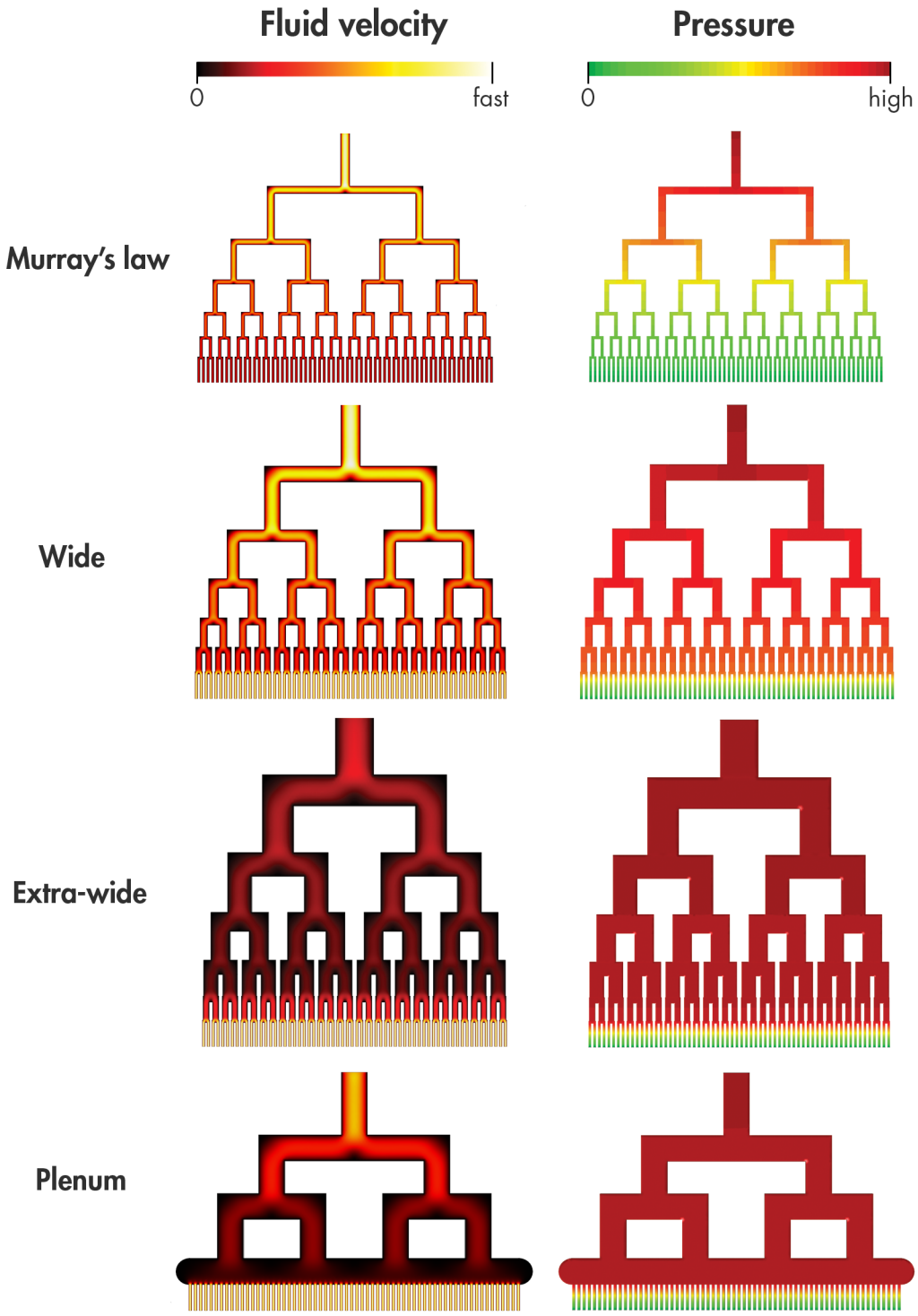

Figure 3.30: The steady state fluid velocity and relative pressure of multinozzle networks calculated with 3D COMSOL model. These results are for Newtonian fluids and are independent of applied pressure or ink viscosity.

wider designs, they are more susceptible to defects in the final generation. For visualization purposes, COMSOL modeling was used to illustrate the relative fluid velocities and pressure drops for the four network designs as shown in **Figure 3.30**.

It is clear that as the diameters of the upper generation increase, the majority of the pressure drop occurs over the exit nozzles. With the Plenum design nearly all non-nozzle pressure drop has been eliminated. Thus, the only way to reduce the pressure drop further is to reduce the length of the exit nozzles. Thus, reduced the length by a factor of 4 would reduce the pressure by the same factor. But in turn, the susceptibility to defects in the length of the nozzles increases accordingly. Additionally, shorter channels are also more susceptible to die swell. Die swell is a phenomenon where extruded filaments of molten polymer "swell" to diameters considerably larger than the channel they were extruded from (called the "die"). Generally, channels with smaller L/d ratios have more pronounced die swell.[57]

3.4 Conclusion

We established a direct 1D model to predict volumetric flow rates for Newtonian fluids in a microfluidic network. We adapted this direct model to an iterative 1D model to predict relative flow rates of power-law fluids through a network. We determined that shear-thinning fluids tend to greater variations in parallel flow rates for a given geometrical asymmetry. Of the four network designs investigated, the Murray's law network has the smallest total volume and is the least susceptible to defects in channel fabrications, which are both highly desirable properties. The Wide network has dramatically lower hydraulic resistance and has the highest conductance to volume ratio. The Extra-wide design has significantly higher hydraulic conductance than the Wide design. The Plenum design has marginally lower resistance compared to the Extra-wide design. Although the Plenum design is most susceptible to non-uniform flows arising from geometric defects, it is the easiest to produce by CNC milling.

It is intuitive to think that the Murray's law network would have the lowest resistance times volume product ($V \times R$), since Murray's law optimizes for a minimum metabolic power (proportional to volume) and a minimum power required to flow (proportional to hydraulic resistance). However, the Wide network has a lower resistance times volume product (**Table 3.4**). This is possible, because the power required for flow is also proportional to the volumetric flow rate. Murray's law optimizes for a minimum power equal to pressure *times* flow rate ($P_{\text{flow}} = pQ$). Our goal is to extrude filaments as fast as possible at low

pressures, so we are trying to minimize pressure *divided* by flow rate (p/Q). It makes sense that a network that is optimized for the vascular transport of nutrient rich-fluids may not be optimal for an industrial process that seeks to extrude ink as fast as possible.

Table 3.4 **Summary of microfluidic network resistances and volumes**

	Network designs			
	Murray's law	**Wide**	**Extra-wide**	**Plenum**
Relative hydraulic resistance	1	0.19	0.14	0.13
Total volume (mL)	0.04	0.14	0.52	0.45
Normalized resistance × volume	1	0.67	1.83	1.48

Chapter 4

High throughput printing via multinozzle printheads

4.1 Introduction

In this chapter, we use multinozzle printheads to print 3D woodpile lattices composed of 200 µm filamentary features over large areas (0.38 m^2) using an organic wax ink. The continuous negative volume of these lattices is infilled with a photo-curable epoxy resin. The epoxy solidifies after exposure to ultraviolet light, yielding a flexible, micro-patterned polymer architecture. The wax features can then be removed, leaving a continuous void network. These structures are of interest for polishing consumables used by the semiconductor industry for planarizing silicon wafers (§4.2.2). To the same end, an alternate approach is also explored. The wax and epoxy resin are deposited simultaneously using a dual multinozzle printhead in order to eliminate the lengthy infill process (§4.2.3).

We also explored other potential applications of multinozzle printing. First, we showed that varying the angle of the multinozzle printhead with respect to the printing direction allows one to so one can modulate the density of printed features (§4.2.4). Next, we produced a multinozzle printhead with the exit nozzles spaced far apart, which was used to print non-overlapping rows of arbitrary 2D structures (§4.2.5). Finally, three different functional materials— hydrogel and two colloidal inks—were deposited through multinozzle printheads as a proof-of-concept that these printheads can be implemented for patterning a broad array of functional inks (§4.2.6).

4.2 Experimental methods

4.2.1 Material systems

Five materials are independently extruded through the microfluidic network in a multinozzle printhead: an organic wax ink, a photo-curable epoxy resin, a polymer hydrogel, a ceramic particle ink, and a silver particle ink. The organic wax ink is composed of 60 wt% petroleum jelly and 40 wt% microcrystalline wax. The procedure for preparing the ink is

described elsewhere (§3.2.4) and in prior references.[58, 59] Wax inks of similar composition have been used previously for the creation of microvascular networks and microfluidic chaotic mixers.[60, 61] The photocurable epoxy resin is commercially purchased (NOA 61, Norland Products). It is a Newtonian fluid with a viscosity of about 0.4 Pa-s and a density of 1.2 g/mL at room temperature. Upon exposure to UV light, the resin solidifies and has an elastic modulus of roughly 1 GPa.[62] The material is optically transparent in both the uncured and cured state. The polymer hydrogel is composed of high molecular weight poly(2-hydroxyethylmethacrylate) (pHEMA) chains, HEMA monomer, ethylene glycol dimethacrylate (EGDMA) comonomer, a photoinitiator, and deionized water. The process for synthesizing this hydrogel ink is detailed by Hanson-Shepherd, et al.[12] This ink is shear-thinning, with a shear thinning exponent of $n = 0.56$.[12] For imaging purposes, a water soluble, yellow-green fluorescent dye (DFTB-C8, Risk Reactor) is mixed into the ink. The ink appears yellow under white light and green under UV light (365 nm). The ceramic ink is composed of commercially purchased copper oxide (CuO) nanoparticles dispersed in an aqueous solution. Features printed with this ink can be sintered in air, to form a solid CuO matrix. If the ink is sintered in an oxygen-free environment, the CuO will be reduced to elemental copper. Thus, the same ink can yield electrically resistive or conductive features depending on the annealing conditions, as shown by Kolesky and Lewis.[63] The silver ink is composed of silver nanoparticles dispersed in an aqueous solution. The ink is shear-thinning, has a yield stress and can readily be printed out-of-plane. The ink is electrically conductive as-printed and achieves a conductivity comparable to bulk silver after annealing.[64] This ink has been used to pattern planar and spanning microelectrodes and transparent conductive grids.[64, 11]

4.2.2 Printing and infilling woodpile lattice pads

Polymer woodpile lattices (**Figure: 4.1**) are printed with a 64-output, 200 µm feature size multinozzle printhead using the organic wax ink. The printhead is mounted onto a custom-built rotation stage, and this rotation stage is then mounted to a three-dimensional positioning gantry (ABG10000, Aerotech). High-pressure pumps (500D, Teledyne Isco) supply the wax ink through a hydraulic hose and into the input of the printhead. The printhead is mounted such that input is at the central opening in the rotation stage and is oriented upwards. The ink flows downward through the bifurcating arrays and is extruded through the exit nozzles, which are oriented to the bottom. The 3-axis gantry positions the bottom of the printhead 200 µm above a circular glass plate. A thin coating of release agent (2,2,4-trimethylpentane, Buehler) is wiped on the piece of glass. The release agent prevents

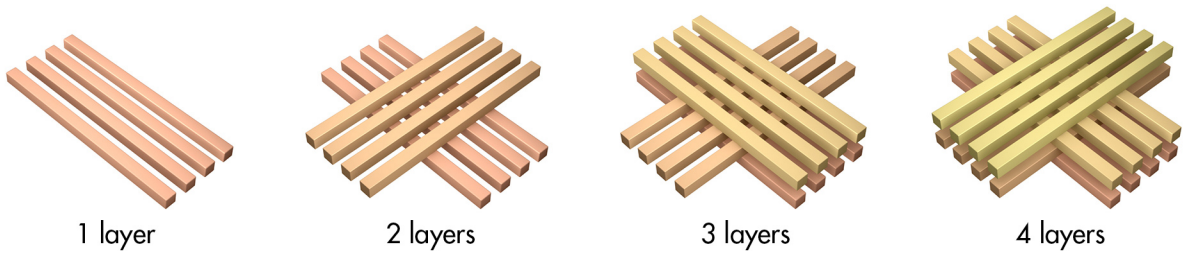

Figure 4.1: Schematic of a woodpile structure. A layer is a set of parallel filaments. Each additional layer is oriented 90° relative to the layer below

the cured epoxy from strongly adhering to the glass. The angle of the rotation stage is adjusted such that the line of exit nozzles is perpendicular to the printing direction. The pumps are set to apply a pressure between 200 and 850 psi. The gantry makes a linear movement across (614 mm) the glass plate at a constant velocity between 5 and 40 mm/s. The stripe produced by the printhead consists of 64 parallel filaments, 200 µm wide and 200 µm tall. The filaments are separated by a gap of 200 µm. At the end of the first linear movement, the gantry moves perpendicularly a distance equal to the width of the printed features (25.6 mm), returns an equal distance in the opposite direction, and then moves laterally another 25.6 mm. This sequence of two stripes and two lateral movements forms a serpentine raster pattern that, when performed 12 times, forms the first layer of the woodpile structure (**Figure: 4.2**). The overall area of the first layer is 614 mm × 614 mm. After the first layer is completed, the gantry moves laterally away from the pad, the rotation stage rotates the multinozzle printhead 90°, the gantry moves vertically 200 µm (equal to the height of the filaments), and then prints a serpentine pattern similar, but perpendicular to the first layer. This process repeats until a total of four layers are printed. The overall dimensions of the completed structure are 614.4 mm × 614.4 mm × 0.8 mm.

After the structure is printed on a circular piece of glass (800 mm diameter, 6.35 mm thick) with wings (150 mm × 100 mm) on the left and right hand sides, a wax border (2 to 5 mm wide and tall) is placed around the perimeter of the glass plate. The purpose of this border is to laterally contain the liquid epoxy that will infill the printed structure. Just outside of the wax border, 2 mm thick spacers are placed around the circumference of the board approximately every 100 mm. A second circular glass plate (800 mm diameter, 6.35 mm thick) without wings is placed overtop the first glass plate. The downward face of the top glass plate is covered with a layer of release agent. The spacers prevent the top plate from collapsing onto the printed structures and the wax border squishes to form an airtight seal around the edges. The spacers allow for a 1.2 mm high space above the printed structure (**Figure: 4.3**). Photocurable epoxy resin (NOA 61, Norland Products) is loaded into a 500

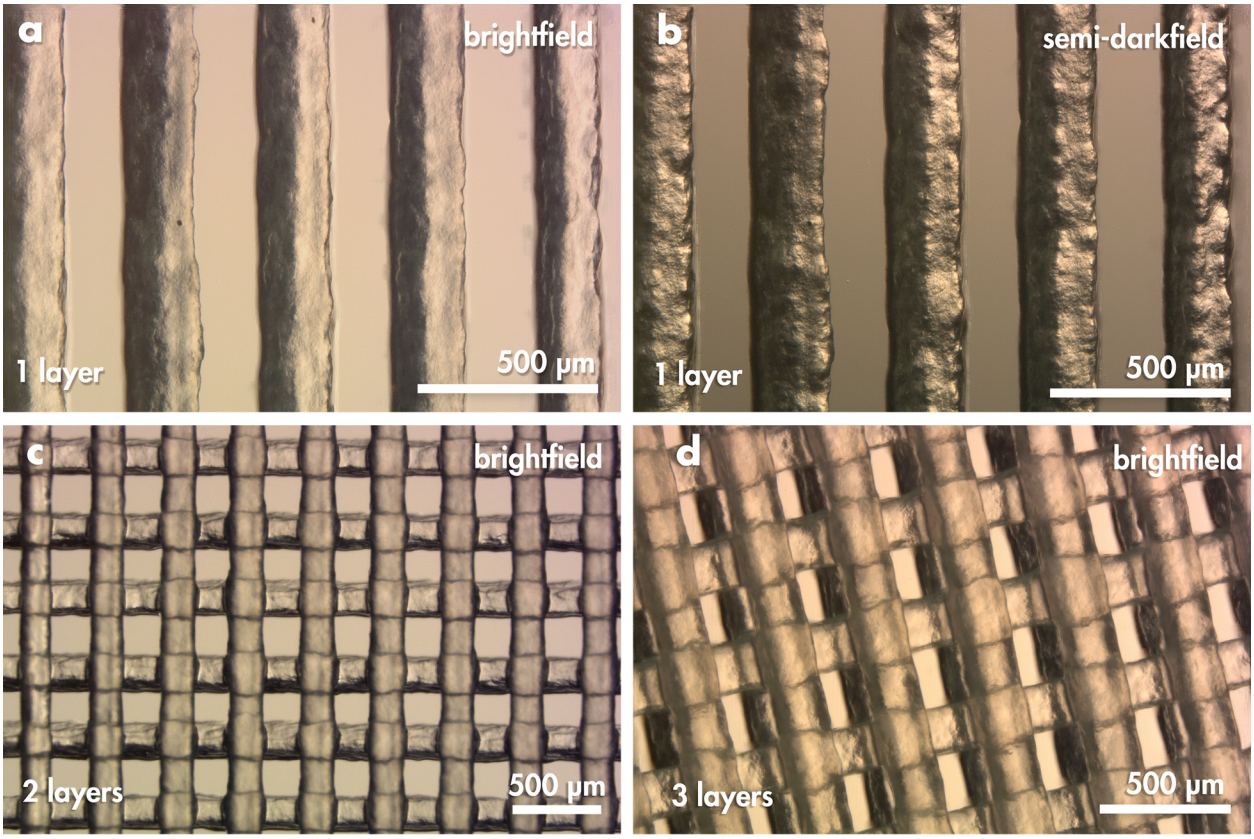

Figure 4.2: Wax filaments extruded from a multinozzle printhead (device #13.1) imaged with a Zeiss Discovery V20 stereomicroscope. (a) A single layer imaged in brightfield. (b) The same field of view as (a) but in semi-darkfield. (c) Two layers of a woodpile structure. (d) Three layers of a woodpile structure imaged at an angle.

mL titration bulb. The bulb is set to drip at a rate of approximately 0.3 mL/min. The liquid epoxy drips onto one of the wings of the bottom glass plate. Capillary forces draw the epoxy between the glass plates and within the printed structure (**Figure: 4.4**). The pressure of the epoxy in the wing-reservoir pushes fluid over the bulk void space above the structure. The resin is set to drip at a rate slow enough that it infiltrates the network ahead of the bulk void space. After around 24 to 48 h, the epoxy has completely filled in the negative volume within the structure as well as the volume above the structure. Ultraviolet lights (XX-20BLB, 365 nm, Black Ray®) are suspended approximately 150 mm above the top glass plate and the lights are repeatedly translated laterally above the epoxy sandwiched between the glass plates. After 8.5 h of exposure, the two glass plates are flipped over and the underside is illuminated for an additional 3.5 h. After curing, the glass plates are pried apart and the cured epoxy is peeled off of the glass. In order to remove the fugitive wax ink from the epoxy pad, the pad is soaked in a bath of hexanes (Sigma-Aldrich) for 3 h, and then sprayed with hexanes with a wash bottle until all of the wax is removed. The soak partially

dissolves the wax and the spray bottle mechanically washes it out. After this cleaning step, the pad is ready to be punched out and used by our collaborators in polishing experiments (**Figure: 4.5**).

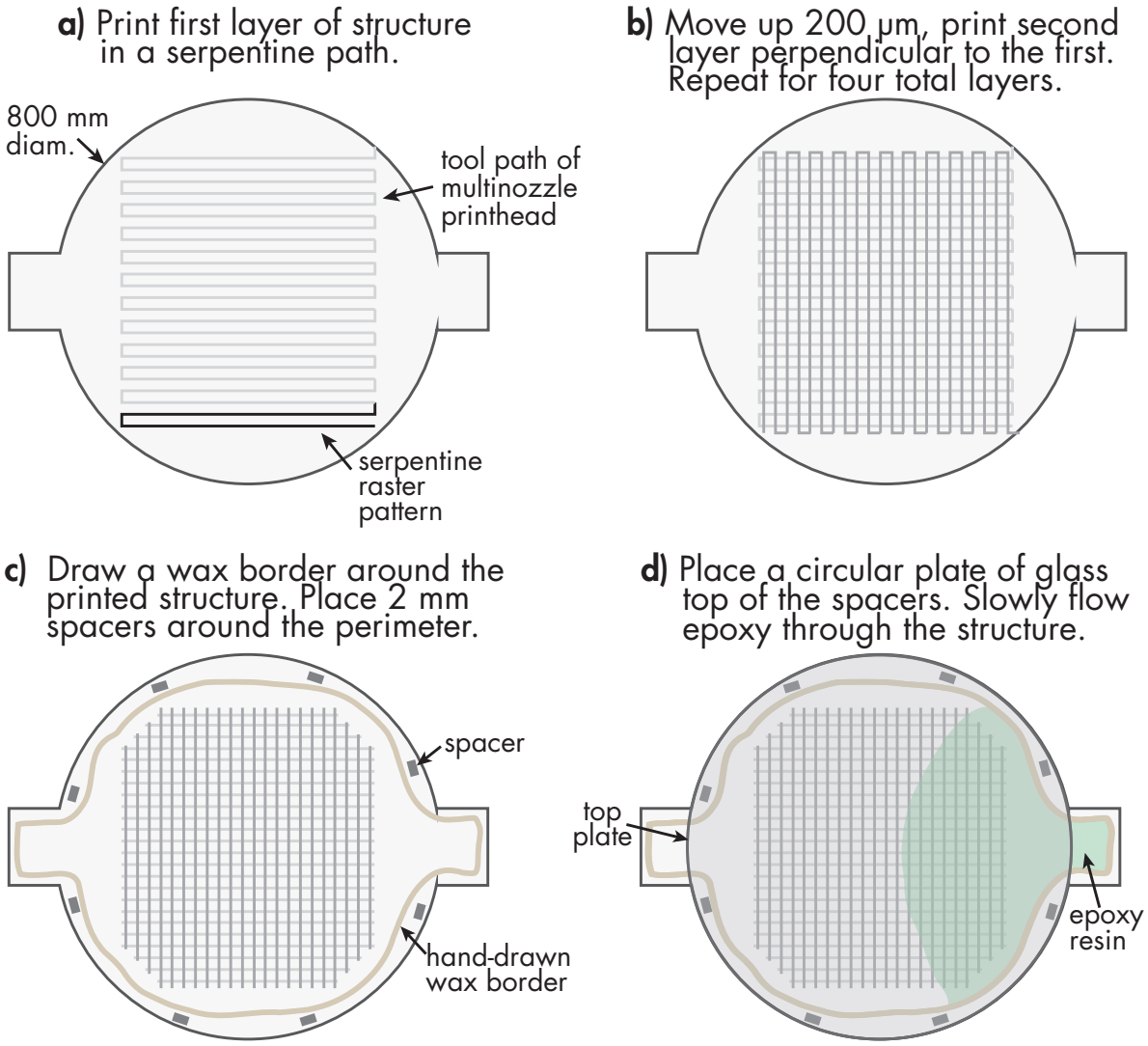

Figure 4.3: Procedure for printing a 614 mm (24″) square 3D microperiodic lattice.

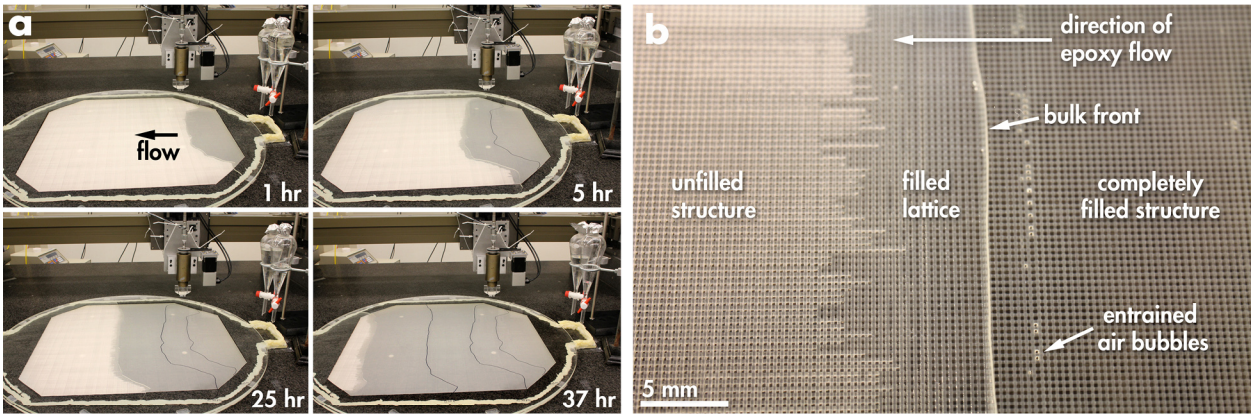

Figure 4.4: Infilling the lattice microstructure. (a) Titration bulbs dispense resin that slowly fills in the voidspace of the structure. b) Close-up of the resin "front" as it moves across.

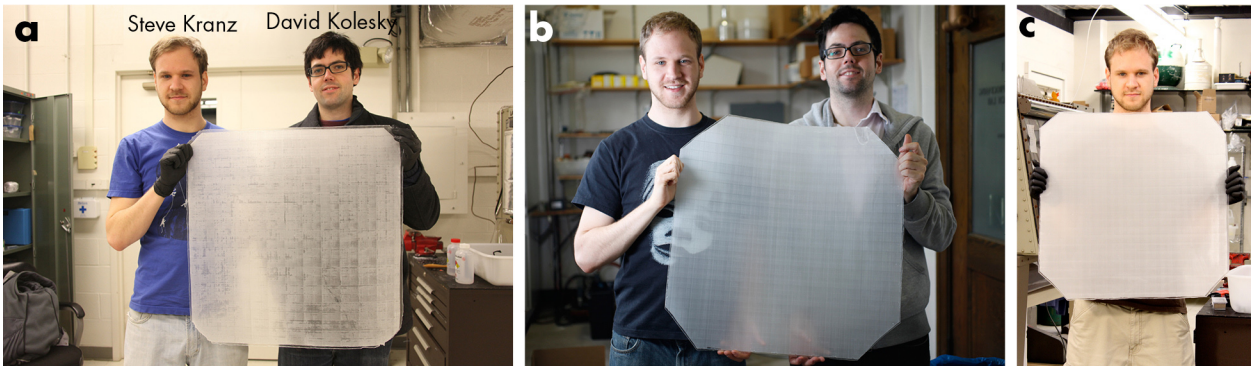

Figure 4.5: Completed microstructured pads. (a) Printed in Jan. 2012 with device #8.3. (b) Printed in Apr. 2012 with device #9.6. (c) Printed in July 2012 with device #13.1.

4.2.3 Co-infill epoxy pad process

During the infiltration process, epoxy drips onto a reservoir and is slowly pulled in between the glass plates until the epoxy covers the entire printed structure. The rate at which the epoxy covers the pad depends on the volumetric drip rate from the titration bulb. Since the space above the pad (1.2 mm vertically) is much larger than the void space within the printed structure (200 µm × 200 µm in cross section), the epoxy resin flows more easily over the structure than into it. If the volumetric flow rate of the epoxy resin is too high, the liquid will flow over the top of the structure faster than it can penetrate the lattice. In this case, bubbles will be entrained and the cured epoxy pad will not have the desired microstructure. In order for the epoxy resin to fully infiltrate the microstructure the volumetric flow rate must be slow enough (0.2 to 0.4 mL/min) for the liquid to be drawn into the microstructure ahead of the bulk flow on top. This slow rate means that the infiltration process of a large

area pad (0.38 m^2) requires between 24 and 48 h.

To obviate this lengthy infill step, we attempted a process of co-infiltration, in which the wax filaments and epoxy are deposited simultaneously. To accomplish this, we built a multinozzle printhead with two parallel, but offset bifurcating networks.[1] Wax filaments extrude from one array and the Newtonian epoxy flows through the other array, filling in the space between the filaments.

The co-infill printhead is mounted to the 3D printer rotation stage similarly to the single-deposition multinozzle (§4.2.2). The printhead is oriented such that the line of exit nozzles of both networks is perpendicular to the printing direction; the wax network leads the epoxy network. The writing speed is around 10 mm/s. The applied pressure of the wax is ~500 psi and the applied pressure of the epoxy is ~5 psi. As the gantry translates the printhead across the glass substrate, 64 wax filaments are extruded in parallel and the void spaces are immediately filled in with the epoxy. After the first pass, the printhead translates 25.6 mm (one path width) perpendicular the printing direction, rotates 180°, and then prints a second row, again with the wax leading the epoxy. The printhead moves perpendicularly another 25.6 mm, rotates 180° and the serpentine pattern repeats.

4.2.4 Adjustable fill factor multinozzle printhead

The "traditional" multinozzle printhead was developed to increase the throughput of printed 3D woodpile lattices. For this purpose the microfluidic network consisted of six bifurcations (64 outputs), with each output having a 200 µm × 200 µm square cross-section. The center-to-center spacing of these outputs is 400 µm. When printed, this leaves a 25.6 wide stripe of 64 filaments with a 0.50 fill factor. That is, half of the 25.6 strip is filaments, and the other half is void space. For the "adjustable fill factor" multinozzle, we adapted the bifurcating network of the printhead to allow us to print alternate architectures. For this application, the multinozzle has four levels of bifurcations (16 outputs) with each 200 µm × 200 µm output having a 1.6 mm center-to-center spacing. This yields a stripe with a 0.125 fill factor. When the row of output nozzles is perpendicular to the printing direction, the printing fill factor is a minimum. If the printhead is rotated such that the row of nozzles is at some other angle with respect to the printing direction, the effective spacing between decreases, while the width of the filament remains essentially constant. This results in a narrower, but high density printed path (**Figure: 4.6**).

If the cross-section of a single extruded filament is circular, the apparent width of a deposited filament (as measured from directly above) would be equal to the filament's diameter, regardless of the angle printed. That is, $w = w_0$, where w is the apparent width and w_0

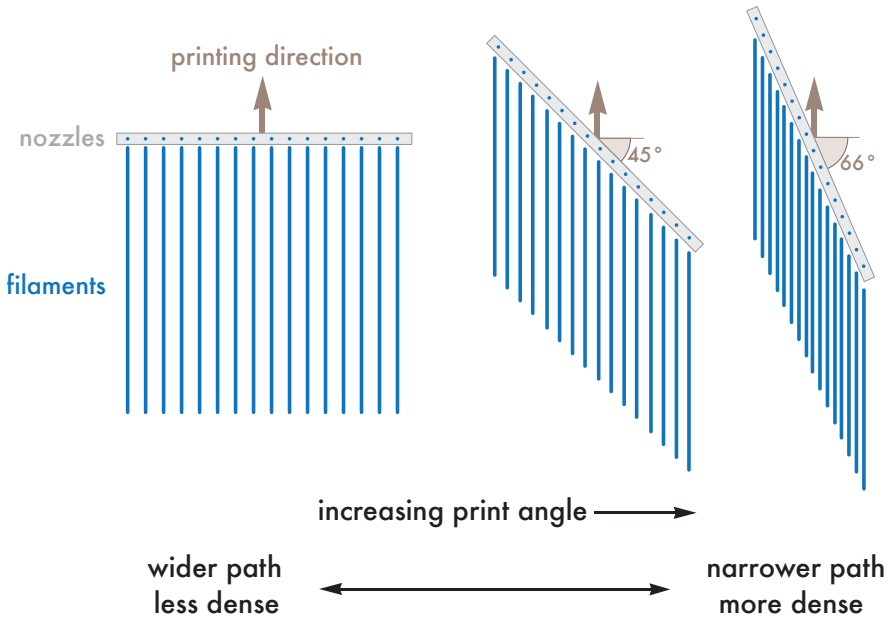

Figure 4.6: Schematic of the adjustable fill factor multinozzle printhead. As the print angle (orthoganal to the printing direction) increases, the printed path becomes denser and narrower.

is the diameter of the filament. If the filament's cross section is square (which is the case for multinozzle printheads), The apparent width of the deposited filament may depend on the print angle. When the print angle is 0° from normal to the printing direction, the apparent filament width should be equal to the edge length off the square cross section. However, if the print angle is 45° from normal to the printing direction, one might expect the apparent width to be $\sqrt{2}$ times the edge length (the length of the square diagonal) (**Figure: 4.7**). Hence, for the square cross section, $w = w_0/\cos\theta$, where w_0 is the edge length of the square, and θ is the print angle (with respect to the normal of the printing direction). The center-to-center spacing of the filaments for both circular and square cross sections is, $c = c_0 \cos\theta$, where c_0 is the center-to-center spacing at $\theta = 0$. The apparent width is important because it effects the calculation of the print angle-dependent fill factor of deposited features. Since the angle dependent fill factor is given by fill factor $= w/c$, where the fill factor for circular filaments is given by:

$$\text{fill factor}_{\bigcirc} = \frac{w}{c} = \frac{w_0}{c_0 \cos\theta} \tag{4.1}$$

and the fill factor for square filaments is given by:

$$\text{fill factor}_{\square} = \frac{w}{c} = \frac{w_0}{c_0 \cos^2\theta} \ . \tag{4.2}$$

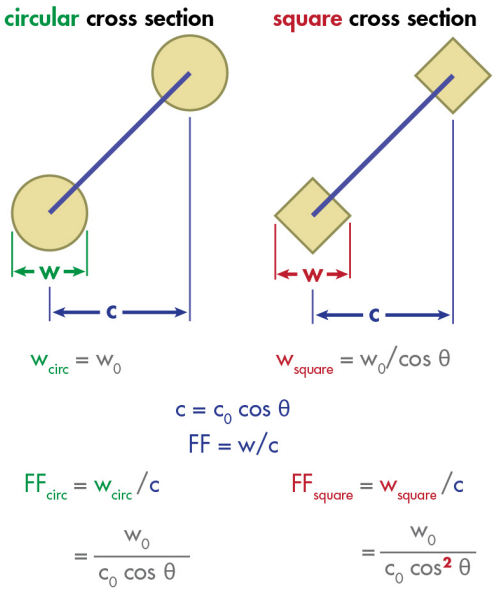

Assuming
w_0 = 0.2 mm
c_0 = 1.6 mm

theoretical fill factor	angle (square)	angle (circular)
0.125	0°	0°
0.250	45°	60°
0.375	54.7°	70.5°
0.500	60°	75.5°
0.625	63.5°	78.5°
0.750	66°	80.5°
0.875	68°	82°
1.00	69.3°	82.75°

Figure 4.7: Calculating the fill factor (FF) dependence on print angle.

4.2.5 Wide-spaced multinozzle printheads

In another adaptation, we created a three-generation (8-output) multinozzle printhead with the center-to-center spacing between nozzles of 8 mm. The large center-to-center spacing of the exit nozzles with respect to their dimensions (200 µm × 200 µm) allows arbitrary two-dimensional structures to be printed in parallel without overlapping one another.

4.2.6 Multinozzle deposition of functional materials

While the multinozzle printheads were initially designed to be used with the organic wax ink, we investigated the use of other inks that could theoretically be deposited with the printhead. One ink was a poly(2-hydroxyethylmethacrylate) (pHEMA) hydrogel, which has been used to create 3D hydrogel scaffolds for culturing neuronal cells. This ink was prepared as described by Hanson-Shepherd, et al.[12] The next ink was a copper oxide particle ink. [63] The final ink was a silver nanoparticle ink that has been used to pattern electrically conductive features on flexible substrates. This ink was prepared as described by Ahn, et al.[64].

4.3 Results and Discussion

4.3.1 Printing and infilling woodpile lattice pads

Four-layer, 0.38 m^2 woodpile lattice pads were printed separately with two different network designs: Murray's law and Wide channels. The most successful pad printed with a Murray's law network design (device #9.6) was printed with the organic wax ink applied at 500 psi pressure, and a print speed of 5.5 mm/s (**Figure: 4.8**). The most successful pad in terms of high print-speed, low-filament breakup, and square-ness of filaments was printed using a Wide channel multinozzle printhead. At an applied pressure of 750 psi, and a print speed of 40 mm/sec, the pad was printed in about 25 minutes (**Figure: 4.9**). Prior to the introduction of the multinozzle printhead, these woodpile lattice pads were printed with a nozzle depositing a single filament at around 50 mm/s, and took approximately 24 h to complete an entire 0.38 m^2 pad. Thus, the Murray's law and Wide channel printhead designs resulted in increased throughputs of approximately 8 and 64 times.

4.3.2 Co-infill epoxy pad process

While the co-infiltration process works in theory, there are several problems that arise in practice that make it less effective than the print-then-infill procedure. The wax filaments of the first layer extrude and lay down evenly and the epoxy fills in the void space almost entirely. However, for the epoxy to completely fill in the void space, it must be over-pumped, i.e., pumped at a greater volumetric flow rate than is required to only fill in the void space. As a result, epoxy fills in the void space, but excess epoxy is also deposited on top of the wax filaments. The wax filaments on the second layer must be printed on a surface of wax covered with epoxy. The excess epoxy hinders the adhesion of the wax filaments to the underlying filaments leading to defects. Most typically these defects are wandering filaments that have detached from the scaffold and float laterally along the structure (**Figure: 4.10**).

We found that the process of co-infiltration is less reliable than print-and-infill. Most importantly, with co-infill it is difficult to deposit defect-free filaments on multiple layers. While high quality lattice structures can be readily patterned with a single-deposition multinozzle printhead, to date, the co-deposition technique has not produced comparable results. Also, the printing speeds of co-deposition (<10 mm/s) are significantly slower than the single deposition process (40 mm/s). This increases the total deposition time from about 25 min (single deposition) to over 2 h (co-deposition) for a 0.38 m^2 lattice. While the infill process can take between 24 and 48 h, it requires only minimal equipment (titration bulbs) and in theory, multiple 3D lattices could be infilled in parallel.

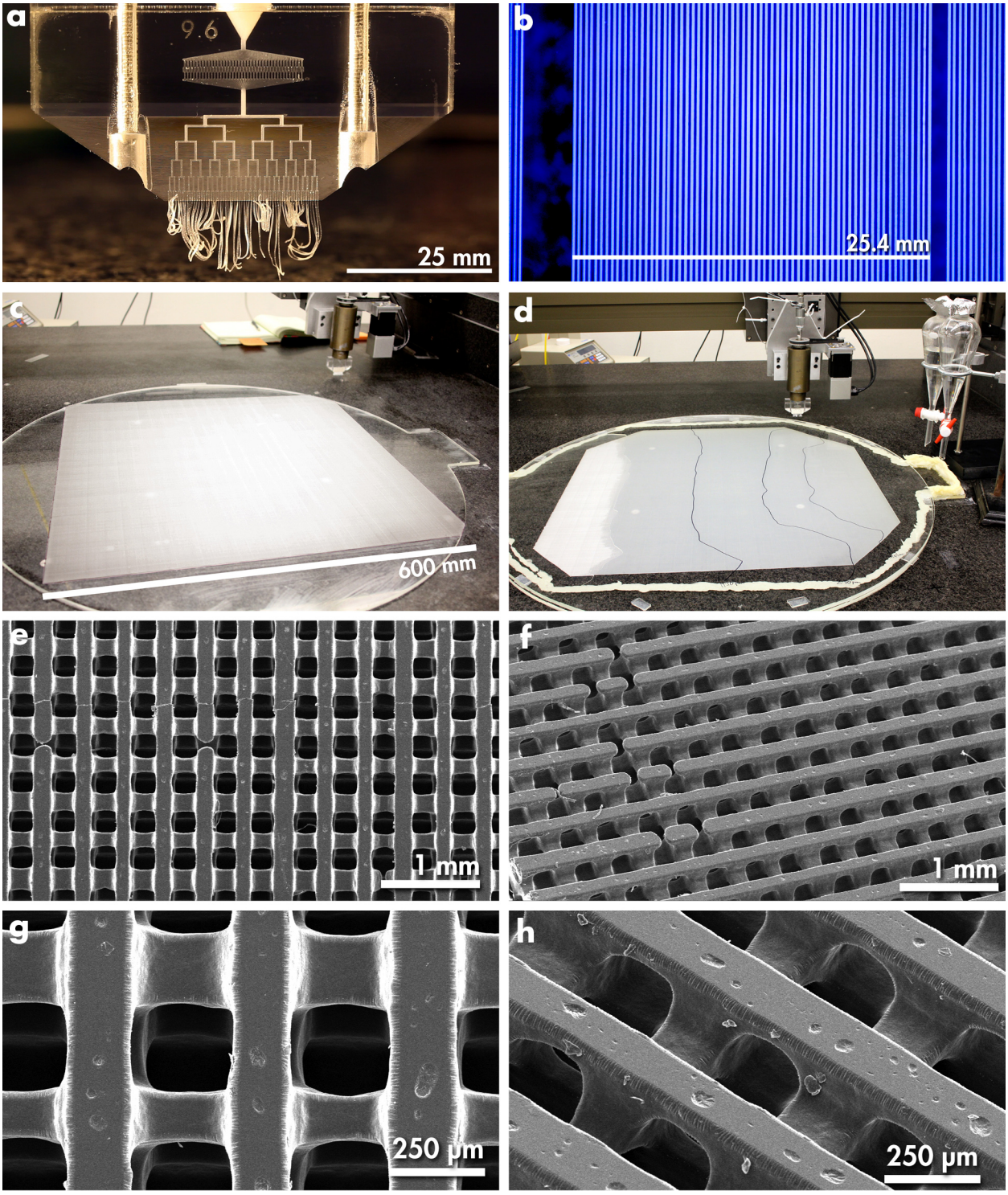

Figure 4.8: Creating a pad with device #9.6. (a) The multinozzle printhead. (b) One layer of filaments deposited with device #9.6. The wax ink auto-fluoresces blue under UV. (c) The completed printed wax structure. (d) The pad during the infilling process. (e-h) SEM micrographs of the cured and cleaned epoxy pad.

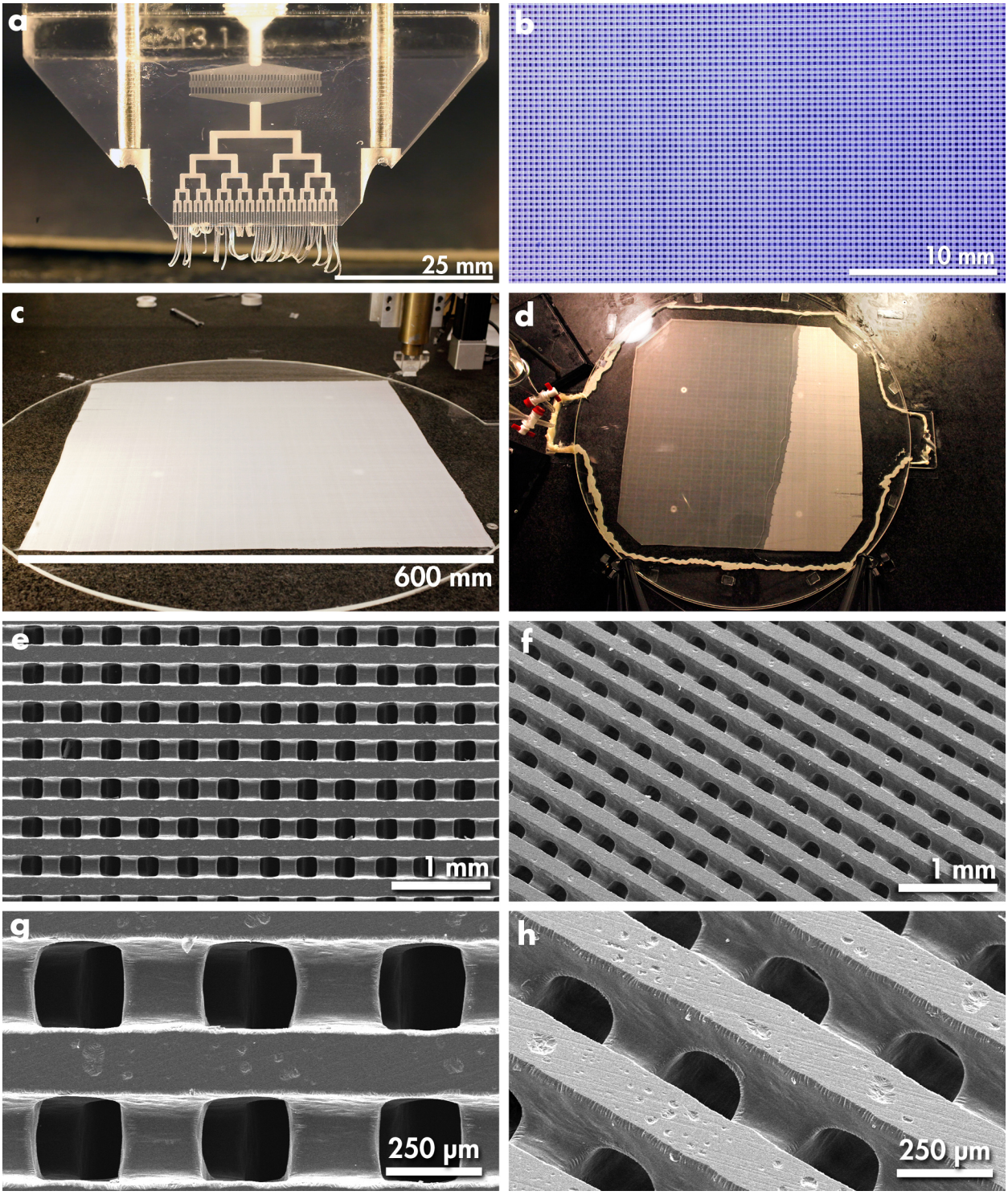

Figure 4.9: Creating a pad with device #13.1. (a) The multinozzle printhead. (b) Two layers of filaments deposited with device #13.1. (c) The completed printed wax structure. (d) The pad during the infilling process. (e-h) SEM micrographs of the cured and cleaned epoxy pad.

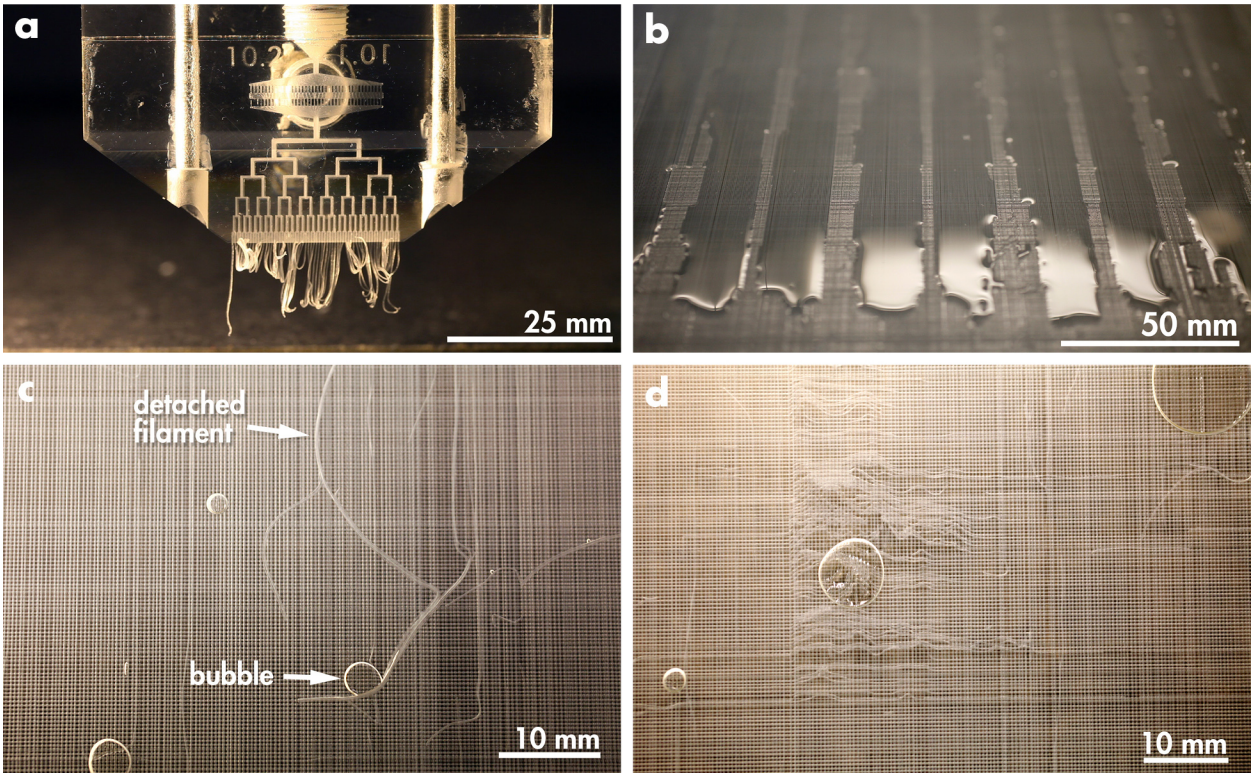

Figure 4.10: Co-infiltration printing. (a) A dual-deposition multinozzle printhead. (b) Eventually, excess deposited epoxy pools due to surface tension. (c,d) Structure printed with dual-deposition multinozzle. Filaments can break off and float or "wander" away.

4.3.3 Adjustable fill factor multinozzle printhead

A multinozzle printhead (device #16.1) with 1.6 mm center-to-center spacing and 200 µm square outlets was used at a range of print angles in order to deposit single layers of wax at fill factors ranging from 0.125 to 1.0. Two sets of angles were used: one set assumed the filament cross-sections were circular; the other assumed the cross-sections were square. After depositing the striped filaments at the defined angles, the stripes were illuminated with UV light which made the organic wax ink fluoresce blue. The stripes were photographed (Rebel T3i, Canon) then using ImageJ, the photographs were thresholded such that the filaments were entirely white pixels, while the background was entirely black. The ratio of white pixels to total pixels was used to calculate the fill factor. The filaments were intended to have a width of 200 µm when printed at 0°, however, too much pressure was applied and the filament width was closer to 250 µm. This value was used for w_0 when calculating the theoretical fill factors. Plotting the experimental data sets against the two theoretical models, it is clear that the experimental data is much closer to the "circular" curve than the "square" curve (**Figure: 4.11**). This is unexpected, but can be explained by considering the

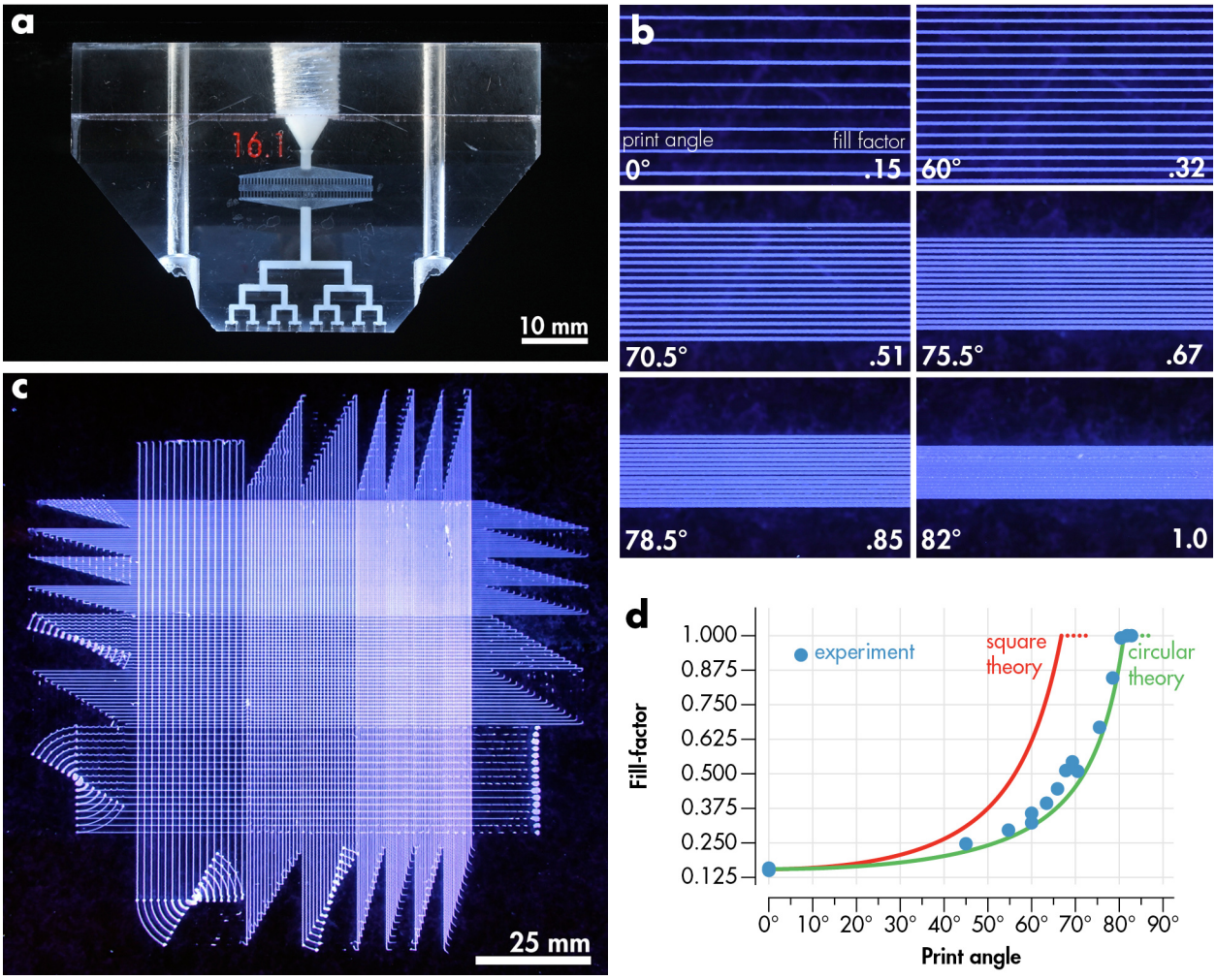

Figure 4.11: Adjustable fill-factor multinozzle (device #16.1). (a) A 16-output, 200 µm nozzle, 1.6 mm center-to-center spacing multinozzle printhead. (b) Examples of wax filaments deposited at various print angles. (c) A two layer structure demonstrating a pattern with varying density. (d) Experimental values of fill-factor vs. print angle are compared to the expected values.

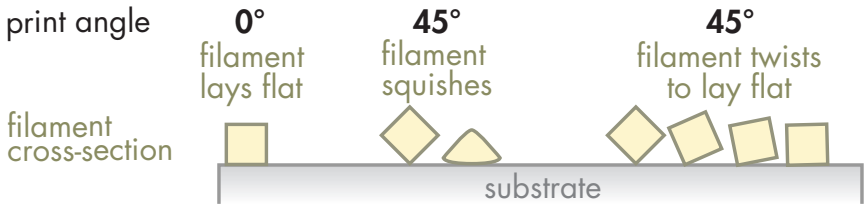

Figure 4.12: Drawing of filament expectation of filament behavior upon deposition. When depostited at a non-zero print angle, the filament might "squish" or twist so it lays flat on the substrate.

case of $\theta = 45°$. While we expect that the cross section to be $\sqrt{2}$ times w_0, this is only the case if the filament lays down on a cross-sectional corner. Since this is an unstable position, the filament may twist such that it lays down on a cross-sectional edge. Thus, at any angle the apparent width, w, is equal and the filaments appear to be circular in cross-section (**Figure: 4.12**).

4.3.4 Wide-spaced multinozzle printheads

The multinozzle printheads were initially designed to fabricate 3D lattice pads, where the members of the lattice are straight, parallel filaments with 0.4 mm center-to-center spacing (§4.2.2). Thus, the original printhead design has exit nozzles that extrude filaments that have a matching center-to-center spacing of 0.4 mm. The adjustable fill factor printhead design increases the center-to-center spacing to 1.6 mm. This design allows a printed stripe to have a fill factor as low as 0.125 (§4.2.4). The wide-spaced multinozzle printhead has a center-to-center spacing of 8 mm. Unlike the original and adjustable fill factor printhead designs, the wide-spaced multinozzle is designed to pattern identical, but separate patterns in parallel similar to multiple individual nozzles affixed together. A square spiral pattern inspired by patterns often used for antennae was employed for a demonstration of the wide-spaced multinozzle printhead. [65, 66] Multinozzle device #21.1 was used to print the square spiral designs using the wax ink. The leftmost nozzle was extruding material more slowly that the other 7 nozzles (**Figure: 4.13**). There may have been a partial clog in the first nozzle or swelling from the solvent welding process that constricted the diameter of the first nozzle. Despite this defect, the difference in extrusion rates between all 8 nozzles was small enough that continuous filaments were printed and 8 rows of spiral structures were patterned with wax on a glass substrate.

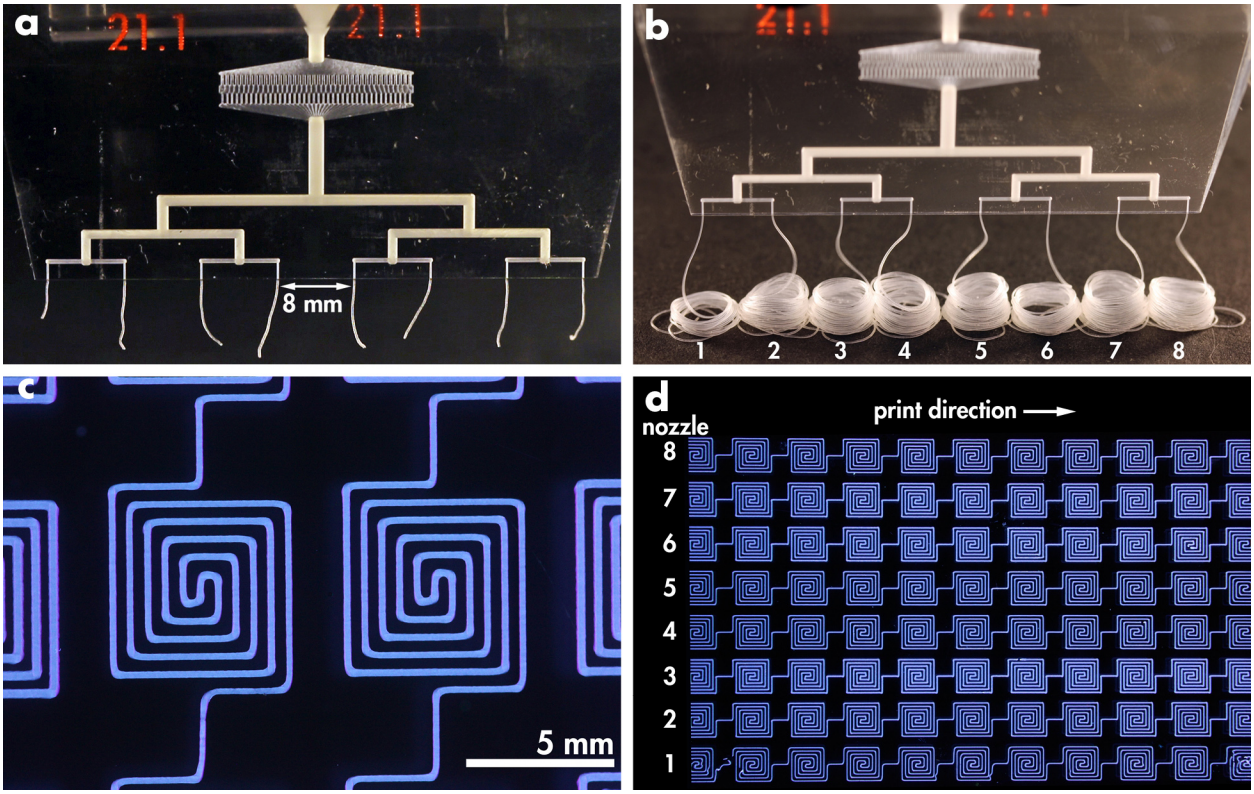

Figure 4.13: Wide-spacced multinozzle printhead (device #21.1). (a) An 8-output, 200 µm filament, 8 mm center-to-center multinozzle printhead. (b) In this device, the left-most nozzle extrudes the wax ink more slowly than the other seven nozzles. (c) This printhead was used to pattern 2D square spiral pattern on glass. (d) Each row of spirals was printed with one of the eight nozzles.

4.3.5 Multinozzle deposition of functional materials

The multinozzle printhead was originally designed for a specific purpose: to print a 3D periodic lattice with a fugitive, organic wax ink. However, the rapid deposition of other functional materials is also important for research and industrial applications. In order to demonstrate the utility of the multinozzle printheads for a wider range of functional materials, we used three additional functional inks: a polymer gel, a ceramic particle ink, and a silver particle ink.

Three-dimensional hydrogel scaffolds have been used to culture neuronal cells.[12] These scaffolds are composed of woodpile architectures with filament widths of 10 µm and filament center-to-center spacing of 40-90 µm. While these small features sizes are unobtainable with current multinozzle printhead designs, we attempted to print similar scaffolds with 200 µm filaments. The pHEMA hydrogel ink printed using multinozzle device #13.2. The ink flowing through the microfluidic network reaches the exit nozzles nearly evenly across the 64 nozzles (**Figure: 4.14**). Thus, during printing 64 filaments were also extruded evenly. We

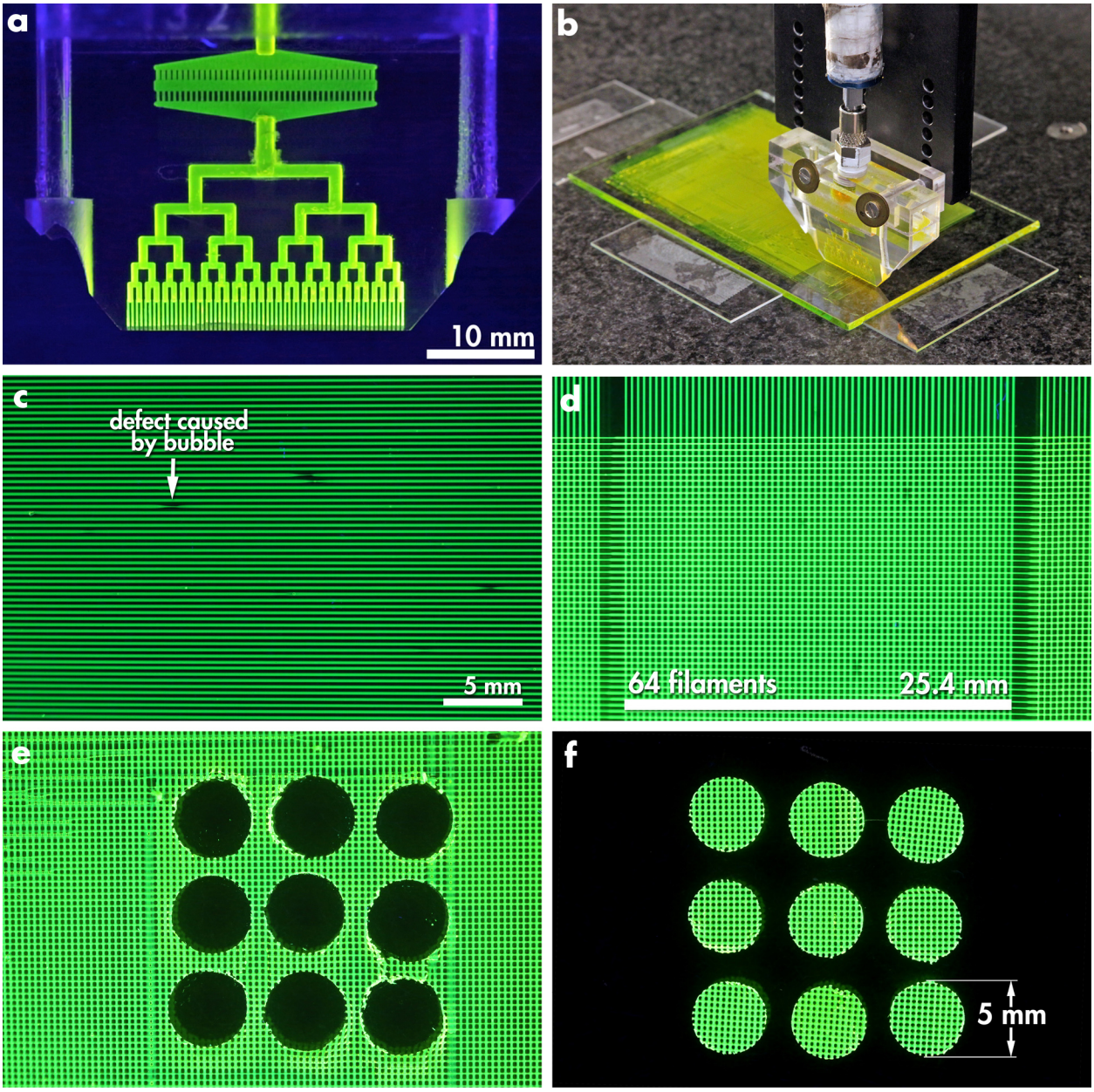

Figure 4.14: Printing pHEMA hydrogel ink (device #13.2). (a) A 64-output, 200 ?m filament, 0.4 mm center-to-center spacing multinozzle printhead. (b) The printhead mounted on a 3D positioning gantry. (c) One layer of filaments. Defects caused by bubbles in the ink are visible. (d) Two layers of pHEMA filaments. (e,f) 5 mm circles punched out with a biopsy punch.

attempted to print two- and four-layer woodpile structures with this ink. While the nozzles extruded evenly, the printed filaments did not span gaps as intended. Thus, instead of a woodpile structure, a flat, square grid was produced. The pHEMA ink is a yield-stress fluid than can be solidified with exposure to UV light. In our experiment, we printed the entire structure, then cured the structure with a large UV lamp. A UV LED placed on the trailing

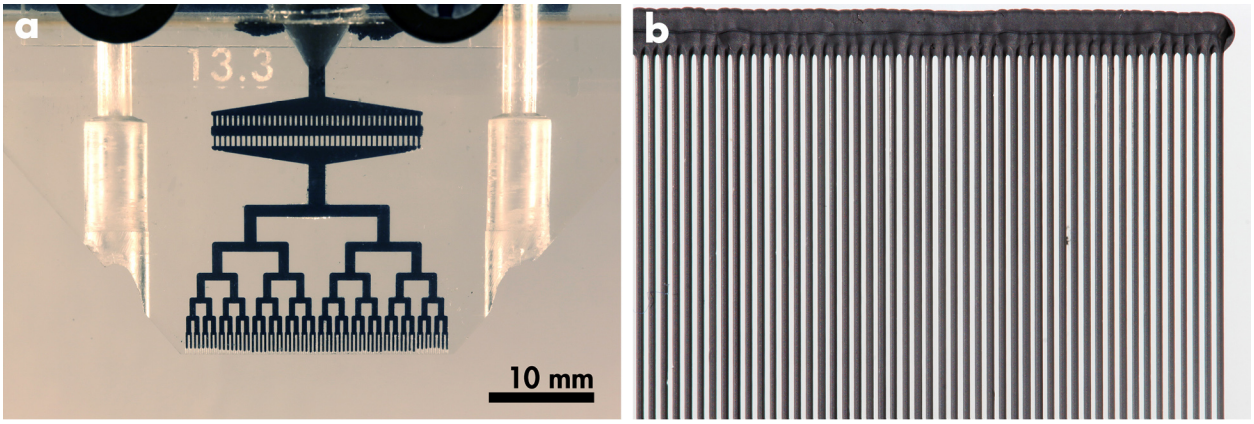

Figure 4.15: Printing copper oxide particle ink (device #13.3). (a) 64-output, 200 µm filament, 0.4 mm center-to-center spacing multinozzle device. (b) 200 µm wide copper oxide filaments.

edge of the multinozzle printhead, the filaments could be cured immediately upon deposition, and so they solidify before they can sag significantly. A UV-opaque coating would prevent the light from curing the ink and causing a clog within the printhead. Occasionally, bubbles (100 µm) were found in deposited filaments. These bubbles were likely not formed by the printing process, but originated as larger bubbles in the ink reservoir.

The copper oxide ink was patterned with a 64-output, 200 µm nozzle, 0.4 mm center-to-center spacing multinozzle printhead (device #13.3). The filaments were deposited in single stripes with few defects. The deposited filaments were sintered in oxygen-free environment in order to convert the copper oxide into elemental copper. While the chemical transformation occurred as expected, during the annealing filaments debonded from the glass substrate and did not retain the as-deposited pattern (**Figure: 4.15**).

The silver particle ink was patterned with an 8-output, 200 µm nozzle, 8 mm center-to-center spacing multinozzle printhead (device #21.2). The ink printed relatively evenly through all 8 outputs. The ink was patterned using the same spiral antenna design employed by device #21.2 (§4.2.5). Compared to the spirals patterned in wax, the spirals pattern with the silver ink tended to have undesired "smudges" around the corners. We believe these defects appear because the silver ink is so thin (much thinner than the wax ink), the ink tends pool at corners. The wax ink behaves more solid-like after deposition and does not exhibit this effect (**Figure: 4.16**).

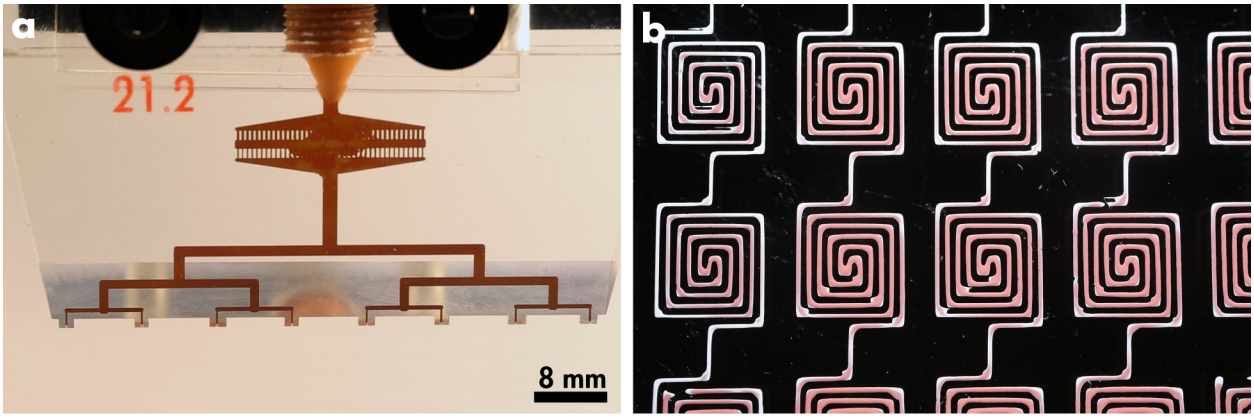

Figure 4.16: Printing silver nanoparticle ink (device #21.2). (a) 8-output, 200 µm filament, 8 mm center-to-center spacing multinozzle device. (b) Square spiral patterns printed with silver ink. The ink is reddish-brown and turns light gray upon drying.

4.4 Conclusion

The Murray's Law multinozzle printhead design resulted in the printing time of the 0.38 m^2 pad being reduced by a factor of 8, relative to a single nozzle deposition. The Wide Channel design allowed for the printing time to be reduced by a factor of 64 times, relative to a single nozzle deposition. The co-infiltration process was unsuccessful in producing woodpile lattices of sufficient quality and was not pursued further. One and two layer structures composed of stripes of user-controlled density were successfully deposited by varying the print angle of a specially designed multinozzle printhead. A multinozzle printhead was adapted to print 8 parallel features of arbitrary design. Finally, three functional inks were successfully deposited using multinozzle printheads.

Chapter 5

Conclusions

This thesis describes the design, fabrication, analysis, and implementation of multinozzle printhead devices. The microfluidic channel designs are inspired by natural architectures, and include variations that optimize for relevant features. The principle findings of this research are summarized below:

1. Printhead design and modeling

   (a) The Hagen-Poiseuille equation is used in series and in parallel to accurately predict the behavior of Newtonian fluids in bifurcating microfluidic channel networks.

   (b) An iterative 1D model is developed to predict fluid flow of power-law fluids in channels. This iterative model matches exactly with a previously developed direct 1D model.

   (c) The iterative 1D model predicts trends in volumetric flow rates for networks with geometric asymmetries. These results were confirmed with 3D fluid simulations.

   (d) The 1D model predicts that widening the upper generations of the microfluidic network dramatically reduces the overall hydraulic resistance, but also makes the device more susceptible to non-uniform fluid flows due to geometric defects or asymmetries.

2. Printhead implementation

   (a) Printheads with bifurcating microfluidic networks are used to successfully fabricate large area woodpile structures for use as polishing pads.

   (b) Printheads that have nozzles with wide center-to-center spacing are used to pattern features of variable density depending on the printhead's orientation.

   (c) Printheads with very wide center-to-center spacing are used to simultaneously deposit multiple filaments in an arbitrary 2D pattern.

   (d) Functional materials, including hydrogel and colloidal inks, are successfully patterned using multinozzle printheads.

5.1 Future work

Future work can explore methods of further improving the multinozzle printheads. For example, they could be manufactured out of more robust materials. While PMMA is easily machined and can be easily bonded to itself, it has limitations. Since the glass transition temperature of PMMA is roughly 120°C[67], a PMMA device would not be suitable for extruding molten polymers (e.g. ABS and PLA), which are commonly heated to temperatures above 200°C.[68] Possibly a better material choice would be a metal. Many metals, such as aluminum and brass, are easily machined and withstand temperatures well above 200°C. While the metal components cannot be solvent bonded like PMMA, two mating faces and be lappend and polished extremely flat, such that they wring together. The two faces could be mated and the tapered end of the device could be forced into a collet that clamps and seals the device evenly.

The printheads could also be adapted into active devices. If each nozzle had an individually addressable valve, the printhead could deposit complex, dynamic patterns. While this could be implemented with a Plenum-type design with one valve for each nozzle, it could also be implemented with a bifurcating array design with valves in each channel in each generation.The benefit would be that entire sections can be controlled with a single valve. Since small valves could be fragile, a reduction in flow from a larger upstream valve would reduce the pressure experienced at a smaller nozzle valve. This system would require an algorithm that compensates for the change in overall hydraulic resistance by modulating the input applied pressure. This type of active printhead could be manufactured out of rigid silicon using well-established MEMS technology.[69]. An advanced active printhead could also have an image-based feedback system, which would analyze the just-deposited filaments and could correct for clogs or unexpected changes in filament diameter.

Ultimately, we hope that this work will advance the feasibility of inexpensive, large-scale products manufactured by 3D extrusion printing.

Appendix A

Hydraulic diameter and square channels

The Hagen-Poiseuille equation and other equations relating properties like shear rate and viscosity were developed for pipes with circular cross section. In order to predict fluid flow in channels of non-circular cross section, diameter term can be replaced by the *hydraulic* diameter, defined as:

$$d_{\text{hyd}} = \frac{4 \times \text{cross sectional area}}{\text{wetted perimeter}} \tag{A.1}$$

In the case of a circular channel, the hydraulic diameter is equal to the inner diameter of the pipe. In the case of a square channel, the hydraulic diameter is equal to the width and depth of the channel. However, a square channel with an identical length and hydraulic diameter to a circular channel will have a lower hydraulic resistance for a given applied pressure.

If This is because the square has a greater area than the circle (at the same hydraulic diameter). In the case of a Newtonian fluid, $R_{\text{square}}/R_{\text{circle}} = 0.697$. For power-law fluids, this ratio is dependent upon n.[49]

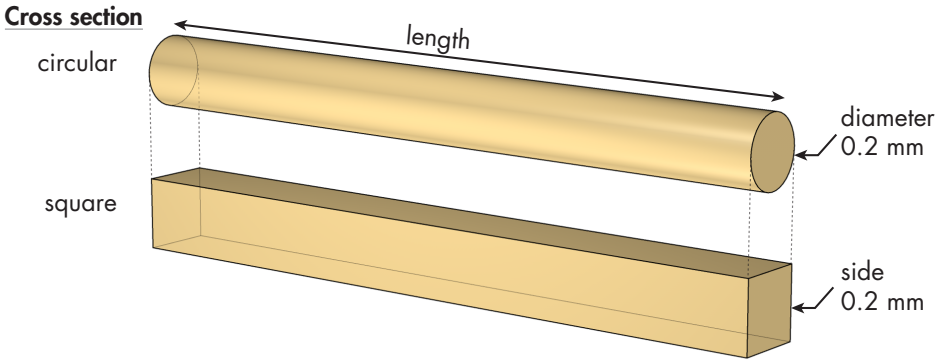

Figure A.1: Channels with circular and square cross sections.

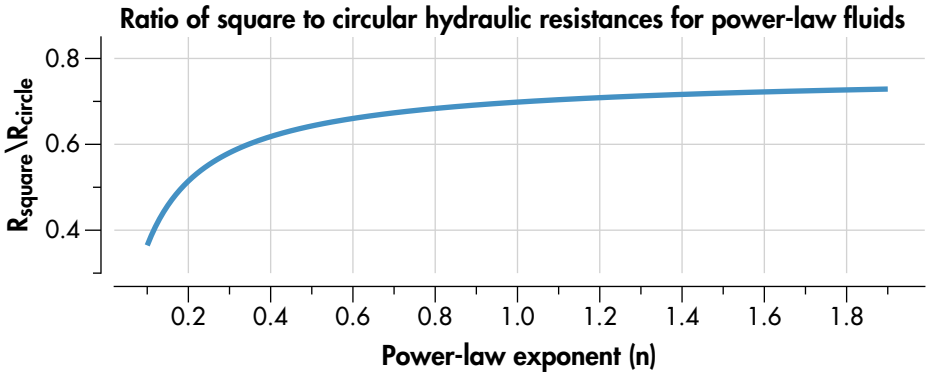

Figure A.2: Square channels have a lower hydraulic resistance than circular channels of the same hydraulic diameter. This ratio is dependent on *n*, the power-law exponent. [49]

For shear-thinning fluids ($n < 1$), the ratio of square to circular channel hydraulic resistances decreases sharply. For shear-thickening fluids ($n > 1$), the ratio slowly increases above the Newtonian ($n = 1$) value. For the organic wax ink ($n = 0.44$), this ratio is 0.629.

Appendix B

3D simulations of laminar flow at high Reynolds number

When designing the microfluidic networks, we were concerned about effects that could lead to uneven output flow. At steady state, fluid in a straight channel will have a maximum flow velocity in the channel center and decrease towards the channel walls. This is ideal for the case of a bifurcation where equal flow through both daughter channels is desired. However, as fluid flows through a channel bend or elbow, the maximum flow velocity moves toward the outer wall.[70] Thus, immediately after the bend, the flow velocity is asymmetric and a downstream bifurcation can see uneven flow through the two daughter channels. After the bend, the asymmetric radial flow distribution tends to symmetry. The length of channel required to achieve an axi-symmetric flow rate distribution (within 99%) is defined as the "hydrodynamic entrance length."[71] There are many models for calculating the entrance length for a channel, but in the case of low Reynolds number fluids, the entrance length is simply $L_{\text{entrance}} = 0.6 d_{\text{hyd}}$.[38] To confirm the results from literature, we used 3D fluid simulations to model a square cross-section channel with a square elbow followed by a T-junction bifurcation. (**B.1**) We found that at a Reynolds number of 10, the volumetric flow rate through the left and right daughter channels was virtually even. At a higher Reynolds number of 200, more flow is directed to the left daughter channel which corresponds to the outer wall of the elbow. At higher Reynolds number, the flow is no longer laminar, and the unevenness in daughter flow rates is expected to increase. As an example of how this could affect a network with multiple generations of bifurcations, we modeled a 3-generation, 8-output network, with channels widths and depths conforming to Murray's law. (**B.2**) The nature of the uneven flow in the bifurcations results in higher flow rates in channels that correspond to the outer-side of the elbows. When fabricating our microfluidic channel networks, we designed the channel lengths after an elbow to be no shorter than 1.5 times the width and depth of the channel.

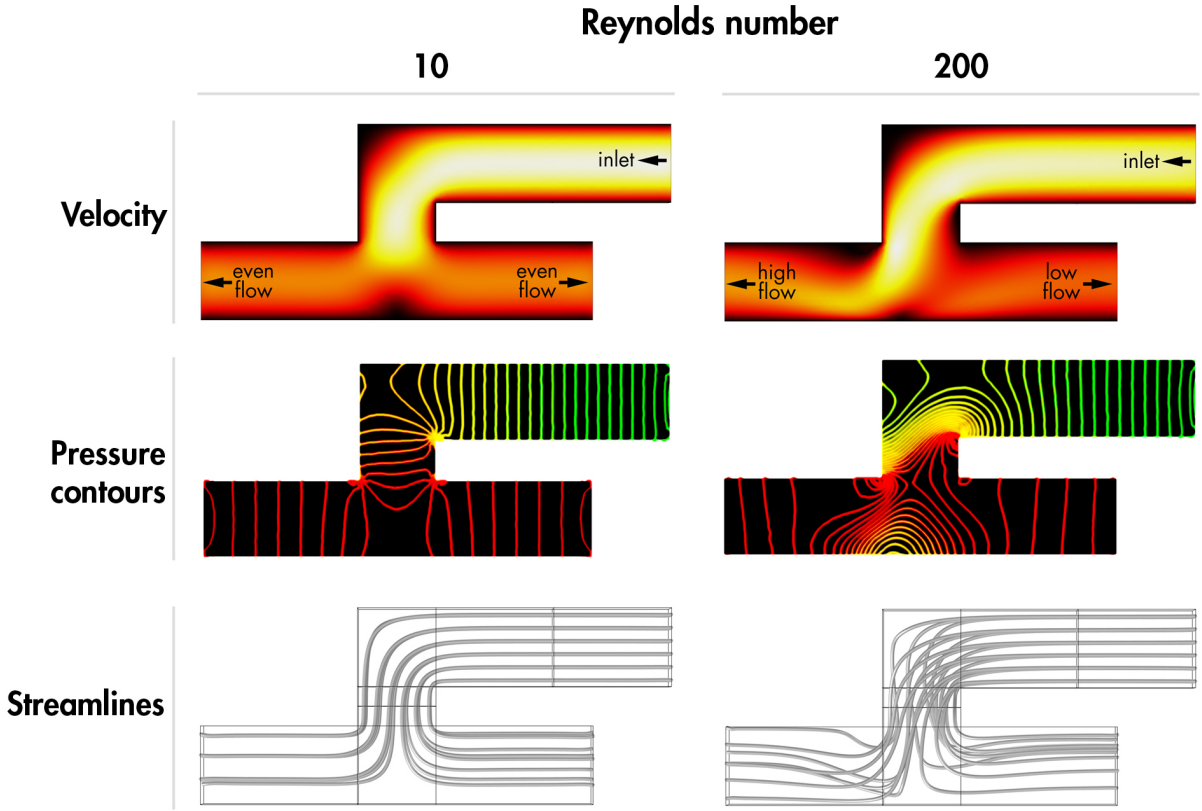

Figure B.1: A 3D laminar fluid simulation performed in COMSOL at Reynolds numbers 10 and 200. For the velocity figures white is fast flow and black is zero flow. The pressure contours are green at high pressure and red at zero. The streamlines represent the trajectory of tracer particles in the flow.

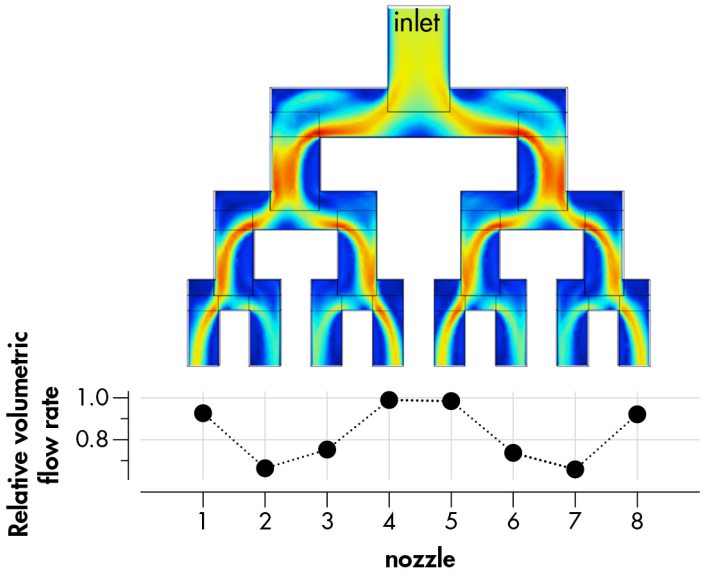

Figure B.2: A 3D laminar fluid simulation performed in COMSOL for a 3-generation bifurcating network at a Reynolds number of roughly 100. Red is high flow velocity and blue is low velocity.

Appendix C

Multinozzle printhead evolution

The multinozzle printhead was first designed and successfully built by Chris Hansen.[59, 1] While successful printheads were made, creating them was time consuming and they had a high failure rate. Our goal was to fabricate these printheads more quickly with at a higher success rate.

The first change we made was to machine all of the channel and blank blocks to the same dimensions (70 mm $\times$ 35 $\times$ mm $\times$ 8 mm). These blocks were machined on a 3-axis CNC vertical mill such that the block is nearly fully formed, but held in place with four tabs. This operation defines an origin that is used to locate the microfluidic channels.

Initially, a large (9 mm) hole was machined into the mated channel and blank blocks which connected the input to the beginning of the fluidic network. This created a sudden and large pressure drop as the channel diameter reduced from 9 mm to 0.8 mm. To alieviate this pressure drop, a "conical reduction" was made with a chamfer endmill. This made the pressure drop more gradual. When the large input hole was machined and tapped directly into the mated block assembly, the part would sometimes split apart. Instead, we created a third piece, the "top cap" that simply contained the tapped input hole.

The printheads also contain two cylindrical through holes on the left and right side of the microfluidic network. The holes allow the printhead to be mounted to a stage with screws. These holes were initially created with a drill press after the rest of the device was completed. However, while drilling these holes, sometimes debonding would occur. Instead, while machining the channel and blank blocks, we used a 1/8" ball nose end mill to cut corresponding semicircular slots. These slots become half of the screw hole and do not promote debonding.

After the three pieces of the printhead are bonded together, the device is a rectangular prism. In this state, when ink is extruded it can easily stick to the outside of the printhead. To reduce this effect, the bottom of the device was machined away (roughly 1 mm deep) except for an area immediately surrounding the exit nozzles. While this is a simple procedure, it obstructs a complete view of the microfluidic network. To the same end, the front and back of the printhead are machined at an angle so the device is tapered. This keeps the

entire network visible and prevents ink from sticking to the device. These changes were made in multinozzle printheads designated as Series 1, 2, and 3.

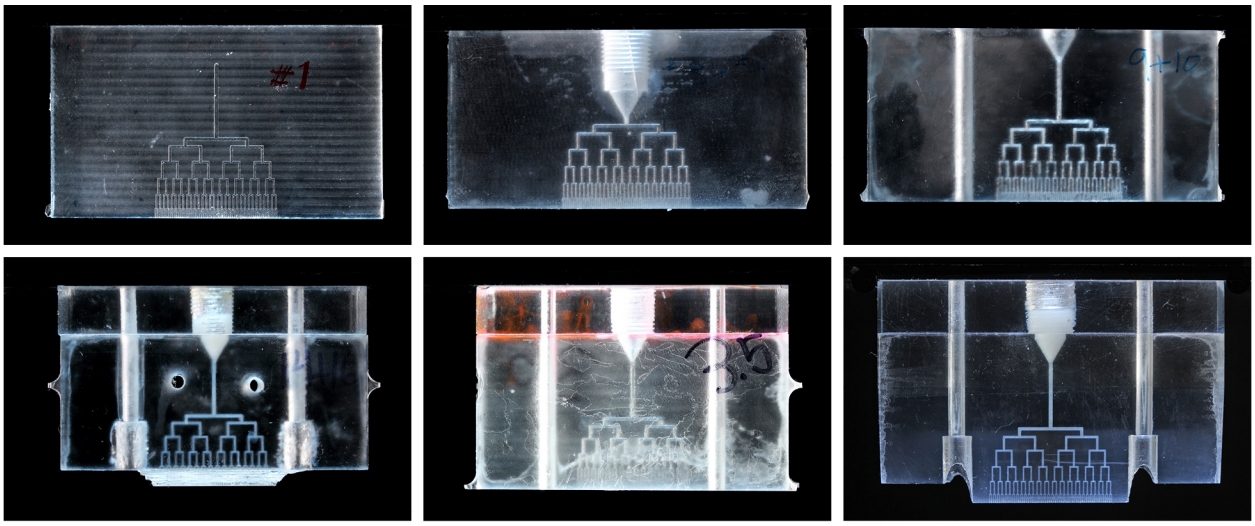

Figure C.1: Series 1, 2, and 3. The first improvement to the printhead devices was a "conical reduction" that funneled ink from the input into the network. The "top cap" was added to reduced the tendency of the block assembly to debond during the tapping process. The device was machined to a taper so the entire network could be seen clearly while preventing the build up of extruded ink.

In Series 4, the next major change in printhead design involves the tool paths for machining the microfludic network. In earlier devices, the channels were machined first by a rough cut that cut out the right side of a given channel. In cases where the channel was wider than the endmill diameter, the endmill would step over a distance 50% of the endmill diameter until the designated width was machined. Instead, an endmill with a diamter 50% to 90% of the channel diameter machines a rough cut through the center of the channel. The left and right sides of the channel are then machined with finishing climb cuts. Series 4 also includes a taper in the left and right sides as well as the front and back. This extra taper is done mostly for aesthetic purposes. Device #4.1 was the first multinozzle to print a satisfactory 12" $\times$ 12" 4-layer pad.

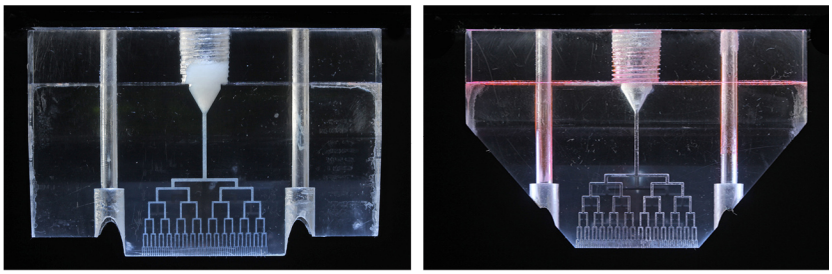

Figure C.2: Series 4. This series produced the first acceptable 12 inch woodpile lattice pad. The multinozzle was also tapered from the sides as well as the front and back.

Series 5 is made the same way as Series 4, with the addition of a prefilter between the ink input and the microfluidic network. Beginning with Series 6, part numbers are laser engraved into the channel block prior to solvent welding. This yields a more permanent and visible identification to each devices. Before, part numbers were written on the devices with marker, which was easily washed away. Series 7 is made with the same as earlier devices. One channel network was sacrificed for use as an SEM specimen.

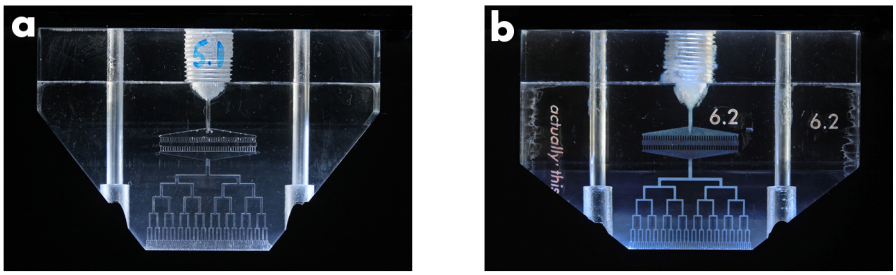

Figure C.3: Series 5 and 6. Series 5 (a) included a prefilter to prevent debris from clogging the device. Series 6 (b) began the trend of laser engraving part numbers on the channel blocks of the multinozzles.

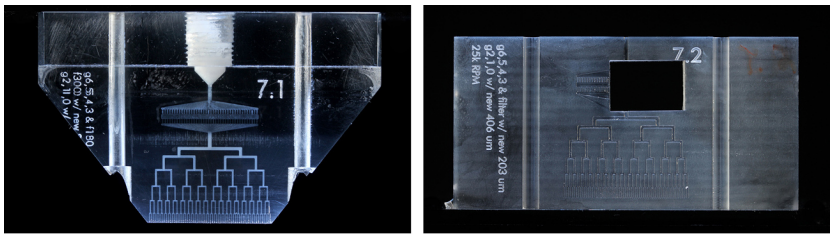

Figure C.4: Series 7. Device #7.1 is similar to series 6. Channel block #7.2 was used as an SEM specimen.

Series 8 devices are made in the same way Series 5, 6, and 7. At this point in the multinozzle evolution the Series numbers are designating different "batches" as opposed to significant changes in design. That is, the all the devices in a given series were made simultaneously. Device #8.3 printed the first acceptable 24" × 24" 4-layer pad.

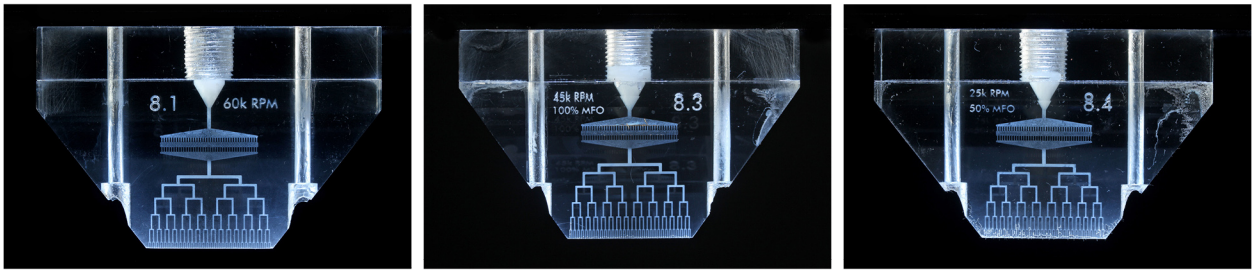

Figure C.5: Series 8. This series is similar to Series 6 and 7.

Series 9 printheads have two parallel, but offset microfluidic networks. The two channel blocks are separated by a thin (1 mm) piece of acrylic. The input in the top supplies the wax ink and the input on the front or back supplies the epoxy. Series 9 also included two single-deposition printheads similar to Series 5, 6, 7, and. 8. Device #9.6 printed a 24" pad with fewer defects than the pad printed with #8.3. Series 10 are the same design as the dual-deposition printheads of Series 9.

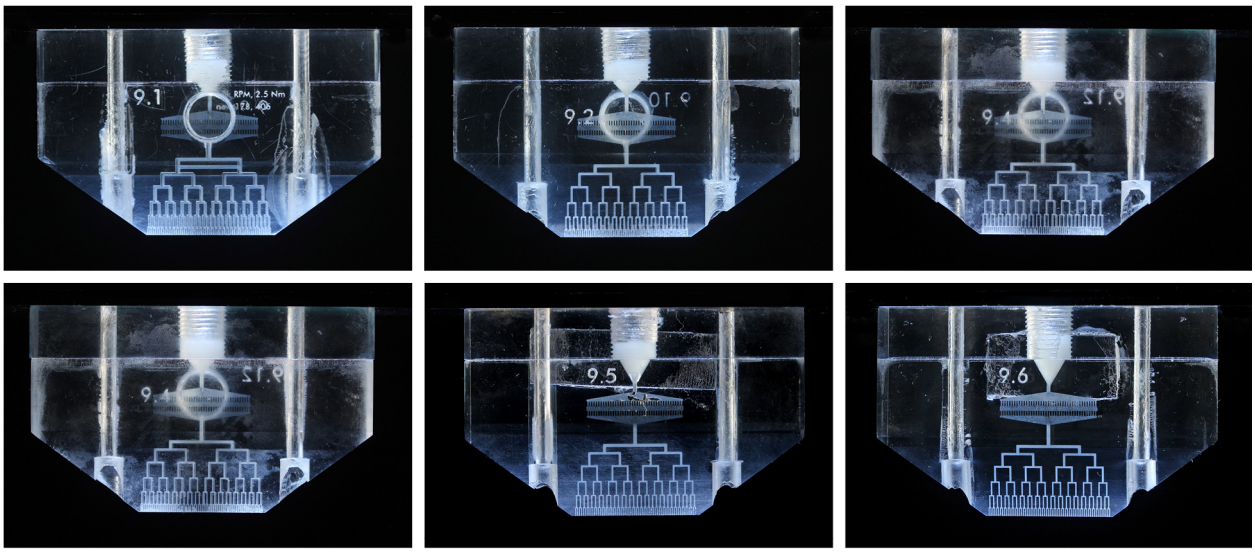

Figure C.6: Series 9. Series 9 devices were the first dual-deposition printheads designed for wax and epoxy. This series included two "traditional" single-deposition printheads.

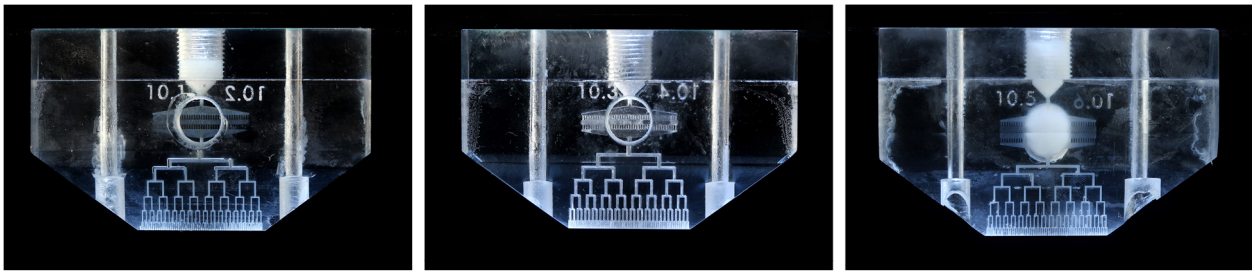

Figure C.7: Series 10. This series is a repeat of the dual-deposition devices in series 9.

The channel blocks in Series 11 were not made into function devices, but were sputter coated and used as SEM samples. Series 12 is a single device made in the same design as Series 8 and others.

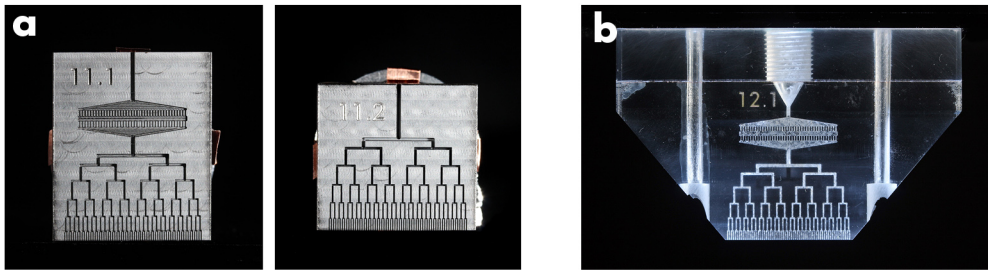

Figure C.8: Series 11 and 12. Series 11 (a) channel blocks were used for SEM specimen. Series 12 (b) was similar to series 6, 7, and 8.

Series 13 is a single-deposition printhead with a "Wide" network design. Channel generations 0 through 5 (generation 6 are the nozzle channels) have widths and depths equal to twice that of the Murray's law network design. A dramatic reduction in hydraulic conductivity was observed with these printheads. Device #13.1 was used to print a nearly defect-free 24" pad. This series was used for several of the functional material printing experiments in Chapter 4.

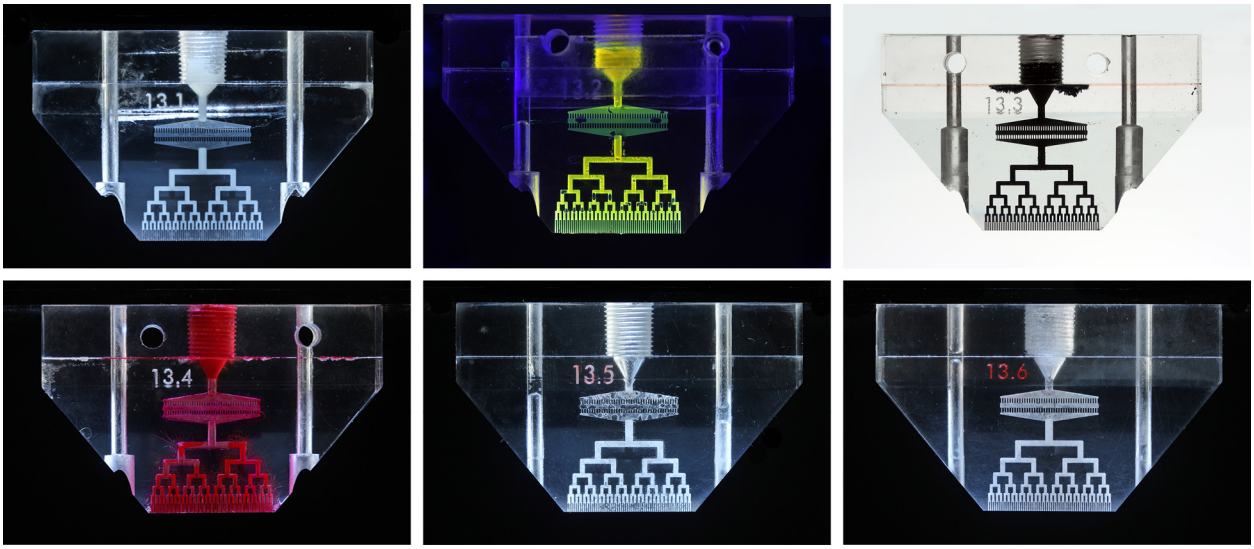

Figure C.9: Series 13. This series debuted the "Wide" channel design. All previous multinozzle printheads had channel diameters conforming to Murray's law. The upper generations of Series 13 printheads have diameters twice that of previous devices.

Series 14 printheads have a microfluidic network similar to Series 13, except it has 7 generations, 128 outputs, with 100 µm × 100 µm nozzle cross section. The center-to-center nozzle spacing is 200 µm. This series was an exploration into the minimum reliable feature size of our printhead manufacturing methods. While printhead #14.1 produced acceptable results, it was difficult to use in practice because it had to be aligned very precisely relative to the substrate.

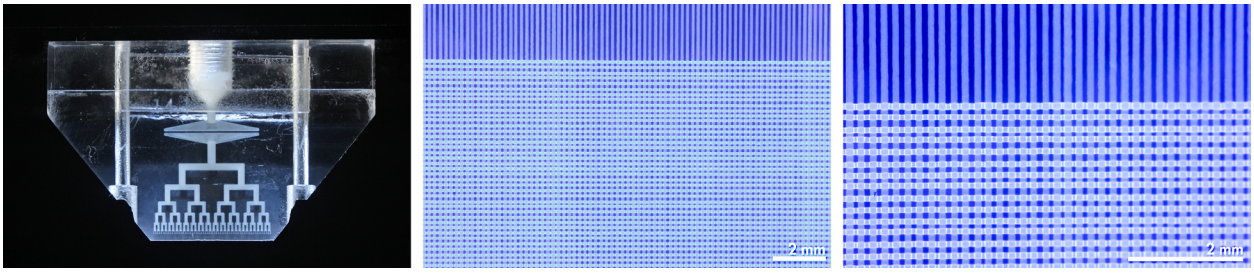

Figure C.10: Series 14. This series has a seven-generation, 128-output bifurcating network with nozzle dimensions of 100 µm.

Series 15 printheads have a "Ultra-wide" network design. Instead of a channel bifurcating at a T-junction, there is a "divider wall" that progressively separates the single channel into 64 channels. The total width of each generation are all roughly 25 mm. While this design works in theory, in practice there are complications. Of the four devices made, none of them printed 64 filaments evenly. In some channels, the fluid unexpectedly flowed in the reverse direction. The causes of the irregularities were likely due to the high aspect ratio of the channels. In other network designs he channels have a square cross section, while Series 15 had rectangular cross section with aspect ratios as high as 8. Fluid flow in high-aspect ratio channels can be complicated and does not follow the Hagen-Poiseuille equation. Additionally, in other designs fluid exiting the prefilter is funneled into a narrow channel. In Series 15 the filter feeds directly into the wide 0th generation channel. In effect, a narrow ribbon of fluid was being extruded (sometimes unevenly) into a much deeper plenum.

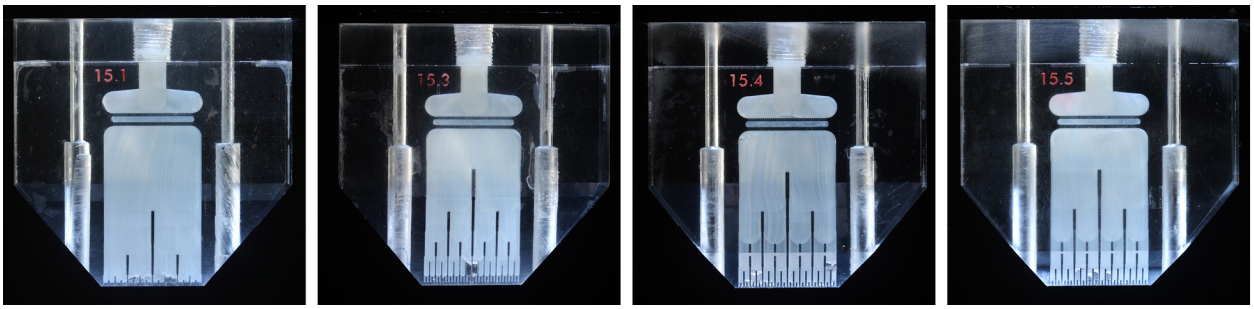

Figure C.11: Series 15. This series was dubbed "Ultra-wide" network.

Series 16 printheads are the devices used for density gradient printing described in Chapter 4. They have a 4-generation, 16-output network, with 200 µm × 200 µm cross-section nozzles. The center-to-center nozzle spacing is 1.6 mm.

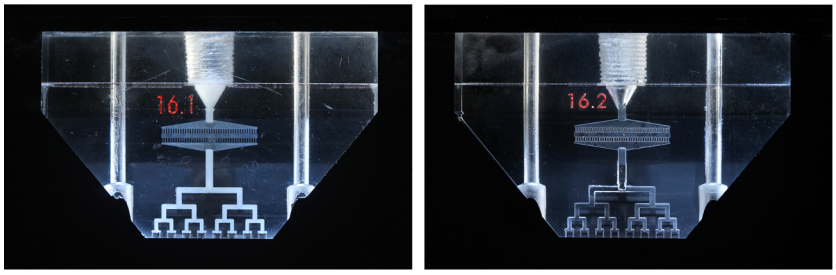

Figure C.12: Series 16. This series has a 4-generation, 16-output network with 1.6 mm nozzle center-to-center spacing. These printheads were used for the density gradient printing.

Series 17 printheads have the same Wide network design as Series 13. These devices are used to experimentally measure the volumetric flow rates per applied pressure for glycerol and organic wax inks. The devices do not have prefilters, which would significantly reduce the measured flow rate. Series 18 have a Murray's law network but do not have prefilters. They are used the same way as Series 17 devices.

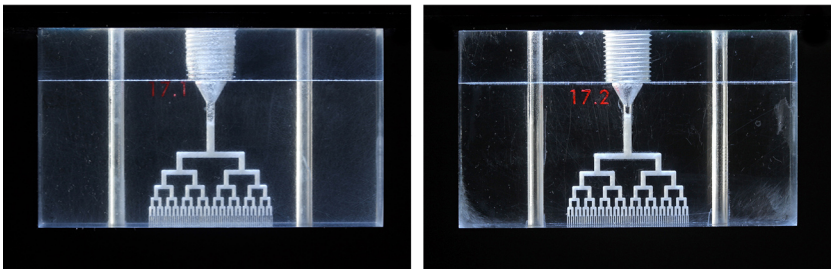

Figure C.13: Series 17. This series has a "Wide" channel network like series 13, but does not include a filter. These printheads were used for the experimental measurements in Chapter 3. These devices were later machined to have a taper like other printheads.

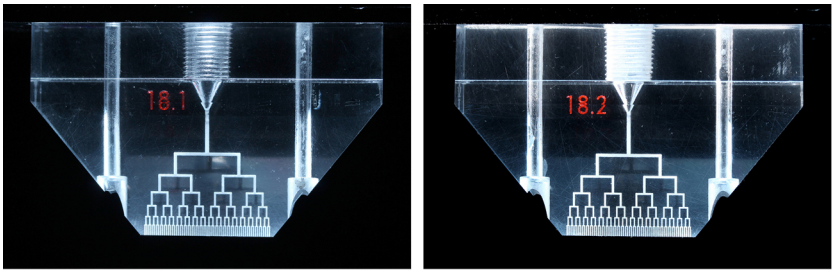

Figure C.14: Series 18. This series has a "Murray's" channel network like series 12 and earlier, but does not include a filter. These were used for the experimental measurements in Chapter 3.

Microfluidic devices built out of glass capillaries or PDMS are often used to create oil/water emulsions. In Series 19, we adapted our multinozzle printheads to create oil in water emulsion at high throughput. These devices are composed of two parallel 16-output bifurcating networks. The outputs of each network are connected by 16 parallel channels 500 µm wide and deep. The flow rates of the oil and water are controlled such that droplets of oil break off at the T-junction where the oil and water stream meet. While this device worked relatively well, there are more efficient methods of creating emulsions. A major benefit of these acrylic devices is the high pressure and high flow rates they can withstand. However, due to the physics of droplet formation, very high flow rates yield continuous jets instead of discrete droplets. Thus the devices cannot take advantage of their inherent strength. These experiments were performed with the help of James Hardin and Jaime Juarez.

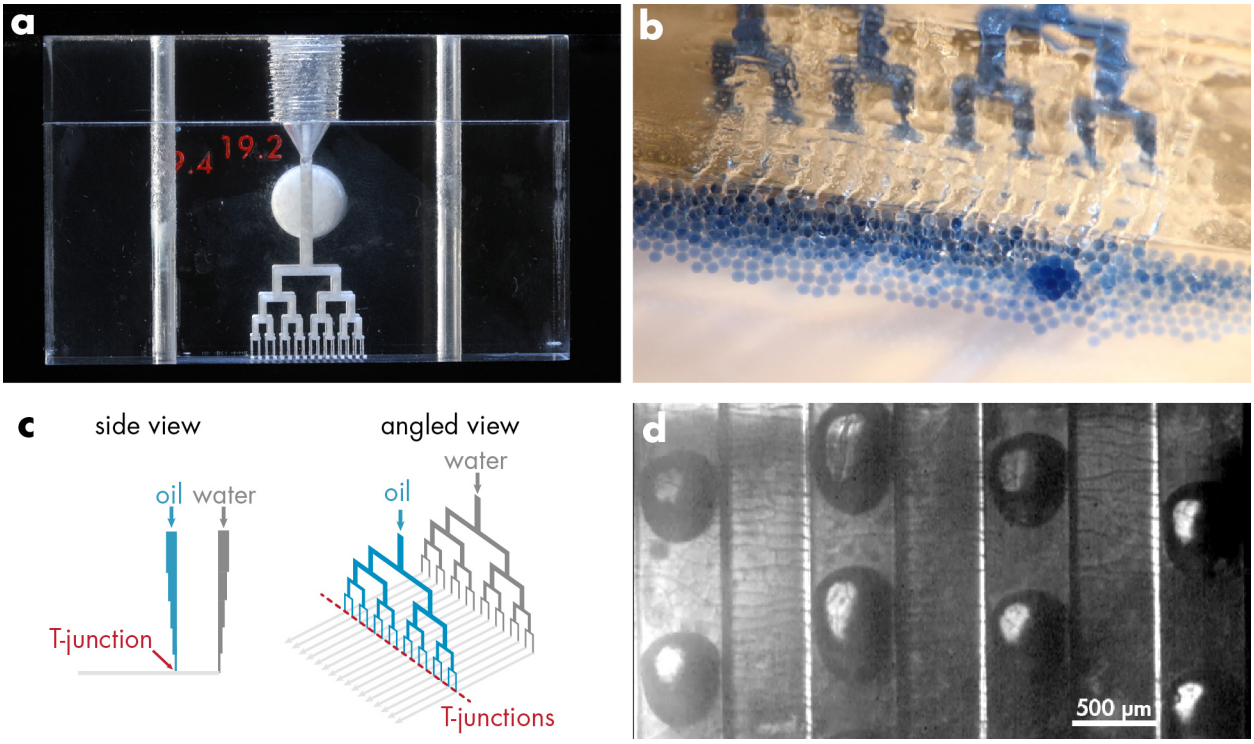

Figure C.15: Series 19. (a) Unlike other multinozzle devices, this series was designed to create oil in water emulsions. (b) Optical image of emulsion drop production. (c) Schematic of the device. (d) High-speed video frame of the emulsions immediately downstream of the T-junctions.

Series 20 has an "Extra-wide" network design. The nozzle dimensions (6th generation) are the same as the Murray's Law and Wide networks, while the 5th generation is twice the width/depth of the Murray's law network, and the 4th through 0th generations are four times the width/depth of Murray's law network. This series does not have a prefilter and is used for experimental measurements in Chapter 3.

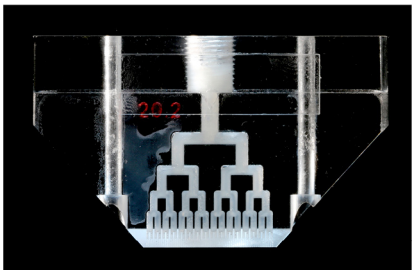

Figure C.16: Series 20. These printheads have a "Extra-wide" network without a filter and were used for the experimental measurements in Chapter 3.

Series 21 printheads have 8-output, 200 µm × 200 µm nozzle cross section, with 8 mm nozzle center-to-center spacing. Like other printhead designs, this series is tapered at the outputs. Additionally, a roughly 1 mm × 1 mm square pillar is machined around each nozzle. The removal of acrylic between the nozzles prevents smudging of the ink when the printhead is translated laterally.

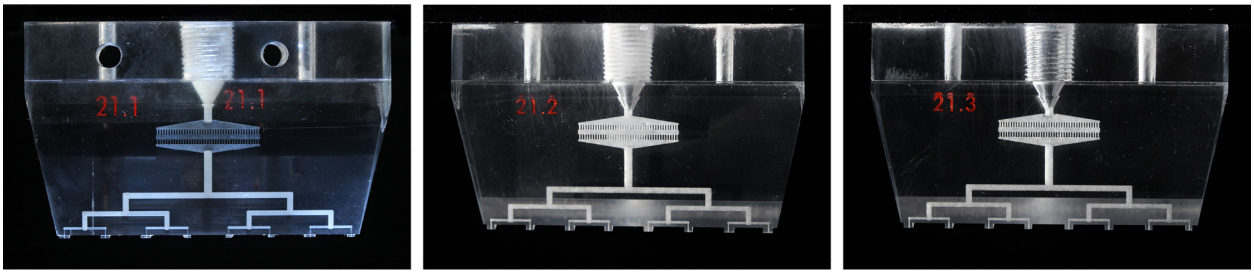

Figure C.17: Series 21. These printheads have 8 outputs with 8 mm nozzle center-to-center spacing. They were used to create the square spiral patterns in wax and silver inks in Chapter 4.

Series 22 printheads have a "Plenum" design. After a prefilter, the ink is distributed via 2-generation network, which feeds into an open chamber, or plenum. The plenum connects all 64 outputs and effectively equalizes the pressure above the nozzles. Plenum design devices were made with nozzles 2 mm long and 0.5 mm long. Device # 22.4 successfully printed filaments at 150 mm/s at roughly 850 psi of applied pressure.

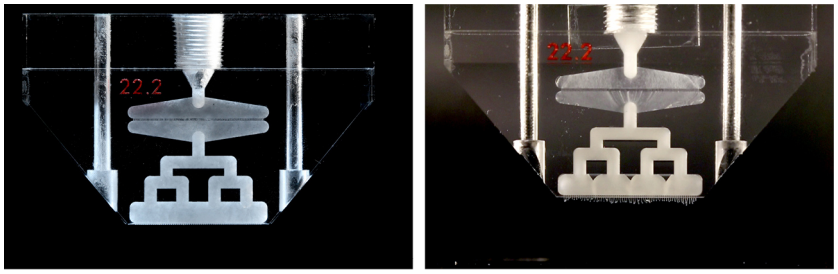

Figure C.18: Series 22. These printheads have a "Plenum" network design. The pictured printhead has nozzles with lengths of 500 µm.

For this work, a total of roughly 60 multinozzle printheads were fabricated. The devices in Series 13 through 21 were fabricated with the help of Artie Jataputra.

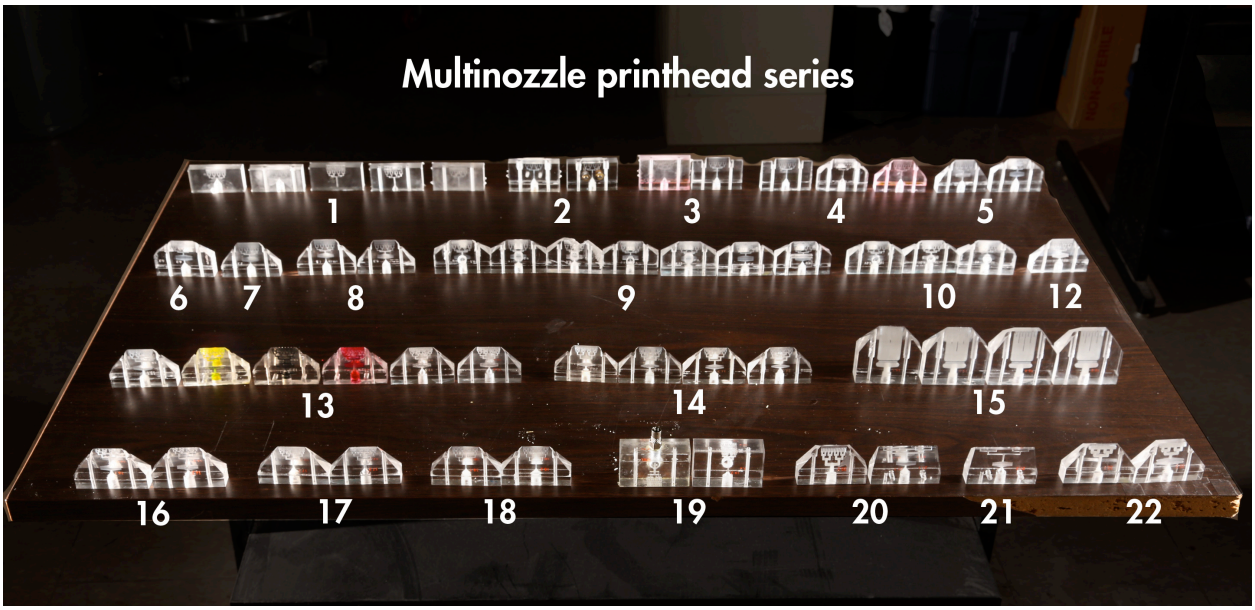

Figure C.19: Photograph of nearly all of the multinozzle printheads fabricated for this work.

References

[1] C. J. Hansen, R. Saksena, D. B. Kolesky, J. J. Vericella, S. J. Kranz, G. P. Muldowney, K. T. Christensen, and J. A. Lewis, "High-throughput printing via microvascular multinozzle arrays," *Advanced Materials*, vol. 25, no. 1, pp. 96–102, 2013.

[2] I. Gibson, D. W. Rosen, and B. Stucker, *Additive manufacturing technologies: Rapid prototyping to direct digital manufacturing*. Springerverlag Us, 2010.

[3] J.-P. Kruth, M. Leu, and T. Nakagawa, "Progress in additive manufacturing and rapid prototyping," *CIRP Annals-Manufacturing Technology*, vol. 47, no. 2, pp. 525–540, 1998.

[4] E. Sachs, "Three dimensional printing," tech. rep., DTIC Document, 2001.

[5] J. A. Lewis, "Direct ink writing of 3D functional materials," *Advanced Functional Materials*, vol. 16, no. 17, pp. 2193–2204, 2006.

[6] S.-H. Ahn, M. Montero, D. Odell, S. Roundy, and P. K. Wright, "Anisotropic material properties of fused deposition modeling ABS," *Rapid Prototyping Journal*, vol. 8, no. 4, pp. 248–257, 2002.

[7] J. Gonzalez-Gomez, A. Valero-Gomez, A. Prieto-Moreno, and M. Abderrahim, *A new open source 3D-printable mobile robotic platform for education*, pp. 49–62. Springer, 2012.

[8] www.makerbot.com, "Replicator 3D printer," 2013.

[9] J. Cesarano III, "A review of robocasting technology," in *Symposium on Solid Freeform and Additive Fabrication*, vol. 542, pp. 133–139, Cambridge Univ Press.

[10] J. A. Lewis, J. E. Smay, J. Stuecker, and J. Cesarano, "Direct ink writing of three-dimensional ceramic structures," *Journal of the American Ceramic Society*, vol. 89, no. 12, pp. 3599–3609, 2006.

[11] B. Y. Ahn, D. J. Lorang, and J. A. Lewis, "Transparent conductive grids via direct writing of silver nanoparticle inks," *Nanoscale*, vol. 3, no. 7, pp. 2700–2702, 2011.

[12] J. N. Hanson Shepherd, S. T. Parker, R. F. Shepherd, M. U. Gillette, J. A. Lewis, and R. G. Nuzzo, "3D microperiodic hydrogel scaffolds for robust neuronal cultures," *Advanced Functional Materials*, vol. 21, no. 1, pp. 47–54, 2011.

[13] L. Sun, S. T. Parker, D. Syoji, X. Wang, J. A. Lewis, and D. L. Kaplan, "Direct-write assembly of 3D silk/hydroxyapatite scaffolds for bone co-cultures," *Advanced Healthcare Materials*, vol. 1, no. 6, pp. 729–735, 2012.

[14] E. B. Duoss, M. Twardowski, and J. A. Lewis, "Sol-gel inks for direct-write assembly of functional oxides," *Advanced Materials*, vol. 19, no. 21, pp. 3485–3489, 2007.

[15] F. Doreau, C. Chaput, and T. Chartier, "Stereolithography for manufacturing ceramic parts," *Advanced Engineering Materials*, vol. 2, no. 8, pp. 493–496, 2000.

[16] C. Sun, N. Fang, D. Wu, and X. Zhang, "Projection micro-stereolithography using digital micro-mirror dynamic mask," *Sensors and Actuators A: Physical*, vol. 121, no. 1, pp. 113–120, 2005.

[17] E. Özkol, W. Zhang, J. Ebert, and R. Telle, "Potentials of the 'direct inkjet printing' method for manufacturing 3Y-TZP based dental restorations," *Journal of the European Ceramic Society*, 2012.

[18] J. R. Evans, M. J. Edirisinghe, and J. Song, "Direct ink-jet printing of vertical walls," *Journal of the American Ceramic Society*, vol. 85, no. 8, pp. 2113–2115, 2002.

[19] N. R. Philips, B. G. Compton, and M. R. Begley, "High strength alumina micro-beams fabricated by inkjet printing," *Journal of the American Ceramic Society*, vol. 95, no. 10, pp. 3016–3018, 2012.

[20] www.stratasys.com, "Polyjet technology," 2013.

[21] S. Kumar, "Selective laser sintering: a qualitative and objective approach," *JOM*, vol. 55, no. 10, pp. 43–47, 2003.

[22] S. Uhland, R. Holman, M. Cima, E. Sachs, and Y. Enokido, "New process and materials developments in 3-dimensional printing, 3DP™," in *MRS Proceedings*, vol. 542, Cambridge Univ Press, 1998.

[23] P. Calvert, "Inkjet printing for materials and devices," *Chemistry of Materials*, vol. 13, no. 10, pp. 3299–3305, 2001.

[24] M. A. Mignardi, J. B. Sampsell, and R. M. Boysel, "Digital micromirror shutter device," 1993.

[25] www.fujifilmusa.com, "Diamatix industrial inkjet printheads," 2013.

[26] H. Fukuchi and T. Ushioda, "Multi-nozzle ink-jet print head of drop-on-demand type," 1985.

[27] J. R. Anderson, D. T. Chiu, H. Wu, O. J. Schueller, and G. M. Whitesides, "Fabrication of microfluidic systems in poly(dimethylsiloxane)," *Electrophoresis*, vol. 21, pp. 27–40, 2000.

[28] J. C. McDonald and G. M. Whitesides, "Poly(dimethylsiloxane) as a material for fabricating microfluidic devices," *Accounts of Chemical Research*, vol. 35, no. 7, pp. 491–499, 2002.

[29] M. A. Eddings, M. A. Johnson, and B. K. Gale, "Determining the optimal PDMS–PDMS bonding technique for microfluidic devices," *Journal of Micromechanics and Microengineering*, vol. 18, no. 6, p. 067001, 2008.

[30] D. A. Mair, M. Rolandi, M. Snauko, R. Noroski, F. Svec, and J. M. Fréchet, "Room-temperature bonding for plastic high-pressure microfluidic chips," *Analytical chemistry*, vol. 79, no. 13, pp. 5097–5102, 2007.

[31] Y. Sun, Y. C. Kwok, and N.-T. Nguyen, "Low-pressure, high-temperature thermal bonding of polymeric microfluidic devices and their applications for electrophoretic separation," *Journal of Micromechanics and Microengineering*, vol. 16, no. 8, p. 1681, 2006.

[32] G. M. Whitesides, "The origins and the future of microfluidics," *Nature*, vol. 442, no. 7101, pp. 368–373, 2006.

[33] H. Klank, J. P. Kutter, and O. Geschke, "CO_2-laser micromachining and back-end processing for rapid production of pmma-based microfluidic systems," *Lab on a Chip*, vol. 2, no. 4, pp. 242–246, 2002.

[34] G.-B. Lee, S.-H. Chen, G.-R. Huang, W.-C. Sung, and Y.-H. Lin, "Microfabricated plastic chips by hot embossing methods and their applications for DNA separation and detection," *Sensors and Actuators B: Chemical*, vol. 75, no. 1, pp. 142–148, 2001.

[35] L. Brown, T. Koerner, J. H. Horton, and R. D. Oleschuk, "Fabrication and characterization of poly(methylmethacrylate) microfluidic devices bonded using surface modifications and solvents," *Lab on a Chip*, vol. 6, no. 1, pp. 66–73, 2006.

[36] F. M. White, *Fluid mechanics*. McGraw-Hill, Singapore, 1979.

[37] A. Akers, M. Gassman, and R. Smith, *Hydraulic power system analysis*. CRC press, 2010.

[38] D. C. Rennels and H. M. Hudson, *Pipe flow: A practical and comprehensive guide*. Wiley, 2012.

[39] C. D. Murray, "The physiological principle of minimum work: Oxygen exchange in capillaries," *Proceedings of the National Academy of Sciences of the United States of America*, vol. 12, no. 5, p. 299, 1926.

[40] D. R. Emerson, K. Cieślicki, X. Gu, and R. W. Barber, "Biomimetic design of microfluidic manifolds based on a generalised Murray's law," *Lab on a Chip*, vol. 6, no. 3, pp. 447–454, 2006.

[41] W. Wu, C. J. Hansen, A. M. Aragón, P. H. Geubelle, S. R. White, and J. A. Lewis, "Direct-write assembly of biomimetic microvascular networks for efficient fluid transport," *Soft Matter*, vol. 6, no. 4, pp. 739–742, 2010.

[42] W. Wu, A. DeConinck, and J. A. Lewis, "Omnidirectional printing of 3D microvascular networks," *Advanced Materials*, vol. 23, no. 24, pp. H178–H183, 2011.

[43] T. F. Sherman, "On connecting large vessels to small. the meaning of Murray's law," *The Journal of General Physiology*, vol. 78, no. 4, pp. 431–453, 1981.

[44] J. Hron, J. Málek, and S. Turek, "A numerical investigation of flows of shear-thinning fluids with applications to blood rheology," *International Journal for Numerical Methods in Fluids*, vol. 32, no. 7, pp. 863–879, 2000.

[45] F. Cogswell, "Converging flow of polymer melts in extrusion dies," *Polymer Engineering and Science*, vol. 12, no. 1, pp. 64–73, 1972.

[46] J. L. White and B. Lee, "An experimental study of sandwich injection molding of two polymer melts using simultaneous injection," *Polymer Engineering and Science*, vol. 15, no. 7, pp. 481–485, 1975.

[47] W. R. Schowalter, *Mechanics of non-Newtonian fluids*. Pergamon press Oxford, 1978.

[48] J. E. Smay, J. Cesarano, and J. A. Lewis, "Colloidal inks for directed assembly of 3D periodic structures," *Langmuir*, vol. 18, no. 14, pp. 5429–5437, 2002.

[49] T.-J. Liu, "Fully developed flow of power-law fluids in ducts," *Ind. Eng. Chem. Fundam.*, vol. 22, pp. 183–186, 1983.

[50] P. Kennedy, *Flow analysis of injection molds*. Hanser New York, 1995.

[51] E. M. Purcell, "Life at low reynolds number," *Am. J. Phys*, vol. 45, no. 1, pp. 3–11, 1977.

[52] G. Mohiuddin Mala and D. Li, "Flow characteristics of water in microtubes," *International Journal of Heat and Fluid Flow*, vol. 20, no. 2, pp. 142–148, 1999.

[53] I. Idelchik, *Handbook of Hydraulic Resistance*. Jaico Publishing House, 3rd ed., 2003.

[54] A. S. Iberall and S. Z. Cardon, "Aeration mass-transfer related to Reynolds number," *Journal of Applied Chemistry*, vol. 16, pp. 64–72, 1966.

[55] J. Bruneaux, D. Therriault, and M.-C. Heuzey, "Micro-extrusio of organic inks for direct-write assembly," *J. Micromech. Microeng.*, vol. 18, 2008.

[56] M. L. Sheely, "Glycerol viscosity tables," *Industrial and Engineering Chemistry*, vol. 24, no. 9, pp. 1060–1064, 1932.

[57] R. Tanner, "A theory of die-swell," *Journal of Polymer Science Part A-2: Polymer Physics*, vol. 8, no. 12, pp. 2067–2078, 1970.

[58] D. Therriault, S. R. White, and J. A. Lewis, "Rheological behavior of fugitive organic inks for direct-write assembly," *Applied Rheology*, vol. 17, no. 1, pp. 10112.1–10112.8, 2007.

[59] C. J. Hansen, *Self-healing materials and multinozzle printheads with embedded microvascular networks*. PhD thesis, University of Illinois, Urbana-Champaign, 2011.

[60] D. Therriault, R. F. Shepherd, S. R. White, and J. A. Lewis, "Fugitive inks for direct-write assembly of three-dimensional microvascular networks," *Advanced Materials*, vol. 17, no. 4, pp. 395–399, 2005.

[61] D. Therriault, S. R. White, and J. A. Lewis, "Chaotic mixing in three-dimensional microvascular networks fabricated by direct-write assembly," *Nature Materials*, vol. 2, no. 4, pp. 265–271, 2003.

[62] www.norlandprod.com, "Norland optical adhesive 61," 2013.

[63] D. B. Kolesky and J. A. Lewis, "Unpublished work," 2013.

[64] B. Y. Ahn, E. B. Duoss, M. J. Motala, X. Guo, S.-I. Park, Y. Xiong, J. Yoon, R. G. Nuzzo, J. A. Rogers, and J. A. Lewis, "Omnidirectional printing of flexible, stretchable, and spanning silver microelectrodes," *Science*, vol. 323, no. 5921, pp. 1590–1593, 2009.

[65] J. Dyson, "The equiangular spiral antenna," *Antennas and Propagation, IRE Transactions on*, vol. 7, no. 2, pp. 181–187, 1959.

[66] J. M. Bell and M. F. Iskander, "A low-profile archimedean spiral antenna using an EBG ground plane," *Antennas and Wireless Propagation Letters, IEEE*, vol. 3, no. 1, pp. 223–226, 2004.

[67] T. Kajiyama, K. Tanaka, and A. Takahara, "Depth dependence of the surface glass transition temperature of a poly(styrene-block-methyl methacrylate) diblock copolymer film on the basis of temperature-dependent X-ray photoelectron spectroscopy," *Macromolecules*, vol. 28, no. 9, pp. 3482–3484, 1995.

[68] J.-Z. Liang, "Melt extrusion properties of ABS and ABS-quasinano-$CaCO_3$ composite," *Journal of elastomers and plastics*, vol. 36, no. 4, pp. 363–374, 2004.

[69] C.-M. Ho and Y.-C. Tai, "Micro-electro-mechanical-systems (MEMS) and fluid flows," *Annual Review of Fluid Mechanics*, vol. 30, no. 1, pp. 579–612, 1998.

[70] M. Rowe, "Measurements and computations of flow in pipe bends," *J. Fluid Mech*, vol. 43, no. pt 4, pp. 771–783, 1970.

[71] J. Du Plessis and M. Collins, "A new definition for laminar flow entrance lengths of straight ducts," *N&O Joernaal*, pp. 11–16, 1992.